DISSERTATION

NEUTRINO BEAM BUNCH STRUCTURE RECONSTRUCTION WITH PRECISION TIMING IN THE ICARUS LIQUID ARGON TIME PROJECTION CHAMBER

Submitted by

Anna Heggestuen

Department of Physics

In partial fulfillment of the requirements

For the Degree of Doctor of Philosophy

Colorado State University

Fort Collins, Colorado

Summer 2026

Doctoral Committee:

Advisor: Robert J. Wilson

Michael Mooney
Joshua Berger
Alexander Brandl

ABSTRACT

NEUTRINO BEAM BUNCH STRUCTURE RECONSTRUCTION WITH PRECISION TIMING IN THE ICARUS LIQUID ARGON TIME PROJECTION CHAMBER

The ICARUS detector has been operating smoothly since 2021 as the far detector in the Short Baseline Neutrino (SBN) program at Fermilab, collecting neutrino interactions from both the Booster Neutrino Beam (BNB) and off-axis from the Neutrinos at the Main Injector (NuMI) beam. Analysis of neutrino interactions in ICARUS requires mitigation of substantial cosmogenic backgrounds. This is achieved by using an external Cosmic Ray Tagger (CRT) and a Photomultiplier Tube (PMT) system embedded in the liquid argon. The intrinsic neutrino beam bunch structure, inherited time structure from the Radio Frequency (RF) system used to accelerate the protons, can be resolved at the ICARUS detector using precise timing information.

Located at shallow depth, ICARUS is exposed to a high flux of cosmic rays that can be mistaken for neutrino interactions. To mitigate this background, the CRT and a 3-meter-thick concrete overburden were installed. To better model backgrounds, ICARUS makes use of an overlay technique where simulated neutrino events are superimposed on detector beam-off data. PMTs installed within a Time Projection Chamber detect argon scintillation light emitted by high energy charged particles passing through the chamber and provide the event timing of neutrino interactions. The nanosecond-level beam bunch structure is reconstructed with the PMT system and can be used to further understand backgrounds and enhance neutrino physics capabilities. In this thesis, I will discuss background mitigation techniques using precision timing and present a novel technique to select neutrino events from our unbiased data stream using the beam bunch structure.

ACKNOWLEDGEMENTS

I would like to gratefully express my appreciation for my family, friends, CSU and ICARUS colleagues, and my committee. I feel incredibly fortunate to have reached this point with the continued support from people that are very special to me. Throughout my academic career, I have been lucky to find incredible guidance from mentors that believed in me from the start.

First, I would like to express my deepest gratitude for my advisor Professor Robert J. Wilson. Before I even started the PhD program at CSU, he trusted me to travel out to Fermilab to assist with quality control tests of the ICARUS Cosmic Ray Tagger system. He provided guidance as both my academic and research advisor during my Masters Program while I took courses, allowing me to work fully as a research assistant during my second year of graduate school which was a great opportunity to gain knowledge early in the program. He continually offered lots of time and advice during these challenging years. He provided me with countless opportunities to demonstrate my knowledge in the field while living and working at Fermilab, and further trusted me to serve as Run Coordinator for the full ICARUS experiment. I would not be here without his continuous encouragement and support, and I can't thank him enough for believing in me from the start. I would also like to thank the members of my PhD committee, Michael Mooney, Joshua Berger, and Alexander Brandl, for their time and guidance on my research.

My family has been an incredible source of support during my PhD, and recognize I would not have reached this point without them. I give my mom, Linda, endless credit for helping me discover the exciting world of High Energy Particle Physics, as she helped me find jobs in physics at UMD which launched my interest and passion for physics. Throughout my whole academic career, she has encouraged me and made me feel capable that I can tackle any challenge and has provided daily support while I complete this degree. I appreciate her coming out to visit many times and being such a supportive mom, and I feel so fortunate to be her daughter. My sister, Ali, has been a continuous source of support, calming me down during countless, panicked phone calls. She believed and encouraged me from the very beginning and throughout this whole degree. My dad, Jim, has always been passionate about science and helped spark my curiosity in the beautiful world around us, always sharing some cool fact he just learned. He let me vent about any difficulties I was facing, offering advice and always reminded me how proud he is. I am immensely thankful for my family, and so thankful to have reached this point with their endless support. I feel incredibly proud to be Dr. Heggestuen!

I have learned so much from my CSU and Fermilab colleagues, which have become what feels close to family.

Biswaranjan Behera, a postdoctoral researcher from CSU and now a professor at Indian Statistical Institute Kolkata, worked close with me from the very beginning and has taught me so much. I thank him for the continuous guidance, patiently answering my questions at any hour and providing endless support throughout my degree, even after moving on from the CSU group. I also feel like I would not have reached this point without him believing in me from the start, and thank him for being such a good friend to me.

Tyler Boone was a fellow CSU graduate student in Wilson's group, and is always so kind and supportive. I feel so lucky to have worked with him on the CRT system and have desks right next to each other on the 12th floor at Wilson Hall. I thank him for the fun times over the years and always being willing to listen and help me solve problems. I have learned so much from him.

Jamie Dyer is a fellow CSU graduate student in my cohort, and I feel so grateful to have gone through this PhD journey with her. We spent countless hours on zoom together while completing coursework, were lucky enough to live together out at Fermilab and had amazing adventures traveling for ICARUS Collaboration Meetings and conferences. I feel so lucky and thankful to have her by my side during these years.

Gray Putnam is a Fermilab postdoctoral researcher working on SBN, who did their PhD on the ICARUS Experiment and we overlapped for many years at Fermilab. Throughout the years, Gray has been a great friend and support system.

Chrisa Hilgenberg was a graduate student at CSU and provided support and guidance during my first years. They had a large involvement in designing and constructing the Side CRT system

using repurposed moduels from the MINOS experiment, and was kind and patient working with me from the beginning.

Ivan Caro Terrazas was a postdoctoral researcher at CSU in Wilson's group. He has been a great source of support over the years and helped push my ICARUS production requests through, and providing help whenever I needed it. Ivan has also been a great friend to me over the years and I feel so lucky to have had him in the group.

Dante Tonani is a research associate at CSU also working in Wilson's group. After first meeting back in 2017/2018, we've been good friends throughout the years. He is always willing to provide guidance at work and more than happy to grab a beer at the pub or in Batavia. I'm thankful for his support and reminding me to not complicate things too much in research.

Jacob Boza is a fellow CSU graduate student working in Wilson's group, focused on the DUNE project. He started just a couple years after me and has been a great friend, always willing to have a pint at the pub and has always been interested and excited about the work I'm doing. I'm thankful to have him in the group and as a good friend.

Noah Vary is a fellow CSU graduate student also working in Wilson's research group. It has been a pleasure working with him over the past few years and I'm thankful for the patience he gave me during my thesis writing. I'm excited to see where he will take this research next.

I'm thankful for my ICARUS colleagues who made working for this collaboration so enjoyable, with a special shout out to Nadia Abrego, Maria Artero, Minerba Betancourt, Milind Diwan, Christian Farnese, Angela Fava, Daniele Gibin, Alberto Guglielmi, Bruce Howard, Wooyoung Jang, Jaesung Kim, Guadalupe Moreno, Justin Mueller, Gianluca Petrillo, Gray Putnam, Francesco Poppi, Logan Clutch Jackson Rice, Promita Roy, Clara Saia, Mattia Sotgia, Dante Totani, Riccardo Triozzi, Filippo Varanini, Matteo Vicenzi and Jacob Zettlemoyer. I thank the whole collaboration for guiding me and helping me establish myself as a researcher.

I've met so many amazing friends living out at Fermilab and hanging out at the Users Center, with too many to list. I thank everyone for so many fun memories and acting as a second family. A special shout out to Tania Claudette, who has been such a good friend to me from the very

beginning when I visited Fermilab. She was always there to listen to me vent and provide encouragement and support, and I feel so thankful for our conversations at the Fermilab Users Center and adventures around the lab.

I'm incredibly thankful for the encouragement and support from my friends and appreciate their patience with me through the years with my busy schedule. Thank you Kenz, Maggie, Siri, Patrish, Joe and Max for all of the love and fun times.

I would like to thank the Fermilab woods and prairie for providing a place of solitude during long days and nights, and giving space for me to think through problems. I also give a big thanks to music for helping me feel good and the ability to change my mindset and focus. Finally, I would like to thank all the birds. I discovered my love for birds after meeting an owl family in Fort Collins in a large cottonwood just down the road from my apartment, and visiting the owls and listening to birds has helped me step back and be present during both good and challenging days.

DEDICATION

I would like to dedicate this thesis to my mom, dad, sister, and our sweet, fluffy Coco dog.

TABLE OF CONTENTS

LIST OF TABLES

LIST OF FIGURES

Chapter 1

Introduction

The Standard Model of Elementary Particles describes our understanding of the particles that make up the observable universe. The fundamental particles and related force carriers that make up the Standard Model are shown in Figure 1.1. Within the Standard Model, neutrinos are the most abundant, yet weakly interacting, massive particles. Neutrinos have a very small mass compared to the other Standard Model particles; so small it was long thought that neutrinos are massless. Due to their elusive nature, neutrinos are extremely challenging to study since they rarely interact with ordinary matter. The communities understanding of neutrinos has greatly evolved since their first detection over 60 years ago, but there remain many open questions about the true nature of neutrinos. Within the Short Baseline (SBN) program, the ICARUS experiment detects man-made neutrinos from the Fermilab Accelerator complex. As challenging neutrinos are to study, exploiting precise timing signals of the neutrino beam allows us to know exactly when to expect the neutrinos at the detector. Further, the time sub-structure within the beam can be resolved with the ICARUS detector. This thesis presents the first selection of unbiased neutrino events leveraging precision timing of the intrinsic sub-structure of the neutrino beam.

1.1 Neutrino Physics

1.1.1 History of Neutrinos

The concept of a neutrino was originally proposed in 1930 by Wolfgang Pauli as a "desperate remedy" [24] to explain missing energy and momentum in beta decay. Pauli proposed a light, spin-1/2, neutral particle. Enrico Fermi coined the name for the neutrino which translates to "little neutral one" in Italian [24]. It wasn't until 1953 when the first hints of neutrinos were detected from a nuclear reactor in The Hanford Experiment [25], where Reines and Cowan noticed a small increase in the number of events when the reactor was on versus when it was off, though this was not

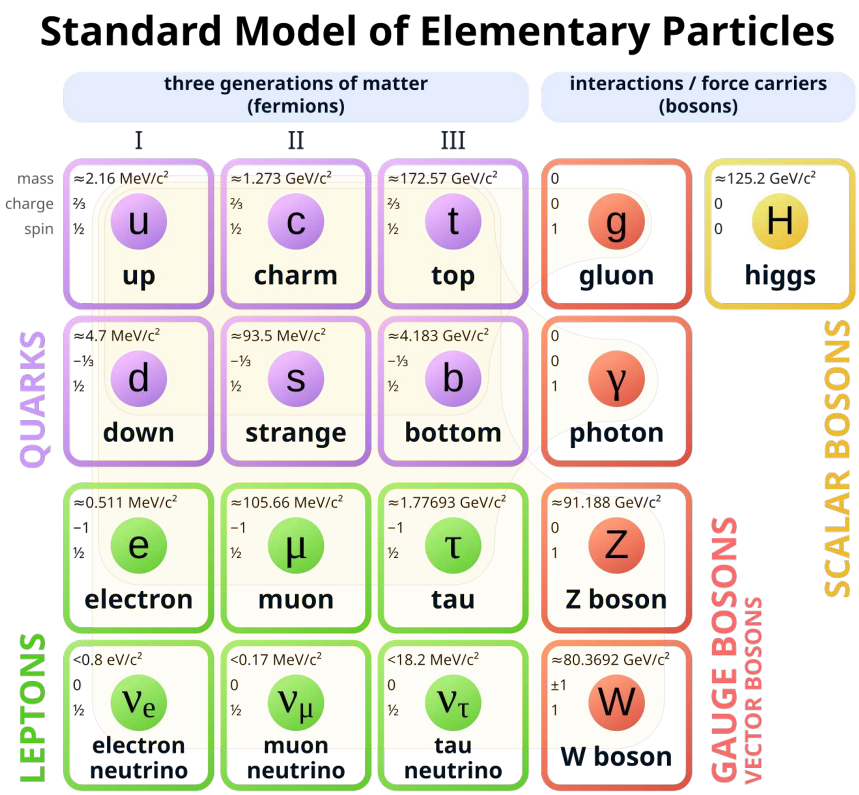

Figure 1.1: Elementary particles and forces that make up the Standard Model of particle physics. Figure from [1].

yet sufficient to claim that neutrino events were being detected. The experiment was completely redesigned and moved to the Savannah River reactor and on June 14, 1956 Reines and Cowan informed Wolfgang Pauli in a telegram [26] that they had definitively detected anti-electron neutrinos emitted from fission fragments [27]. This result was recognized with the 1995 Nobel Prize almost 40 years later [28]. In 1963, Lederman, Schwartz, and Steinberger at Brookhaven National Laboratory proved the existence of the muon neutrino [29], providing the first hints of the second family of elementary particles, earning them the 1988 Nobel Prize in Physics. The Homestake Experiment started in the late 1960's by radio-chemist Raymond Davis, Jr. and astrophysicist John N. Bahcall collecting and counting neutrinos being emitted from nuclear fusion processes in the Sun. They observed a large discrepancy between the number of neutrino events detected compared to the number of solar neutrinos predicted from the Sun's luminosity, sparking what is known as the "Solar Neutrino Problem" [30].

This discrepancy between detected and predicted solar neutrinos could be explained by a process discussed by Bruno Pontecorvo in 1957 [31], [32] called neutrino oscillation, a quantum mechanical phenomenon where the neutrinos exist in a superposition of defined-mass eigenstates, allowing the neutrino to be created as one type and detected as another. Pontecorvo's idea of neutrino oscillation eventually resolved the Solar Neutrino Problem. Up until the 1970's, it was believed neutrinos were massless particles. Pontecorvo recognized that if neutrinos have mass, they would be able to oscillate from one flavor to another. This observed phenomena would require modifications to physicists current Standard Model, as neutrinos are taken to be massless in the Standard Model.

Strong evidence for neutrino oscillation was observed in the Super-Kamiokande experiment [33] in Japan studying atmospheric muon neutrinos. Super-K compared the rate of neutrinos coming from above the detector with those coming through the Earth, suggesting that muon neutrinos were oscillating into tau neutrinos within the Earth. The Sudbury Neutrino Observatory (SNO) in Ontario, Canada [34] began collecting data soon after, observing solar neutrino interactions in a large tank of heavy water. SNO demonstrated that solar electron neutrinos were oscillating into

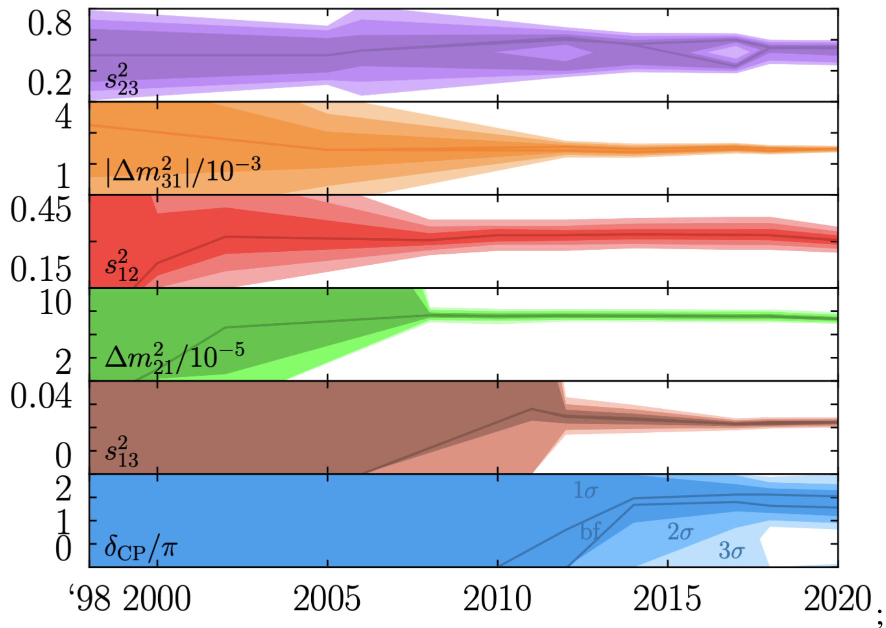

Figure 1.2: Neutrino oscillation parameters vs. calender year, showing the evolution of the communities understanding of them. Parameters are listed in the order they were first measured. Figure from [2].

different neutrinos as they traveled to the Earth. These two experiments resolved the Solar Neutrino Problem by providing direct evidence for neutrino oscillation and leading to Super-K and SNO collaborators the 2015 Nobel Prize in Physics.

Neutrino oscillation depends on the ratio of the distance traveled (L) and the neutrino energy (E). Different neutrino sources (accelerator, solar, atmospheric or reactor) produce different energy ranges of neutrinos and neutrino detectors sample neutrinos at fixed distances (L), making the different neutrino sources and technologies sensitive to different oscillation parameters. See Figure 1.2 for a look at the different oscillation parameters and the communities current understanding of them. In general, detectors located near the source (< 1 kilometers) are referred to as Short-Baseline experiments while Long-Baseline experiments typically have multiple (near and far) detectors located hundreds to thousands of kilometers apart.

1.1.2 Short-Baseline Anomalies

Several experimental anomalies of excess ν_e candidates in a ν_μ beam have been observed over the years. In the 1990's, the Liquid Scintillator Neutrino Detector (LSND) [35] performed a search

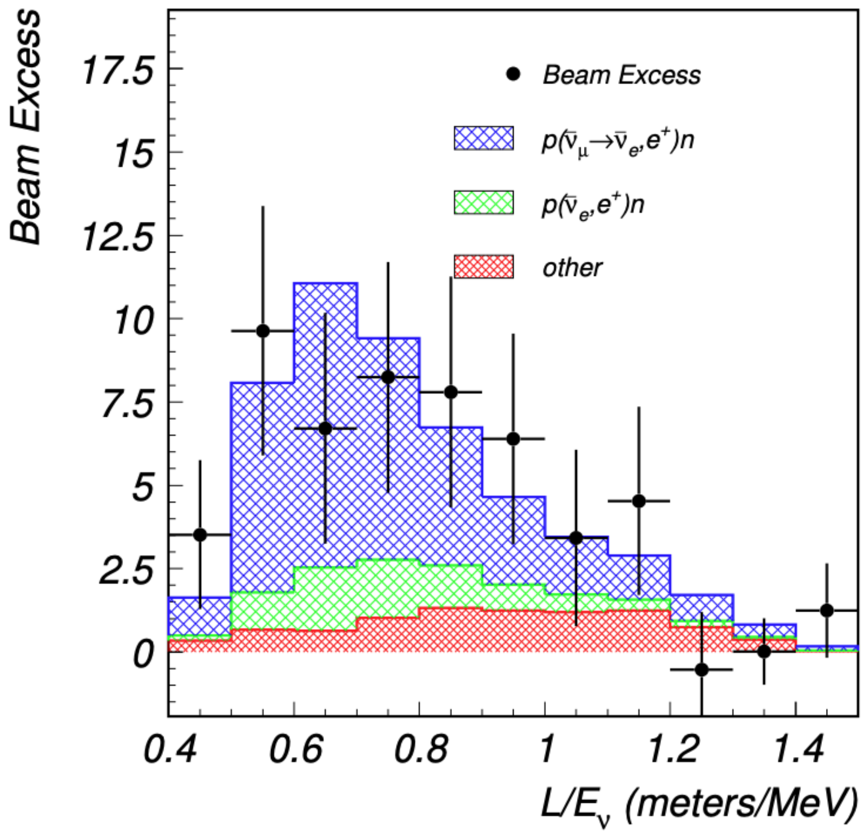

Figure 1.3: LSND excess of $\overline{\nu}_e$ events from $\overline{\nu}_\mu$ from μ^+ decay at rest at Los Alamos Neutron Science Center. Figure from [3].

for $\overline{\nu}_\mu$ to $\overline{\nu}_e$ oscillations at Los Alamos Neutron Science Center using $\overline{\nu}_\mu$ from μ^+ decay at rest. An excess of $\overline{\nu}_e$ was observed at 3.8 σ, see Figure 1.3. The Mini Booster Neutrino Experiment (MiniBooNE) [36] originated in attempt to confirm or refute the results from LSND. The Booster Neutrino Beam (BNB) was turned on in 2002 and MiniBooNE collected samples of both neutrinos and antineutrinos in tank of mineral oil located at Fermilab. MiniBooNE observed an excess of ν_e and $\overline{\nu}_e$ from a ν_μ and $\overline{\nu}_\mu$ beam at the 4.8 σ level (See Figure 1.4) and at the 6.1 σ level when combined with LSND [37].

Oscillations at this short of a baseline are not predicted within the Standard Model, hinting at new physics. Several theories suggest this excess could be explained by hypothetical sterile neutrino(s) at $\Delta m^2 \sim 1\mathrm{eV}^2$, where a sterile neutrino would not interact through the weak force.

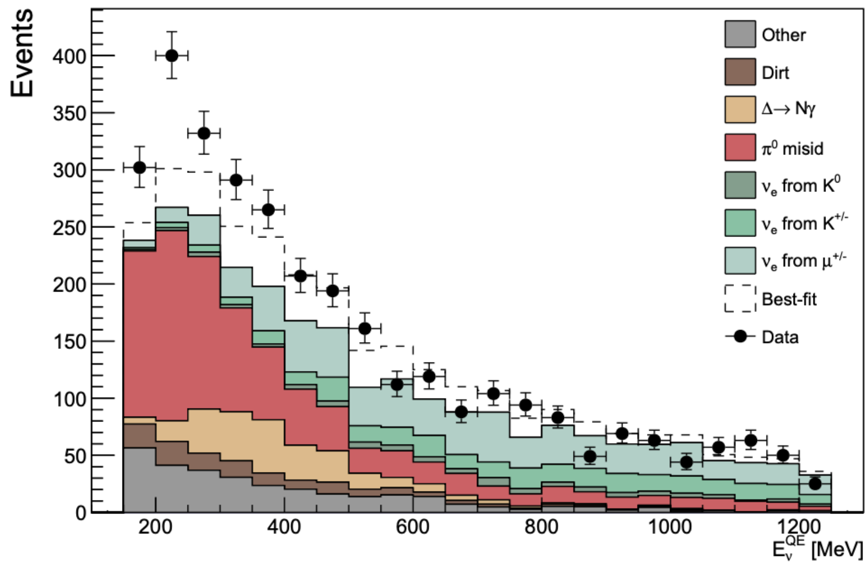

Figure 1.4: MiniBooNE excess of ν_e and $\overline{\nu}_e$ from a ν_μ and $\overline{\nu}_\mu$ beam. Figure from [4].

Through this mechanism, the muon neutrinos could oscillate into a sterile neutrino before oscillating back to electron neutrinos, offering an explanation for the excess electron neutrino events.

1.2 Short-Baseline Neutrino Program

The Particle Physics Project Prioritization Panel P5 report [38] from 2014 recommended a short-baseline neutrino program based at Fermilab. The Short Baseline Neutrino (SBN) Program was proposed in 2015 to perform a direct search for an eV-scale sterile neutrino. The original SBN proposal [5] estimates that a search for muon neutrino to electron neutrino appearance can be performed with $\sim$5 sigma sensitivity for the LSND allowed (99% C.L.) parameter region, with the estimated sensitivities shown in Figure 1.6 with a simple 3+1 sterile neutrino model.

The SBN program is composed of three detectors situated along the Booster Neutrino Beam (BNB) at Fermilab (See Figure 1.7). The SBN Detectors utilize Liquid Argon Time Projection Chamber (LArTPC) technology which enables precise imaging of particle interactions. The general principles of LArTPC are described in Section 1.2.1, followed by an overview of the Booster Neutrino Beam in Section 1.2.2. The three SBN detectors, MicroBooNE, SBND and ICARUS, will be described in Sections 1.2.3, 1.2.4 and Chapter 2, respectively. Only the near and far de-

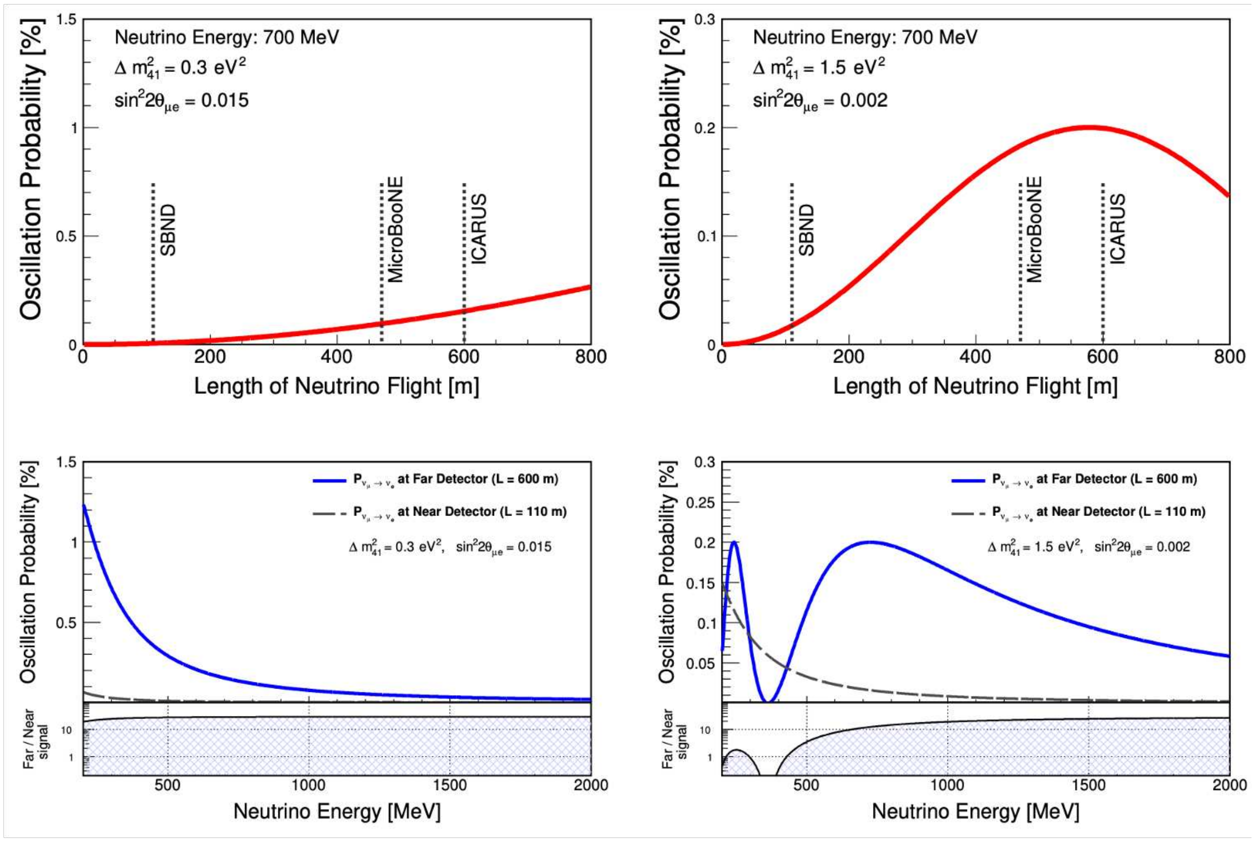

Figure 1.5: ν_μ to ν_e oscillation probabilities as a function of the baseline (L) and ν energy (E) for two 3+1 sterile neutrino benchmarks. Figure from [5].

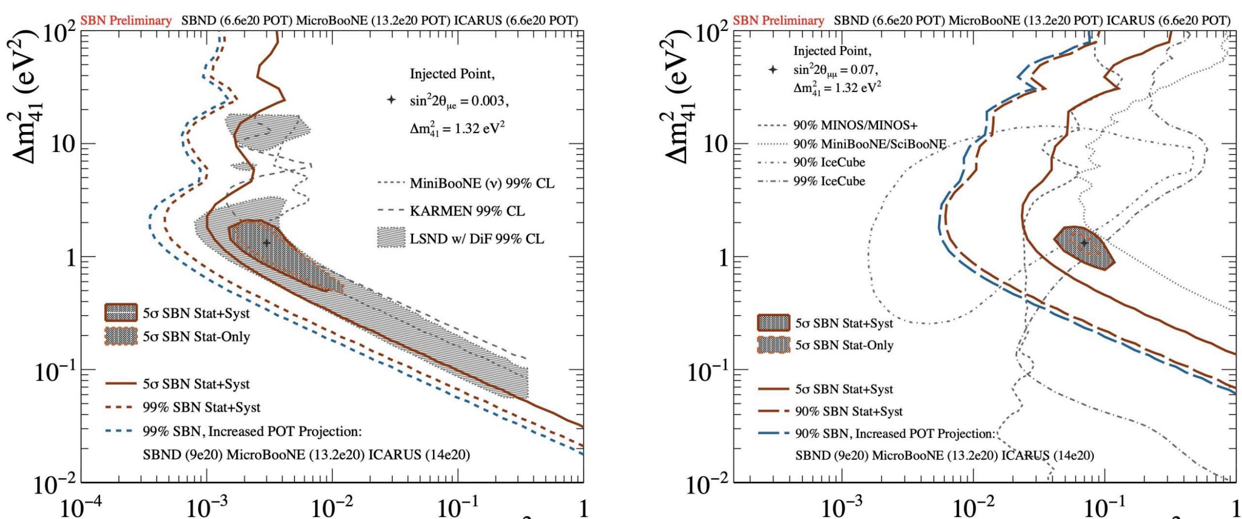

Figure 1.6: Estimated SBN 5σ sensitivities using a simple 3+1 sterile neutrino model, with ν_e appearance on the left and ν disappearance on the right.

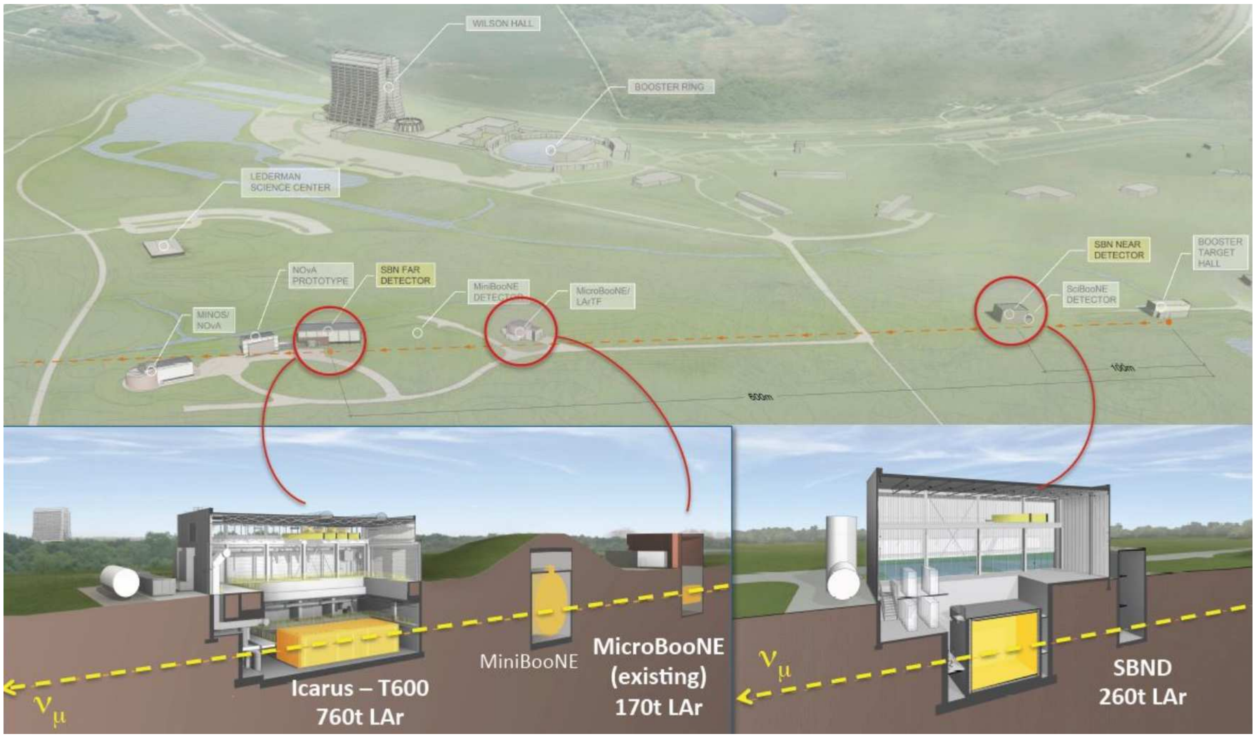

Figure 1.7: Overview of the Short Baseline Neutrino program at Fermilab, with three Liquid Argon Time Projection Chambers situated along the Booster Neutrino beam. The Short Baseline Near Detector (SBND) is the closest to the neutrino beam target and ICARUS operates as the far detector. MicroBooNE operated independently and collected beam data prior to the joint operation of ICARUS and SBND.

tectors, SBND and ICARUS, operated in the beam together. MicroBooNE was proposed and built to look directly for the anomaly observed by MiniBooNE, instead using the LArTPC technology. As opposed to the Cherenkov detector technology used by MiniBooNE, LArTPCs have the ability to distinguish electrons from photons, allowing to search directly for the low energy excess from electron neutrinos at short baselines. MicroBooNE, which will be discussed in more detail in Section 1.2.3 performed direct searches for the low energy excess observed by LSND and MiniBooNE and reported no excess of electron neutrino candidates. With SBND and ICARUS, the SBN program aims to either confirm or exclude sterile neutrinos as the source of the short-baseline anomalies, targeting a sensitivity of 5 sigma.

1.2.1 Liquid Argon Time Projection Chamber Technology

A LArTPC consists of a large tank of cryogenically cooled liquid argon under the influence of a uniform electric field readout by an array of wires and photomultiplier tubes (PMT)s. When a charged particle interacts in the liquid argon, this produces ionization electrons and scintillation light. A uniform electric field is applied between the cathode and anode (wire) plane. Ionization electrons drift towards an anode readout wire plane in the electric field where the charge is sampled over three wire planes. The ionization charge induces signals in non-destructive way on the first two planes (Induction-1 and Induction-2), then it is finally collected by the last plane (Collection plane), providing three 2D views of the same particle interaction. A schematic of the general operating principle of a LArTPC is shown in Figure 1.8.

Using liquid argon as the detector medium has many benefits. It has a relatively high density (1.4 g/mL) which is beneficial for a neutrino detector, as the neutrino cross section scales with the density of the detector material. More importantly, LAr acts as both the detector target and the scintillating material with $\sim$50,000 photons/MeV for a minimum ionizing particle. Since argon is a noble gas with few free electrons, the energy from charged particles crossing the detector either ionize the argon or produce scintillation photons, resulting in a long drift lifetime. In addition, LAr can be highly purified, removing organic impurities to very low levels and allowing ionization trails drifting under the influence of an electric field over 100's of centimeters. Liquid argon is also relatively cheap and easy to obtain, as its the third most abundant gas in Earth's atmosphere ($\sim$1%), which is an important consideration for building large scale detectors.

Scintillation photons from the interaction are detected on an array of PMTs mounted behind the three wire planes of the TPC. The PMTs are used to reconstruct the position of the event along the charge drift direction and for the trigger of the full detector. PMTs are capable of detecting fast scintillation light with a response time of $\sim$nanoseconds, while the time it takes electrons to drift to the TPC wire planes is much longer, $\sim$milliseconds. LArTPC technology on a large scale was conceived by Carlo Rubbia in 1977 [39], building on Nygren's concept of a gaseous TPC, and

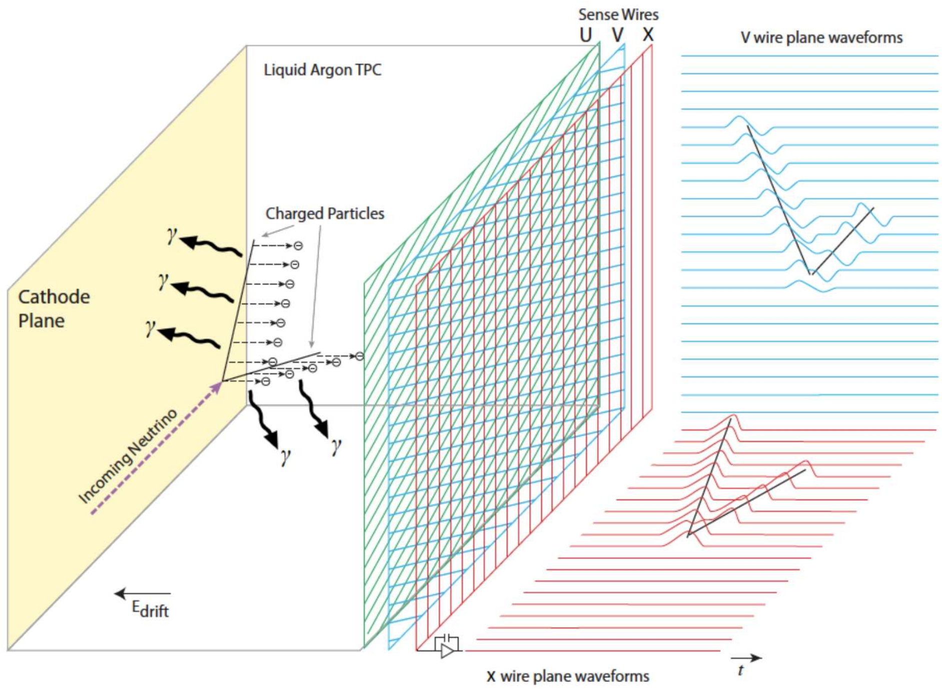

Figure 1.8: A cartoon showing the general operating principles of a Liquid Argon Time Projection Chamber from [6].

the technology was developed by ICARUS Collaboration for over 25 years [11], [40] (for more details, see Chapter 2).

1.2.2 Neutrino Beams

The SBN Program detectors are located along the Booster Neutrino Beam (BNB) at Fermilab. ICARUS collects neutrinos from both the BNB and Neutrinos at the Main Injector (NuMI) beams. Using superconducting radio-frequency (RF) cavities, 400 MeV protons from the Linac [20] are accelerated up to 8 GeV (120 GeV) kinetic energy before being extracted to the BNB (NuMI) target to produce a beam of hadrons [7]. The Booster, Main Injector and other components of the Fermilab Accelerator complex are depicted in Figure 1.9. A magnetic focusing horn with a 174 kA current in 143 μs pulses [5] coincident with the proton extraction running through the exterior of the focusing horn focuses and sign selects the hadrons. Based on the sign of the current through the focusing horn, either positive or negative particles are selected. The hadrons, mostly pions and kaons, are directed into a decay pipe where they decay into neutrinos and other mesons (eg.

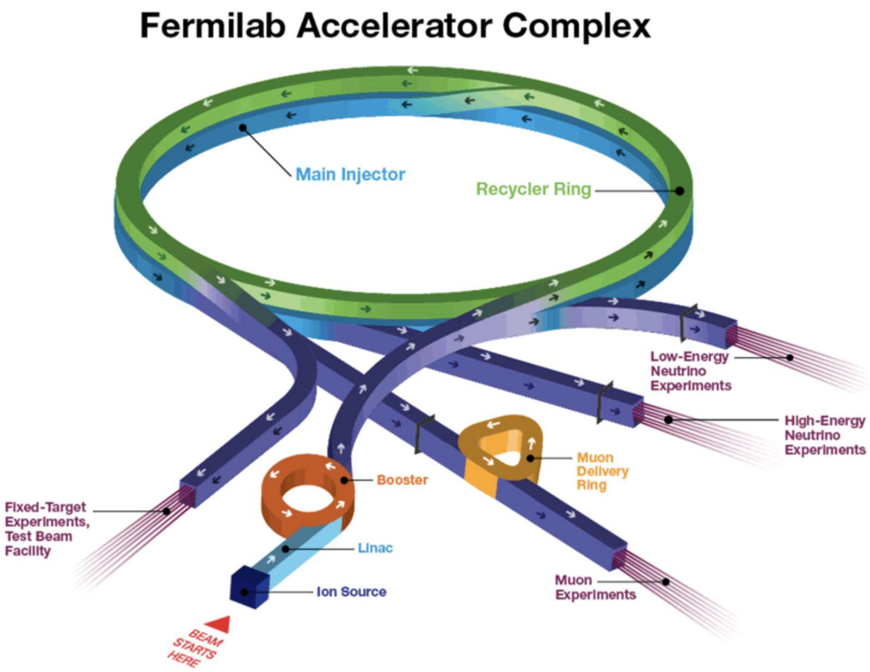

Figure 1.9: Diagram of the Fermilab Accelerator complex showing the Booster and Main Injector rings from [7].

muons). The mesons decay in the pipe or are stopped in an absorber, while the neutrinos travel downstream to the detectors intervening dirt and rock. Using RF cavities to accelerate the protons results in the the beam "bunching" in time. For BNB, 8 GeV protons with a RF frequency of 52.8 MHz [20] are extracted from the Booster accelerator before hitting a beryllium target. A 1.6 μs BNB spill is composed of 81 bunches spaced ∼18.9 ns apart. For NuMI, the 8-GeV protons from the Booster are extracted into the Main Injector ring and are accelerated up to 120 GeV (53.1 MHz [41]) before hitting a graphite target. A NuMI neutrino spill is 9.5 μs long with 486 bunches spaced by ∼18.8 ns [42]. The NuMI beam set a beam power record of 1.018 MW in summer 2024. These features are summarized in Table 1.1 and more details about the neutrino beams will be provided in Chapter 6.

1.2.3 MicroBooNE

MicroBooNE [8] was the first operational LArTPC located along BNB and started collecting neutrino data in October 2015. This experiment was originally built to look for the anomaly seen

	Spill	Bunches per spill	Bunch Spacing	Proton Energy	POT per spill
BNB	1.6 μs	81	18.9 ns	8 GeV	$5 \cdot 10^{12}$
NuMI	9.5 μs	486	18.8 ns	120 GeV	$6 \cdot 10^{13}$

Table 1.1: Beam parameters of the Booster Neutrino Beam (BNB) and Neutrinos at the Main Injector (NuMI) neutrino beams at Fermilab showing the spill duration, the number of bunches per spill, intrinsic beam bunch spacing, incident proton energy, and amount of Protons-on-Target (POT) per spill.

by LSND and MiniBooNE, using LArTPC technology with the ability to distinguish electrons from photons. This allows for a direct search for excess events from ν_e at low energies in the same BNB beamline as MiniBooNE. MicroBooNE was the first phase of the SBN program located at a baseline of 470 meters between the Short Baseline Near Detector and the ICARUS Far Detector, as can be seen in Figure 1.7.

The MicroBooNE detector is composed of a single TPC volume of 2.6 m width, 2.3 m height, and 10.4 m length in the beam direction, housed within a cylindrical cryostat as shown in Figure 1.10. MicroBooNE operated with a nominal electric field of 272 V/cm which was lower than the target electric field of 500 V/cm due to instabilities in the cathode high voltage. With this, ionized electrons drift at a velocity of $\sim$1.1 mm/μs corresponding to a drift length of 2.53 m and a maximum drift time of 2.3 milliseconds. Similar to SBND and ICARUS, MicroBooNE has three wire planes oriented at $\pm 60^\circ$ and 0° from the vertical, with a total of 8,256 wires. 32 PMTs are situated behind the anode wire plane to detect the scintillation light in the liquid argon. Positioned at shallow depth, MicroBooNE is exposed to a large background of cosmic ray muons. This persistent cosmogenic background will be discussed more in Section 2.2, but it becomes more challenging to remove with MicroBooNE's longer drift time of 2.3 ms. Because of this, a cosmic ray tagging (CRT) system was installed after the first data run. The CRT system was designed by the Laboratory for High Energy Physics (LHEP), Albert Einstein Center for Fundamental Physics, University of Bern and uses 73 modules made of plastic scintillator surrounding the MicroBooNE detector to provide time and position information for cosmic particles traversing the TPC, with a coverage of 4π (85%). Similarly, SBND and ICARUS both have dedicated CRT systems that will be described in Section 1.2.4 and Chapter 4 respectively.

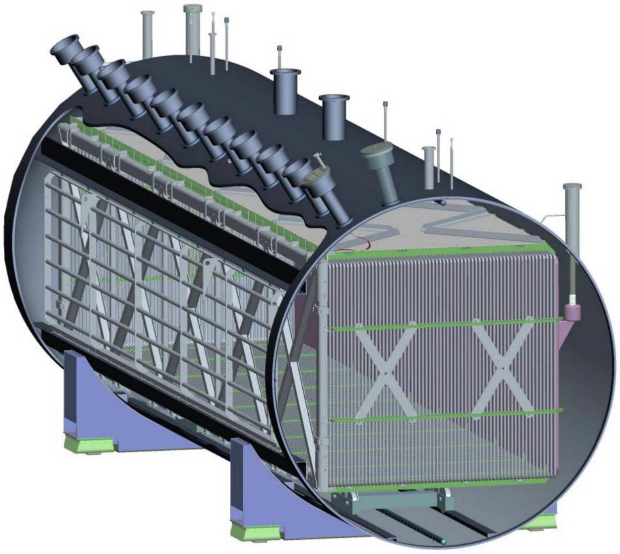

(a) Schematic diagram of the MicroBooNE detector.

(b) Exterior view of the cathode frame.

Figure 1.10: The MicroBooNE detector. Figures taken from [8].

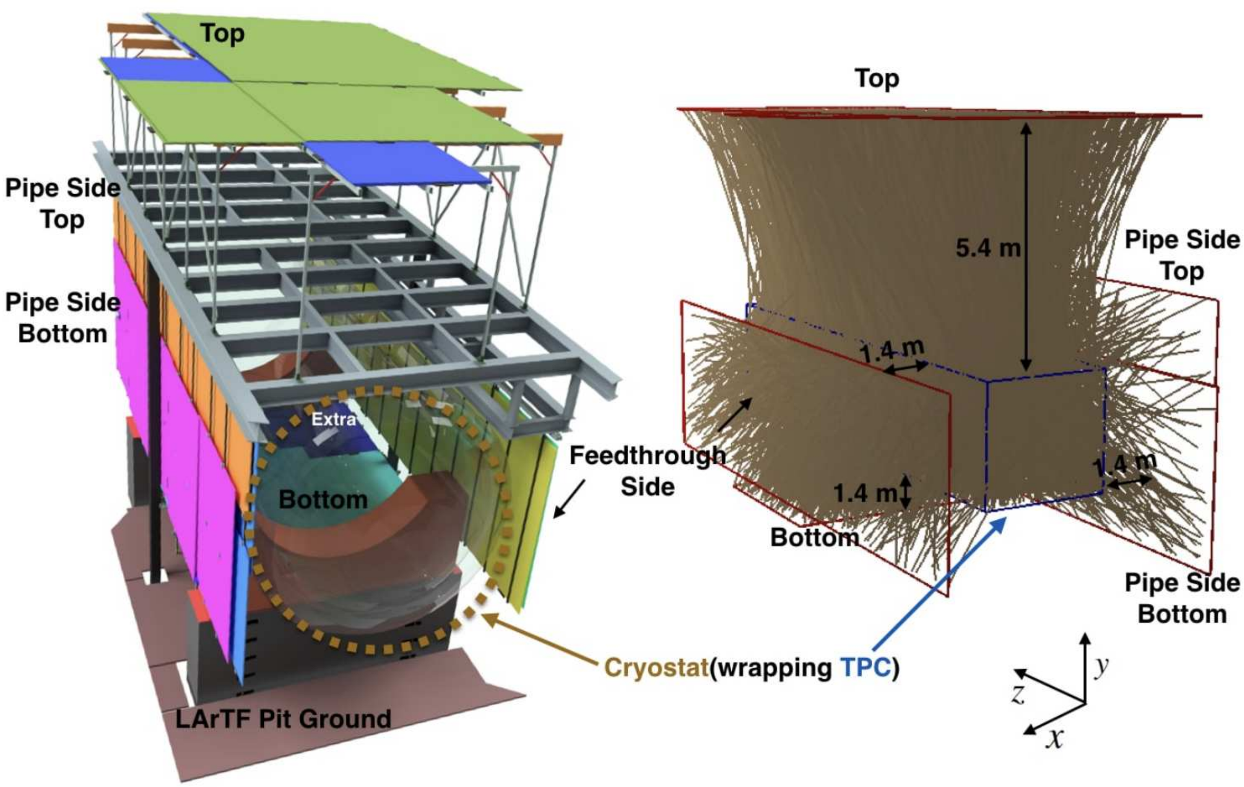

Figure 1.11: MicroBooNE CRT design. On the right, the brown lines represent possible cosmic ray trajectories from a simulation of cosmic rays crossing the CRT. Figure from [9].

The MicroBooNE experiment operated from 2015 to 2020, accumulating over 1.3×10^{21} Protons-on-Target (POT). MicroBooNE used a novel, data-driven technique to evaluate detector-related uncertainties [43], which is being adopted in ICARUS and will be discussed in more detail in Chapter 5. Using the beam bunch structure, MicroBooNE was the first LArTPC detector to demonstrate O(1 ns) timing resolution [44]. Precise timing resolution is a large focus of this thesis and will be covered in Chapter 6. The collaboration carried out a variety of physics analyses including detector performance and LArTPC technology development [45–49], neutrino cross-section measurements, dark matter sensitivities [50] and extensive searches related to the MiniBooNE low energy excess. MicroBooNE announced their first low energy excess results in 2023 using just 6.37×10^{20} POT [51] and reported no evidence of light sterile neutrino oscillations. More recently in 2025, the collaboration published a first search for e^+e^- explanations of the MiniBooNE anomaly, and excluded a majority of the parameter space [52], with results reported with a 95% confidence level.

1.2.4 Short-Baseline Near Detector

The SBND detector was moved to the detector hall in December 2022 and the liquid argon fill was completed February-March 2024. A picture of the detector being lowered into the cryostat is shown in Figure 1.12. SBND recorded its first neutrino interactions in early July 2024. Located just 110-meters from the neutrino beam target, SBND sees unprecedented neutrino statistics, recording nearly 7000 neutrinos per day from the BNB with nominal operations. The detector has 112-tons of liquid argon in the $4 \times 4 \times 5\text{m}^2$ active volume. SBND has a central cathode that splits the detector into two drift volumes, with the cathode plane held at 100 kV. A field cage surrounds the detector to provide a uniform electric field of 500 V/cm. Similar to MicroBooNE and ICARUS, the anode wire plane has wires oriented at $\pm 60°$ and $0°$ from the vertical with a 3 mm wire spacing, and has $\sim$11,000 readout wires in total.

The SBND Photon Detection System (PDS) can be seen in Figure 1.13. A single SBND PDS module houses 5 PMTs and 8 X-ARAPUCA devices, with 12 on each anode wall for a total of 24

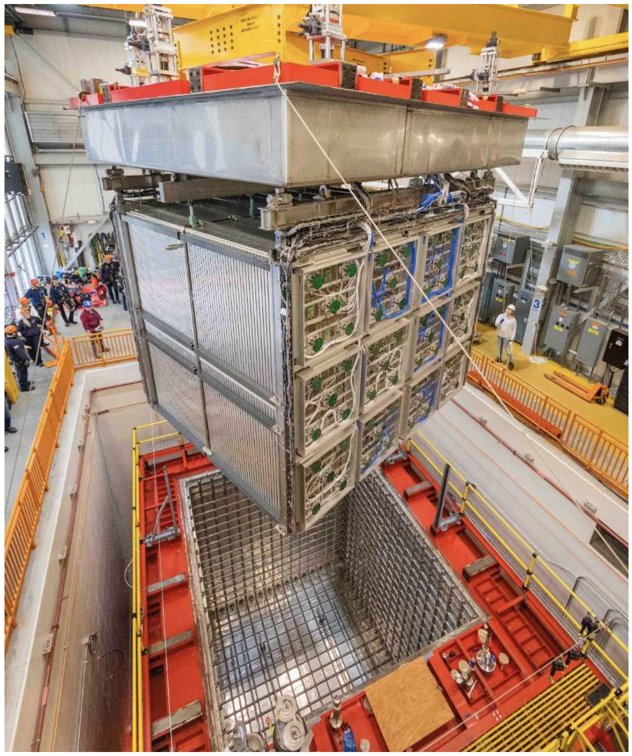

Figure 1.12: The Short Baseline Neutrino Detector (SBND) being lowered into the cryostat at FNAL, with the detector shown hanging from the cryostat lid. Picture from April 2023.

PDS modules (120 8-inch Hamamatsu PMTs and 192 X-ARAPUCAs). SBND uses both uncoated and coated PMTs and X-ARAPUCAs to be sensitive to both vacuum ultraviolet and visible light. Additionally, SBND has a CRT system surrounding the detector cryostat to tag incoming cosmic rays. The CRT system is composed of 7 individual walls shown in Figure 1.14, with a total of 146 modules made up of scintillator strips readout with silicon photomultiplier tubes (SiPMs).

SBND collected its first physics run from December 2024 - July 2025, is currently collecting data for Run-2 and has already accumulated the world's largest neutrino-on-argon dataset. Together with ICARUS, SBN program will be able to definitively confirm or refute the existence of a $\Delta m^2 \sim 1\text{eV}^2$ mass sterile neutrino at Short Baselines.

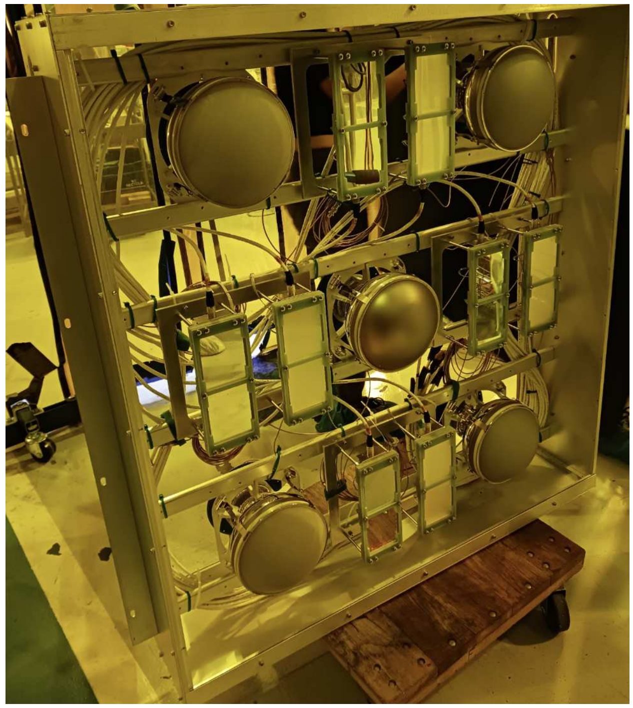

Figure 1.13: A single SBND Photon Detection System (PDS) module comprised of 5 PMTs and 8 X-ARAPUCA devices. Each anode wall has 12 PDS modules, with a total of 24 PDS modules for light detection in the TPC.

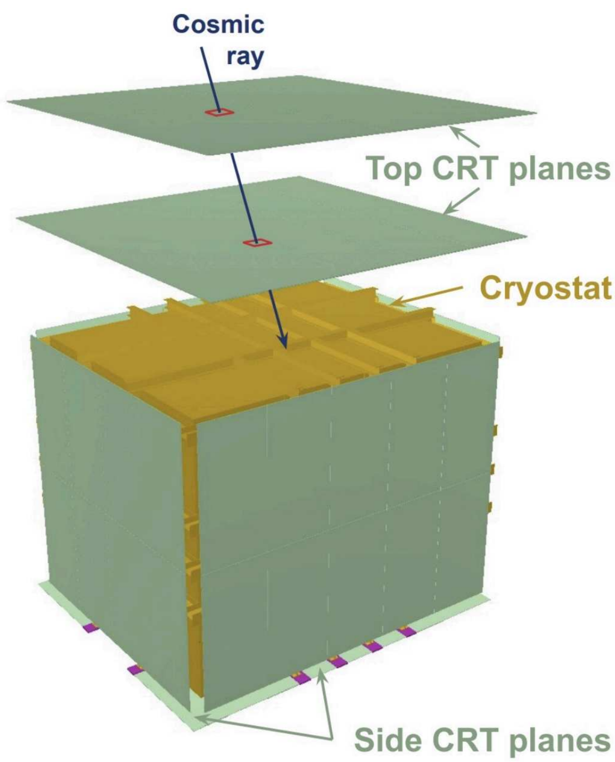

Figure 1.14: The SBND Cosmic Ray Tagger (CRT) system composed of 7 CRT walls with 146 modules.

Chapter 2

The ICARUS-T600 detector

ICARUS (Imaging Cosmics and Rare Underground Signals) is the world's first large-scale LArTPC detector containing 760 tons of ultra-pure liquid argon. ICARUS' spokesperson, Carlo Rubbia, first proposed the concept of a large-scale LArTPC in 1977 [39], and the ICARUS Collaboration designed and built the first prototypes with successively larger size following many years of research and development.

This chapter starts by outlining the history of the ICARUS detector (Section 2.1), where the initial operation gave the detector its name. I then discuss the cosmogenic background ICARUS is exposed to at Fermilab and methods to mitigate this persistent background in Section 2.2. The commissioning and installation of the ICARUS detector is covered in Section 2.3 and an overview of our collected physics runs is provided in Section 2.4.

2.1 ICARUS: From Italy to CERN to Fermilab

ICARUS began as a standalone R&D program dedicated to demonstrating the feasibility of operating a large-scale LArTPC. Initial tests started in 1993 with a 3-ton LAr prototype collecting events from cosmic rays and a monochromatic gamma ray source [53] continuously for more than 4 years. In 1997 a larger prototype of 14 tons of LAr, referred to as the 10^3 module, was built. After completing cooling and filling tests at Pavia in July 1999, the detector was moved to a surface location at Gran Sasso National Laboratories (LNGS) collecting cosmic ray data from January to June 2000. In parallel to the tests, the design and construction for scaling up to the next prototype of 600 tons, referred to as a T-600, lasted for about 4 years. In 2001, one of the 300-ton modules (a T-300, one half of a T-600) was brought into operation and ran for 3 months on the surface at LNGS exposed to cosmic rays. The detector was decommissioned following this initial test and in 2004, the full detector (two T-300s) was brought underground to Hall B of LNGS and started collecting neutrinos from the CERN Neutrinos to Gran Sasso (CNGS) beam. From October

2010 to December 2012, a total of about 3,000 neutrino events were collected, corresponding to 8.6×10^{19} Protons-on-Target (POT). Beyond demonstrating the practicality of running a large-scale LArTPC, the ICARUS physics program was focused on studying atmospheric, solar and long baseline neutrinos, as well as proton decay. The collaboration performed a search for ν_e appearance in an almost pure ν_μ beam, setting limits on the $\nu_\mu \rightarrow \nu_e$ oscillation probability [54]. Additionally ICARUS measured the velocity of neutrinos from CNGS, disproving the claim that neutrinos move faster than the speed of light from the OPERA experiment [55] using the same neutrino beam source.

After a successful 3-year operation at Gran Sasso, the ICARUS-T600 detector was transported to CERN for upgrades including:

- New cryogenic cold vessels with passive insulation.
- Updated cryogenics and LAr purification equipment.
- Flattening of the TPC cathode (the punched hole stainless-steel panels underwent a thermal treatment improving the planarity to a few mm).
- New, higher performance TPC read-out electronics.
- New LAr light detection system with improved coverage (5% coverage).

See Figure 2.1 for a fisheye view inside of one of the ICARUS T300 detectors while being refurbished at CERN. A single T-300 module is composed of a central perforated cathode with two drift regions, each read out by an array of PMTs.

ICARUS was shipped to Fermilab in July 2017 following the overhauling at CERN. In August 2018, the two ICARUS modules were placed into their final position in the cryostat in the SBN Far Detector building shown in Figure 2.2. See Figure 2.3 for a view of one of the T-300 detectors being lowered into the warm vessel at the SBN-Far Detector building at FNAL.

Figure 2.1: A fisheye view inside one of the ICARUS T300 during upgrades at CERN. The two TPCs are separated by a perforated cathode shown on the left side of the image, with the PMTs and wire-planes located on the right hand side and the field cage on the top and bottom of the TPC. Figure courtesy of CERN.

Figure 2.2: The Short Baseline Far Detector building at Fermilab designed by Holabird & Root architecture firm. The front face mimics the perforated cathode in ICARUS and shows an example event display. Photograph taken by the author.

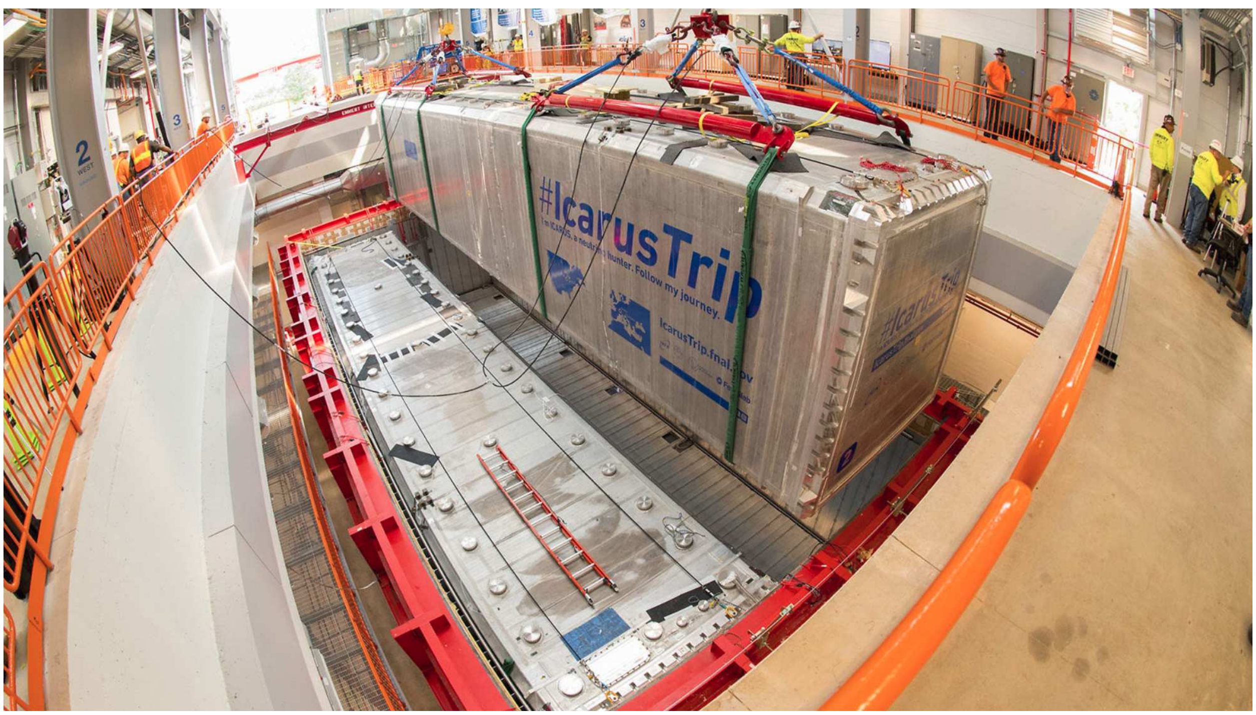

Figure 2.3: A ICARUS T-300 module being lowered into the warm vessel in the Short Baseline Far Detector building at Fermilab. Photo from Fermilab Creative Services.

2.2 Cosmic Ray Background

Surface operation of ICARUS poses new challenges due to the cosmic ray background. When a high-energy cosmic ray particle, typically a proton, collides with the upper atmosphere, it creates a shower of particles that transverse down to the Earth's surface. These particles can interact in the detector and potentially mimic a neutrino signal, providing a challenging background in neutrino experiments. Electromagnetic showers produced by cosmic particles propagating through or near the detector are important backgrounds for a ν_e CC analysis, as a photon can be mistaken for an electron. In comparison to ICARUS' operation in the Gran Sasso laboratory where it was situated under a mountain to substantially reduce backgrounds, the detector is now operating at shallow depth at Fermilab and exposed to a large background of cosmic activity. On average, about 13 cosmic muon tracks are expected per triggered event in the 0.96 ms TPC drift readout.

To combat this persistent background, a concrete overburden is installed to stop and block the cosmic rays before they reach the detector and a Cosmic Ray Tagging (CRT) system tags the remaining incoming charged particles with precision of a few nanoseconds. I assisted CSU post-doctoral researcher, Biswaranjan Behera, with studies on the impact of the concrete overburden on reducing the cosmic ray flux. The effectiveness of a ~2.85 m (6 m water equivalent) concrete overburden was studied by producing samples of CORSIKA cosmics simulated with and without a concrete overburden included in the detector geometry, and comparing the simulated rates. CORSIKA will be discussed in more detail in Chapter 5. Another CSU graduate student, Tyler Boone, and I assisted in these studies by simulating CORSIKA events over a total exposure time of 211 s (corresponding to 3 years of data taking, $\sim 6.6 \times 10^{20}$ POT exposure with 5×10^{12} protons / spill) with and without a concrete overburden at Fermilab's elevation. 10,000's of Monte Carlo files were produced using the Fermilab Computing Grid to run the production of these files. Figure 2.4 shows the impact of a concrete overburden on the spectrum of cosmic primaries that enter the ICARUS TPCs. The overburden reduces the dominant muon flux by $\sim 25\%$, effectively blocking primary cosmic muons with kinetic energy $E_K < 1.5$ GeV. The overburden is even more effective

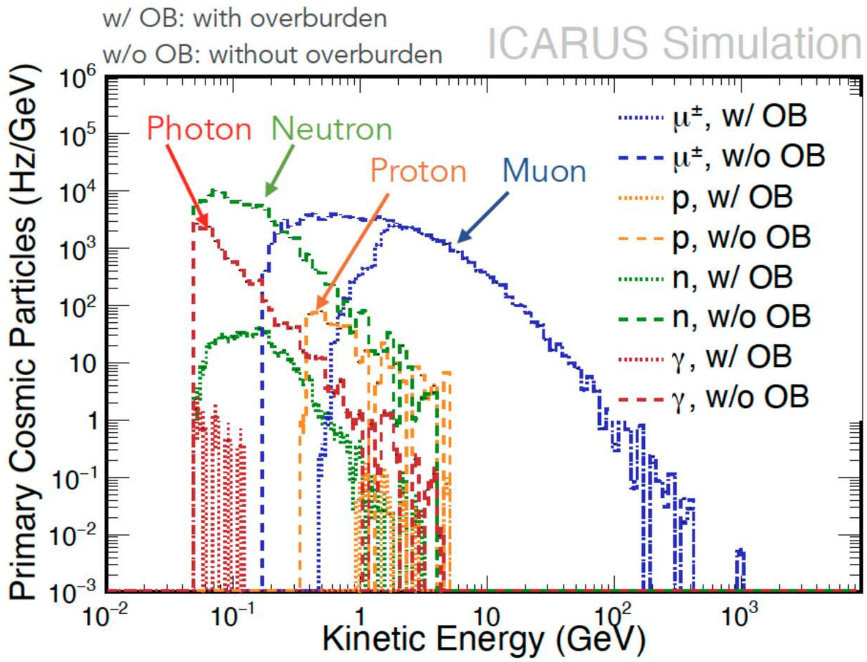

Figure 2.4: Impact of a concrete overburden on the spectrum of cosmic primaries reaching the ICARUS TPCs for various particles over a 211 s exposure. A 6.6×10^{20} POT exposure with 5×10^{12} protons / spill results in 211 s of total integrated beam-on time. Figure from [10].

at suppressing the hadronic component of the flux, reducing cosmogenic protons by a factor of 500 and dramatically stopping cosmogenic neutrons (99.5% reduction in the 1 ms drift window).

The number of γ initiated electromagnetic showers with and without a concrete overburden is shown in Figure 2.5 for a 3-year exposure for various cosmic primaries. Only showers above 200 MeV are considered as potential background as that is the threshold used for a ν_eCC selection in the SBN Proposal [5]. The background due to γ initiated electromagnetic showers is almost completely removed with an $\sim$ 3 m concrete overburden.

These studies motivated the installation of the concrete overburden; see Figure 2.3 for pictures from the overburden installation. A CRT system compliments the overburden by tagging cosmogenic particles that were not stopped in the concrete. The CRT system is composed of three subsystems, a Top, Side, and Bottom CRT, and will be covered in detail in Chapter 4.

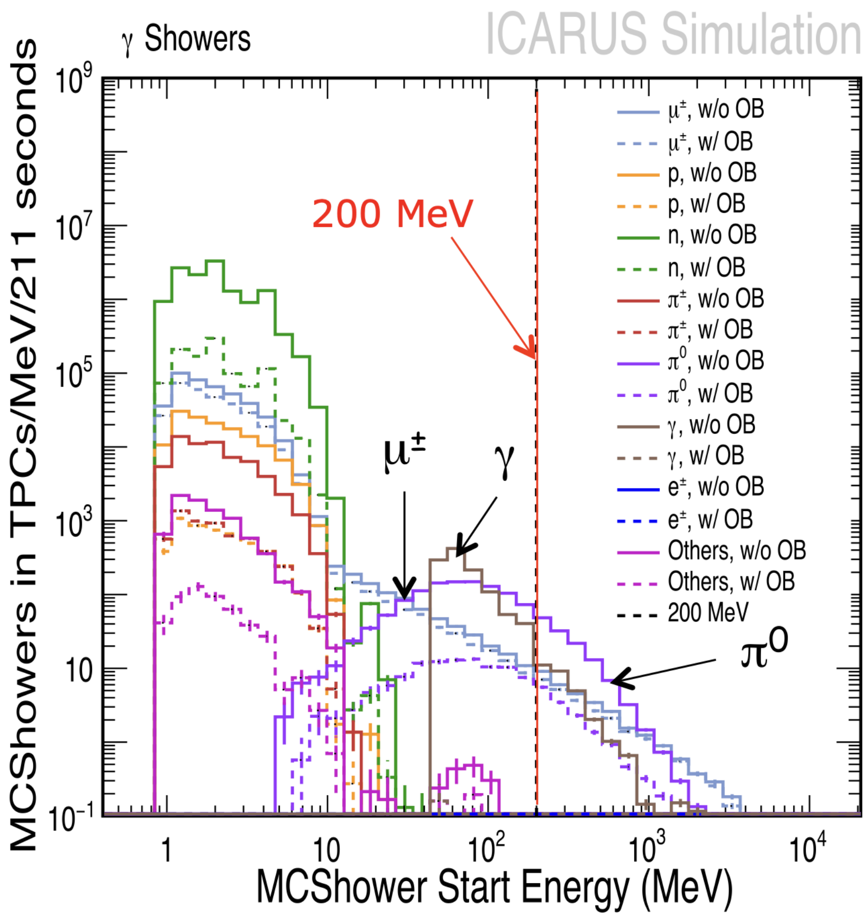

Figure 2.5: γ initiated electromagnetic showers with and without a concrete overburden, for a 221 s ($\sim 6.6 \times 10^{20}$ POT) exposure.

2.3 Commissioning and Initial Operations

ICARUS detector commissioning activities at FNAL started in August 2018, following the placement of the two T-300 modules in the pit in the SBN-FD building. The PMT and TPC subsystems were deployed and initial tests took place to monitor the gain and dark rate in the PMTs and the noise in the TPCs. The cryogenic system was installed by July 2019 and commissioning began January 2020. The argon filling was completed, along with the liquid argon recirculation system, by May 2020. For more details on the ICARUS cryogenic plant, see [11]. The detector was first activated in August 2020, when the TPC wire planes and cathode high voltage (HV) were taken to nominal voltage. See [56] for a detailed overview of the overhaul and installation of the TPC electronics.

The first cosmic ray events at FNAL were recorded with ICARUS with a random 5 Hz trigger and used for calibration purposes. The Bottom CRT was installed below the cryostat in the before the warm vessel was placed in the SBN-FD hall. During 2020 and 2021, the Side CRT system was installed with a large participation from Wilson's group at CSU. Top CRT installation completed December 2021. The CRT installation and commissioning will be covered in Chapter 4 after the full CRT subsystem is described in detail. The first FNAL neutrinos were collected with ICARUS in June 2021, just before the summer shutdown.

In January 2021, I led a neutrino event scanning group with TITUS event display using first beam data collected by the ICARUS detector at FNAL. Working with INFN-Padova collaborator Christian Farnese, I organized and collected events from the US university group of scanners. This activity identified some of the first neutrino interaction candidates in the ICARUS detector based at FNAL, demonstrating that the ICARUS detector subsystems were working properly, and neutrinos can be identified and reconstructed in the LArTPC. For an example of a visually selected candidate, see Figure 2.6. This effort also helped identify some TPC channel mis-mappings that are important to recognize and correct during the commissioning phase.

The concrete overburden installation started in April 2022 following the Top CRT commissioning. The overburden has three layers of concrete blocks, each about 1 meter tall, amounting

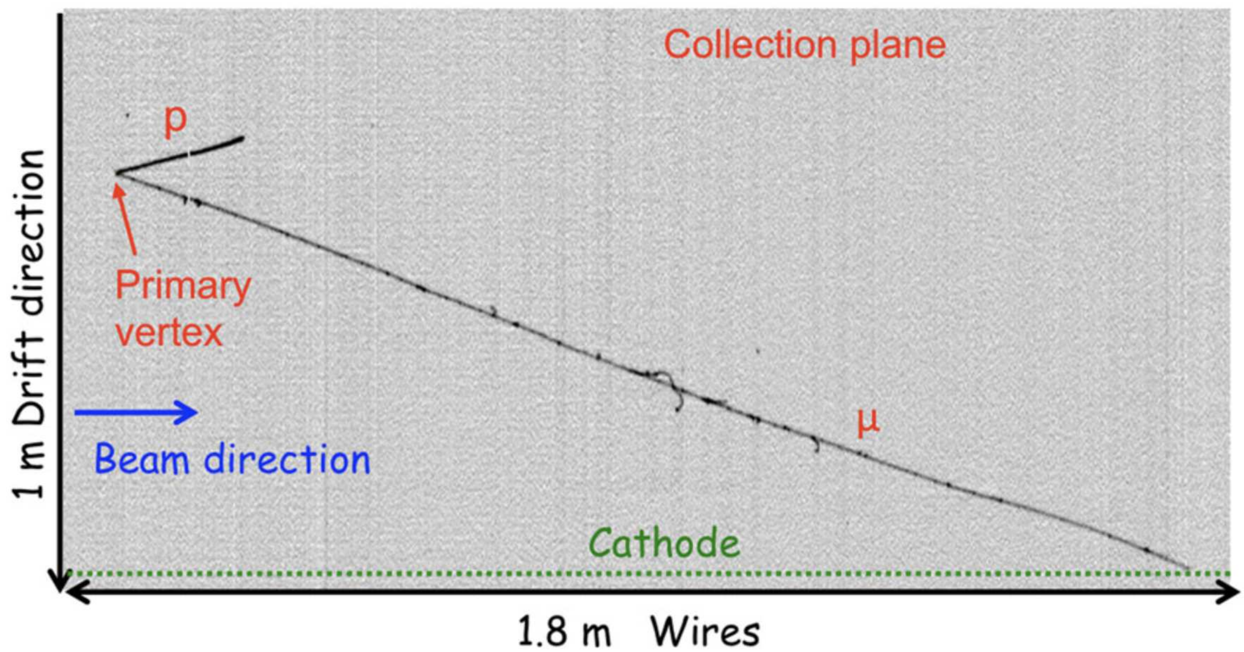

Figure 2.6: Visually selected ν_μ CC candidate from the BNB beam identified from the scanning effort from [11].

to 2.845 m (or 6 meter water-equivalent). The concrete blocks were tested with a Geiger counter before installation to ensure low radioactivity. The first concrete block of the first layer of the overburden can be seen lowered on top of the detector in Figure 2.7. This was a nerve-wracking experience considering these heavy concrete blocks were being installed just 10 cm above the Top CRT modules and the delicate detector equipment installed directly below. The last concrete block was placed on June 7, 2022, with the fully installed overburden shown in Figure 2.8. Data was collected during the installation of the overburden to see the effect on the cosmic ray rate in the CRTs. The impact in the Top CRT data rates can be seen in Figure 2.9, where a clear reduction in the trigger rates is seen with each subsequent layer installed.

2.4 Physics Runs

ICARUS' first physics run officially started June 8th, 2022 and lasted for one month before the regular summer shutdown, collecting a total of 2.96×10^{20} and 5.03×10^{20} Protons-on-Target (POT) for BNB and NuMI beams respectively. POT is a how we quantify how much beam was

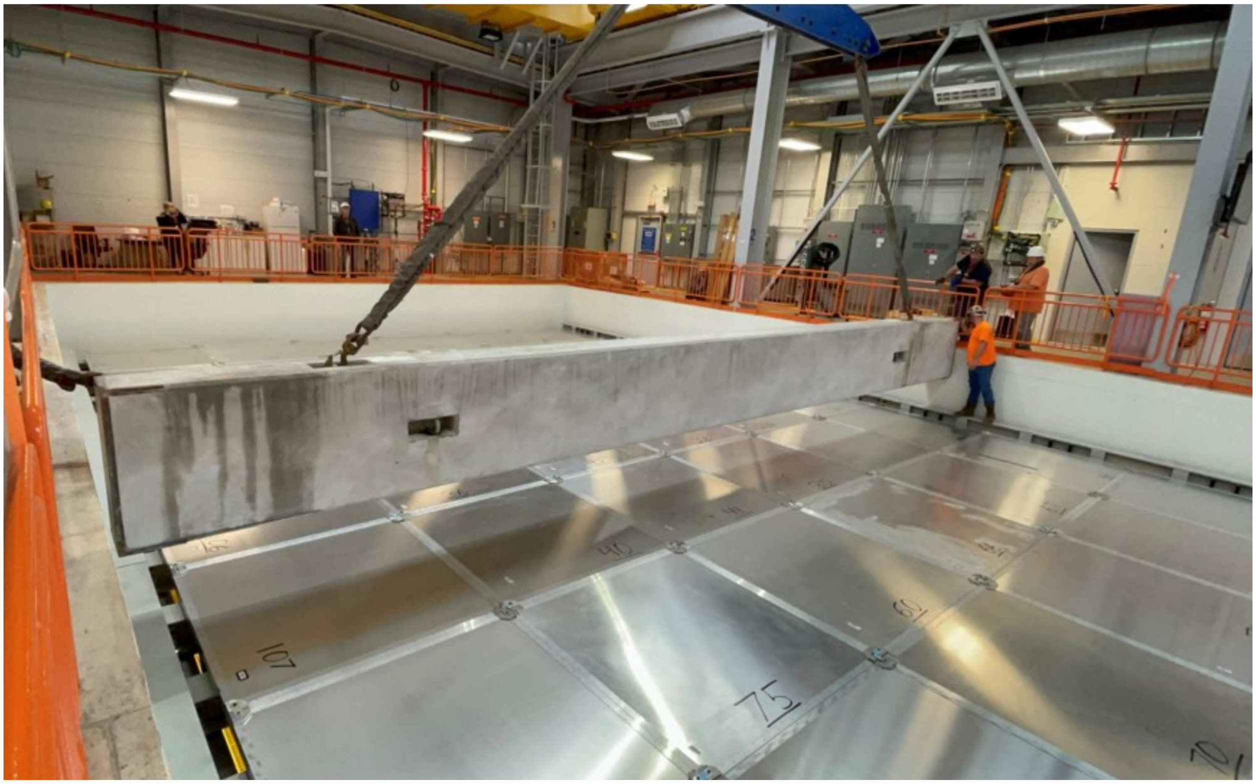

Figure 2.7: First block of first layer of concrete overburden being installed above the ICARUS Top CRT.

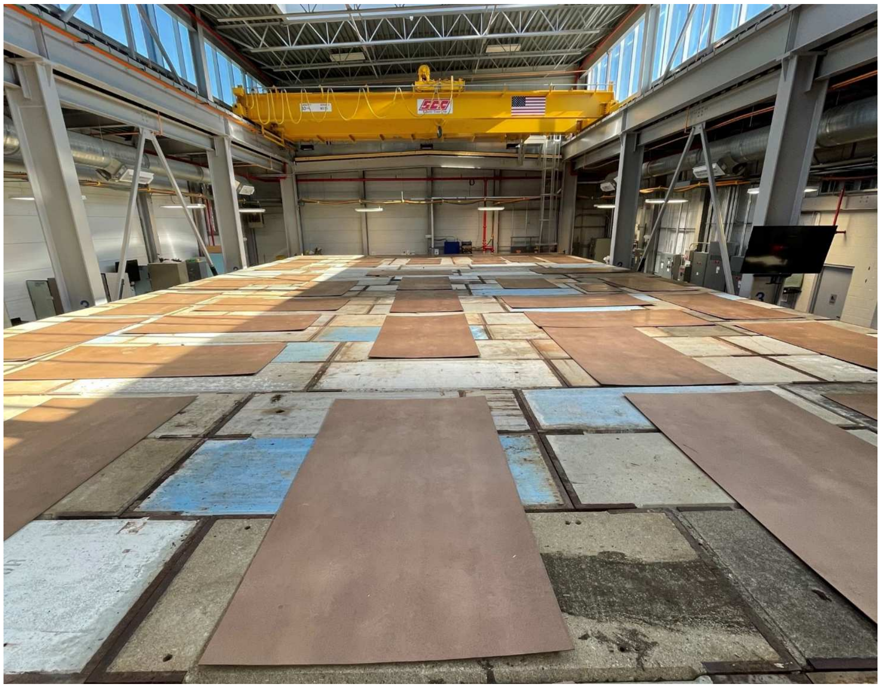

Figure 2.8: Fully installed concrete overburden.

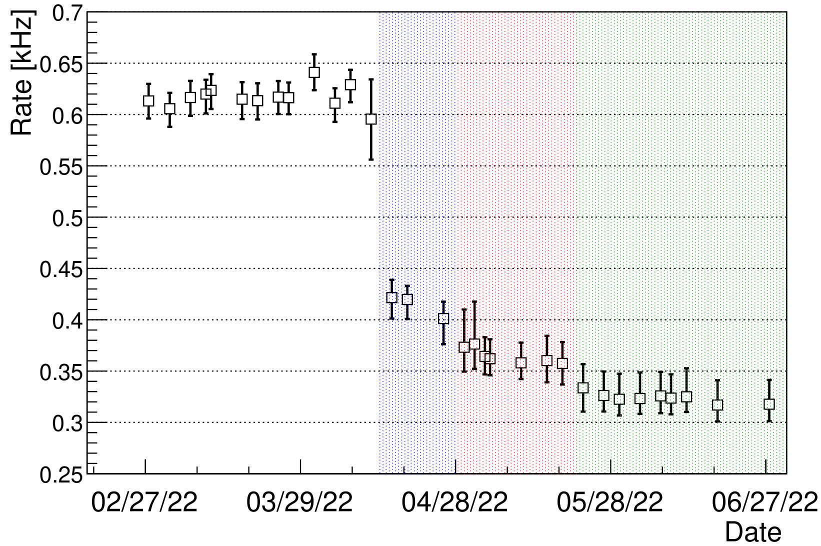

Figure 2.9: Top horizontal CRT Trigger Rate as a function of time, with color bands showing the progress of the overburden installation: first layer (blue), second layer (red) and third layer (green). Figure taken from CRT Technical Note [12].

delivered. ICARUS is now collecting data for its 5th data run, collecting a total of 10×10^{20} and 6.30×10^{20} POT for BNB and NuMI respectively, see Figure 2.10. For a POT collected across the various runs, see Table 2.1. In general, I will use upper case "Run" to refer to our neutrino beam runs and lower case "run" to refer to our data acquisition (DAQ) run numbers.

Since data collection started, the ICARUS collaboration has done extensive calibration work preparing for our first physics analyses. For the TPC, detailed noise studies and characterizations

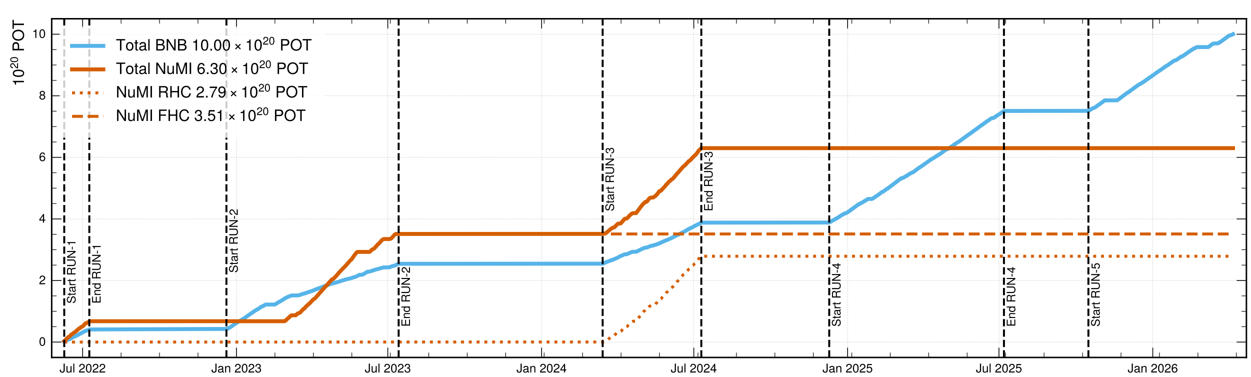

Figure 2.10: Protons-on-Target (POT) collected by ICARUS Physics Runs at Fermilab up to April 8th, 2026.

Beam Run	DAQ run numbers	BNB POT (x10^{20})	NuMI POT (x10^{20})
Run-1 (6/8/22 - 7/9/22)	8460 - 8554	0.41	0.68
Run-2 (12/20/22 - 7/12/23)	9301 - 10097	2.05	2.74
Run-3 (3/14/24 - 7/12/24)	11806 - 12037	1.36	2.82
Run-4 (12/10/24 - 7/8/25)	12962 - 13271	1.37	-
Run-5 (10/16/25 - ongoing)	13758 - ongoing	4.81	-
Total		10	6.30

Table 2.1: Run periods with dates, DAQ run numbers, and total collected POT for the various ICARUS Runs. Units are in x10^{20} POT. Note the POT shown for NuMI is the sum of FHC+RHC (neutrino and antineutrino mode). NuMI was not operational from 2024-2026.

were carried out [18]. The data-driven calibration and simulation of the TPC will be covered in Section 5.1.2. [57] demonstrates a clear angular dependence of recombination electron-ion recombination.

Since the beginning of neutrino beam data taking, ICARUS has carried out a number of physics analyses. The first physics result released from the collaboration was a search for Long Lived Particles (LLPs) hypothesized as being produced from kaon decays in the NuMI beam traveling a distance to the ICARUS detector and decaying into two Standard Model particles inside the TPC [58]. Prior to the SBND detector turning on, the ICARUS collaboration focused on a muon neutrino disappearance search using Run-2 BNB data. Performing this first oscillation analysis with a single detector helps lay the groundwork for future, more sensitive SBN analyses. These results were presented a Fermilab Wine and Cheese seminar on January 9th, 2026, with the analysis paper published on arXiv [59] and recently submitted to Physical Review D.

For this thesis work, I will largely focus on BNB data from Run-2 and Run-4, although BNB data from Run-3 and Run-5 was also studied. Run 2 was collected from December 2022 - July 2023 with $\sim 2.13 \times 10^{20}$ and $\sim 2.84 \times 10^{20}$ POT from BNB and NuMI respectively. For Run 4 from December 2024 - July 2025, the NuMI beam was off and $\sim 3.63 \times 10^{20}$ POT was collected from BNB, corresponding to roughly $\sim 4 \times 10^{5}$ neutrino interactions expected to trigger the ICARUS-T600 detector from BNB alone. When NuMI is running, the Booster beam is bunch rotated [60] to match the Main Injector frequency which results in the beam bunch spreading out in time [60].

Bunch rotation is a method the accelerator uses to modify the particle bunch's shape in phase space and is needed to provide a high intensity beam to NuMI. More details will be provided in Chapter 6. With the NuMI beam off for ICARUS' fourth data run, the intrinisc bunch width should be smaller in ICARUS Run-4 data compared to Run-2 data. As discussed in more detail in Chapter 6, I will use both BNB Majority and BNB Minimum Bias stream datasets, with the various data streams described in Section 3.3. For this work I focused on demonstrating these techniques with the BNB beam, but the analysis techniques apply to the NuMI beam as well.

Chapter 3

ICARUS Photomultiplier and Trigger System

The ICARUS Photomultiplier system is made up of 360 8” Hamamatsu R5912-MOD Photomultiplier Tubes (PMTs) mounted behind the TPC wire planes, with 90 PMTs per TPC. PMTs detect scintillation light from charged particles interacting in liquid argon (see Section 3.1), where the fast scintillation light is used to reconstruct the position of the event along the charge drift direction. The PMTs are arranged in a honeycomb pattern mounted on the wire chamber mechanical frames about 5 mm behind the Collection wire plane. To mitigate induction of fake signals from PMT signals on nearby wire planes, the PMTs are housed within a stainless steel grid cage. A laser calibration system is used for gain equalization, timing, and monitoring of all PMTs. The PMTs are connected to 24 CAEN V1730B digitizer boards in 8 crates with 3 boards per crate. Each board reads out 15 PMTs with a spare channel used to digitize external timing signals from the Accelerator Division which will be described in detail in Section 6.2.

In this chapter, I introduce scintillation light timing mechanisms in Section 3.1 and calibrations to achieve a timing equalization well below 1 nanosecond are described in Section 3.2. I describe how the PMTs are used as the trigger system for the full ICARUS detector in Section 3.3 and discuss trigger rates and efficiencies across the various beam runs.

3.1 Scintillation Light Timing

Charged particles traversing the liquid argon can excite or ionize argon atoms that then pair with neutral argon atoms, producing excited or ionized argon dimers. Ionized dimers, Ar_2^+, are produced if the energy transfer is enough to free an electron from a parent argon atom, whereas excited dimers, Ar_2^*, are formed when an incoming charged particle transfers energy to the argon atom but not enough to free an electron. Ionized dimers eventually recombine with a free electron to produce, Ar_2^*. In both processes, the excited argon dimer subsequently decays, producing two argon atoms and a 128-nm scintillation photon. The excited dimer may exist as a singlet or a triplet

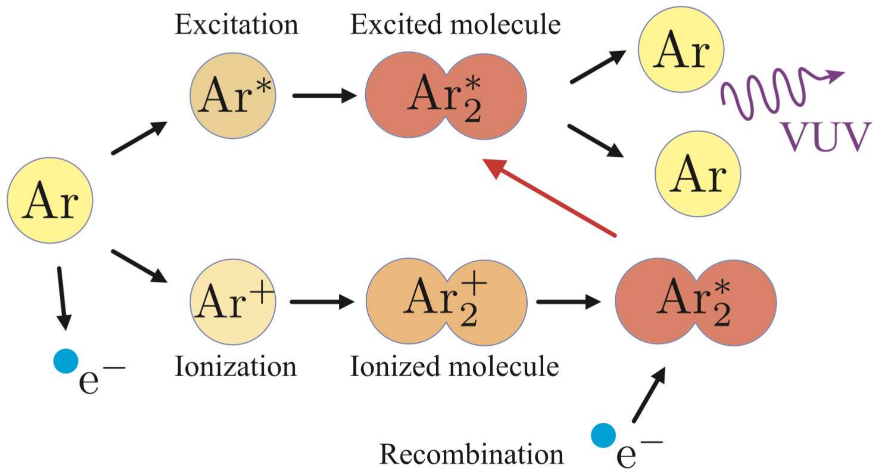

Figure 3.1: Cartoon of scintillation and ionization mechanisms in liquid argon from [13].

spin state, and this determines the lifetime of the decay and timescale on which the scintillation light is emitted. In liquid argon, the singlet state decays fast with a lifetime of $\mathcal{O}(6\ \mathrm{ns})$, whereas the triplet state decays much slower with a lifetime of $\mathcal{O}(1.5\ \mu\mathrm{s})$. A cartoon of the scintillation and ionization mechanisms in liquid argon is shown in Figure 3.1. As the scintillation light is produced in the vacuum ultraviolet (VUV), each PMT is coated with wavelength shifting tetraphenyl butadiene (TPB) to convert the scintillation photons to visible light.

3.2 PMT Timing Calibration

To achieve a timing resolution below a nanosecond, three different timing corrections are performed for the PMT system: a hardware trigger correction, a laser correction, and a cosmic rays correction. The hardware trigger correction removes the internal ∼16 ns timing jitters between the CAEN readout boards and the trigger hardware by using additional external signals as a time reference, aligning the PMT times with a sampling precision of 2 ns. For the laser corrections, a dedicated laser system composed of a Hamamatsu PLP10 laser diode that generates pulses (λ = 405 nm, FWHM = 60 ps) is used for calibration of the PMT system. The laser pulses are distributed to each PMT through optical fibers, light splitters and optical feed-through flanges. Recent upgrades were made to distribute the laser light pulse to all PMTs within the same run by replacing the optical switch with an optical splitter [61].

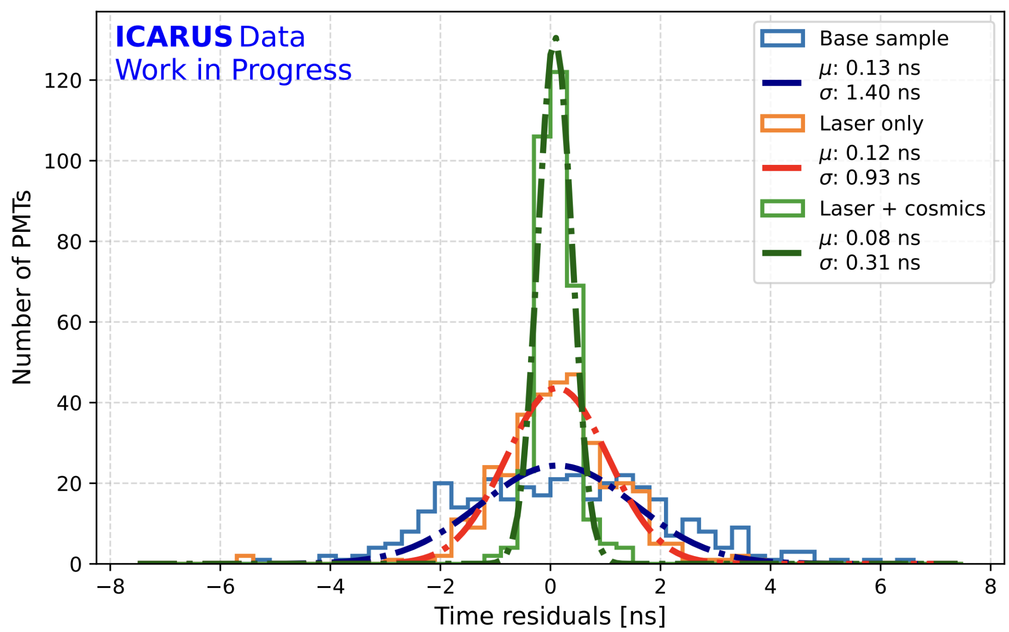

Figure 3.2: PMT Timing Residuals after each timing correction from [14]. The base sample shown in blue is after a hardware trigger correction, orange/red shows the sample after a laser correction, and the green sample is after the laser and cosmic rays corrections were applied, with a final timing equalization of $\mathcal{O}(300\ \mathrm{ps})$.

The large source of cosmic rays impinging on the ICARUS detector operating on the surface are used as a final timing equalization of the PMTs. By selecting a source of downward-going cosmic muons, timing residuals are extracted for each PMT channel to align the PMT times. With these three consecutive corrections in place, the PMT system achieves a time resolution well below 1 ns (∼300 ps), as shown in Figure 3.2 from [14].

3.3 PMTs as Detector Trigger

ICARUS collects various PMT-based trigger types for both BNB and NuMI beams, and off-beam for calibration. The two main trigger types are a Majority and Minimum Bias trigger collected either in coincidence with the BNB/NuMI beam spills (on-beam) or in between spills (off-beam) (see Figure 3.3 and Figure 3.4). The Majority trigger is based on discriminated PMT signals above a set threshold, while the Minimum Bias trigger fires when there is a gate with no requirement on the scintillation light. The on-beam Majority data is the primary trigger for beam physics, looking for PMT light flashes from the BNB or NuMI beam spills (1.6 µs and 9.5 µs respectively).

Beam Run	BNB on-beam	BNB off-beam	NuMI on-beam	NuMI off-beam
Run-1/Run-2	200	20	60	20
Run-3/Run-4	40	20	30	20

Table 3.1: Minimum Bias pre-scale factors used for the various ICARUS beam runs.

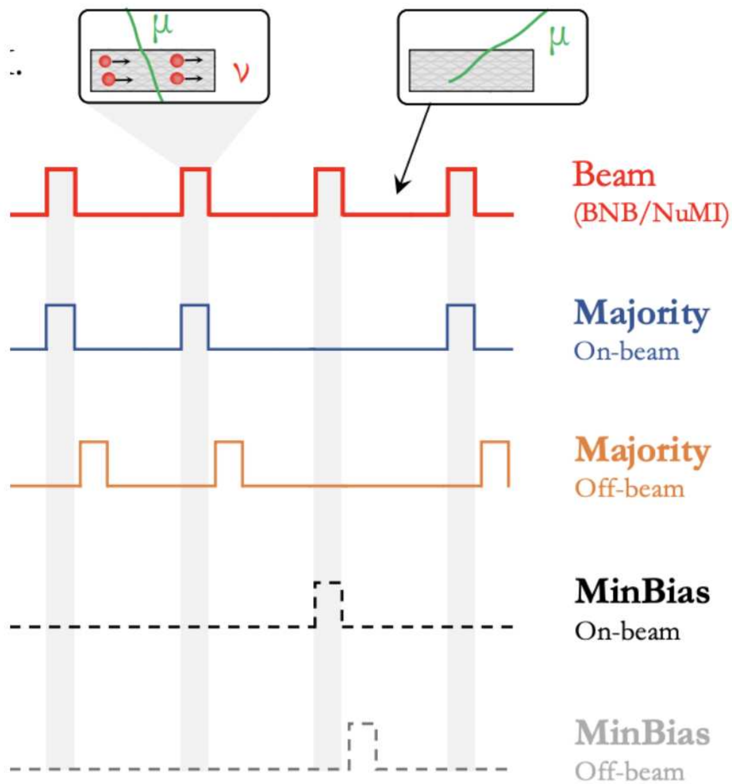

Figure 3.3: Various trigger types collected with the ICARUS detector. The gray band represents an example beam gate where the on-beam triggers are fired and off-beam triggers are collected in between gates.

The off-beam Majority provides a sample of cosmic ray events. The Minimum Bias data provides an unbiased data sample.

This pre-scale factor varies for the different ICARUS runs and helps minimize the impact on the Majority beam data triggers, while still collecting a sample of unbiased triggered data. The different pre-scale factors used in various ICARUS beam Runs is shown in Table 3.1. These unbiased data provide a sample to validate and cross-check the performance of the Majority trigger, and are used for calibrations and detector physics studies.

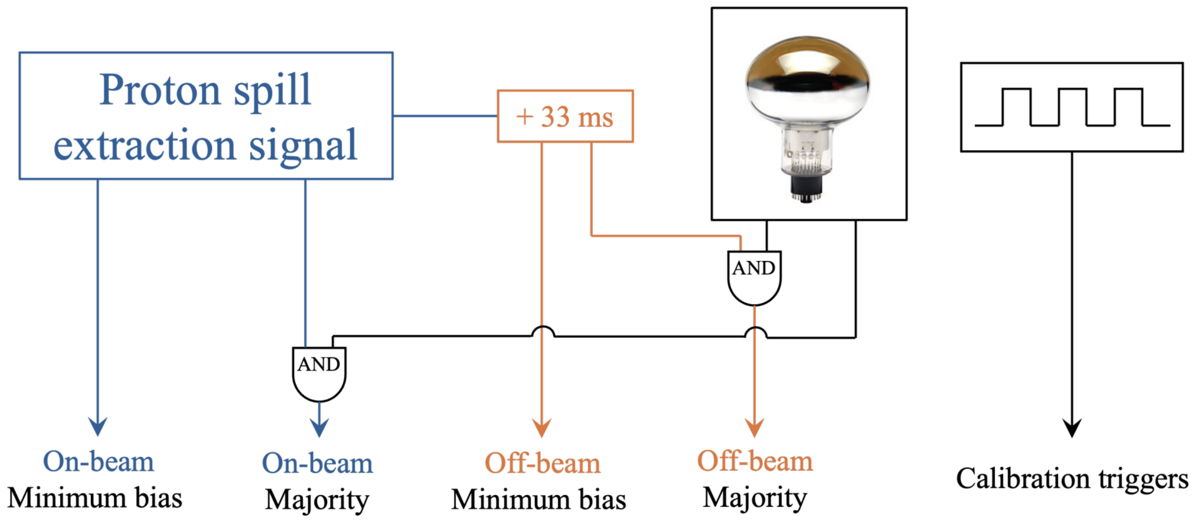

Figure 3.4: Logic for how the various trigger types are collected with the ICARUS detector. Figure from [15].

The average trigger rate for ICARUS is ∼0.7 Hz, including contributions from both the BNB and NuMI Majority components and Minimum Bias triggers. For Run-2, trigger rates from the Majority components (on-beam and off-beam) were ∼0.2 Hz and ∼0.25 Hz for BNB and NuMI respectively [15]. The cosmic-induced rate from the off-beam Majority stream is estimated to be between 8-11 kHz.

A measurement of the trigger efficiency is extracted from the large statistics of cosmic rays in ICARUS from surface operation. In order to obtain this measurement, the crossing time (T0) of each particle track is needed to unambiguously identify the particles in the event. A T0 time can be extracted from cathode crossing tracks or by matching tracks back to the CRT system. A particle track that crosses the cathode provides the true position of the particle track by matching the two segments in neighboring TPCs. The time the track crosses the cathode is extracted from the spatial shift along the drift direction needed to connect the two track segments. The time resolution from this procedure is on the order of microseconds, with the precision driven by the quality of track reconstruction near the cathode.

Alternatively, a T0 time can be extrapolated from TPC tracks matched with external hits on the CRT system as the CRT hits have a well-defined timestamp on the order of nanoseconds, with the

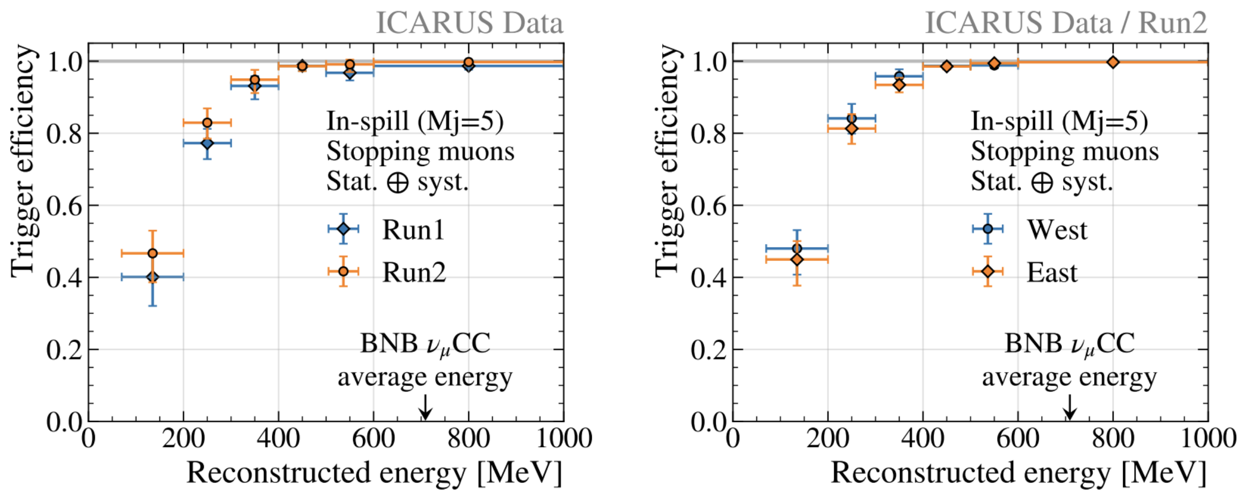

Figure 3.5: Trigger efficiency versus reconstructed energy in Run-1 and Run-2 (left), and separately in the two West and East modules for Run-2 (right). Figure from [15].

CRT time resolution covered in Section 4.5. This method to match the TPC tracks back to the CRT system is referred to as "CRT-TPC Matching" and is covered extensively in T. Boone's thesis [62]. The TPC track trajectory is linearly extended back to the CRT system and matched with the closest CRT hit by looking for CRT hits with the smallest distance (d_{CRT}) to the TPC track projection.

The trigger efficiency was evaluated as a function of energy at different positions in the TPC using both stopping muons and vertical muons. The resulting trigger efficiency as a function of muon energy from residual range is shown in Figure 3.5. Using both Run-1 and Run-2 Majority data, the trigger efficiency saturates around 400 MeV and reaches more than 80% from 200 to 300 MeV [15]. The CRT-TPC matching was further used to evaluate associated systematics, along with the muon track reconstruction from the TPC.

Chapter 4

Cosmic Ray Tagger System

The ICARUS Cosmic Ray tagging (CRT) system surrounds the detector medium ($\sim$ 1,100 m^2) with two layers of fiber embedded in rectangular cross section plastic scintillator to tag high energy particles entering or exiting the TPC. The CRT is made up of three distinct subsystems, Top, Side and Bottom, seen in Figure 4.1 and described below. The full CRT system is introduced in Section 4.1, with more details provided on the Side CRT system as that is the subsystem I primarily worked on. The readout electronics are introduced in Section 4.2 and the installation, commissioning of the subsystem in Section 4.3 and Side CRT noise mitigation efforts in Section 4.4. CRT timing and hit reconstruction is covered in Sections 4.5 and 4.6. Finally, I explain how the nanosecond level precision of the CRT systems are used to tag cosmic backgrounds by matching with PMT signals in Section 4.7.

4.1 CRT Subsystems

The Bottom CRT system[1] is made up of 14 spare veto modules repurposed from the Double Chooz experiment. These modules were installed below the cryostat prior to the detector warm vessel deployment, as seen in Figure 4.3. Each module contains 64 scintillator strips (3.2 m $\times$50 mm $\times$ 10 mm) in two layers with a wavelength shifting (WLS) fiber running the length of the strip. Each strip is read-out at one end with a Hamamatsu H8804 multi-anode photomultiplier tube while the other end of the strip is mirrored [63].

The Top CRT system is composed of 123 modules designed and constructed by CERN/INFN. The CSU group participated in early Top CRT design studies, with more details on the groups contributions in [16]. Each module contains 16 scintillator strips oriented in two layers. Within each module, the scintillator strips are positioned orthogonally to each other in layers (8 strips per

[1] The Bottom CRT system is not yet fully integrated into the CRT Hit reconstruction so it is not used in ICARUS analyses.

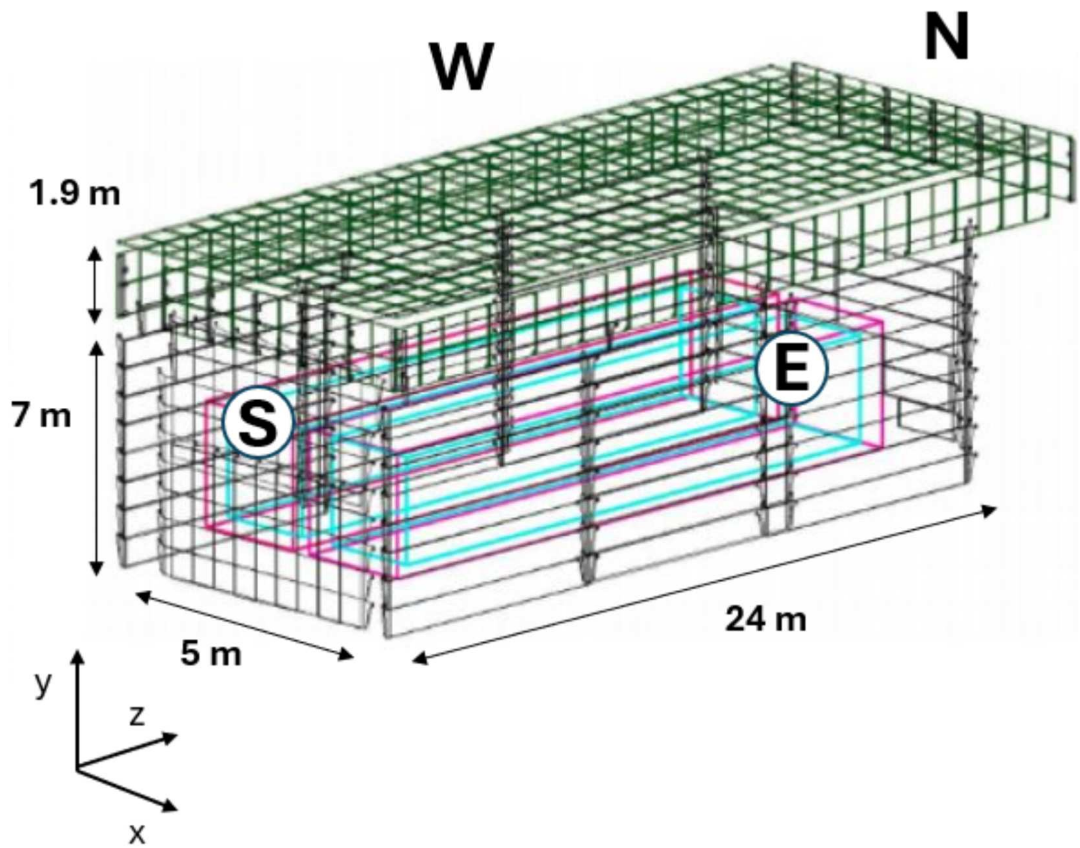

Figure 4.1: Schematic of CRT subsystems surrounding the ICARUS cryostat.

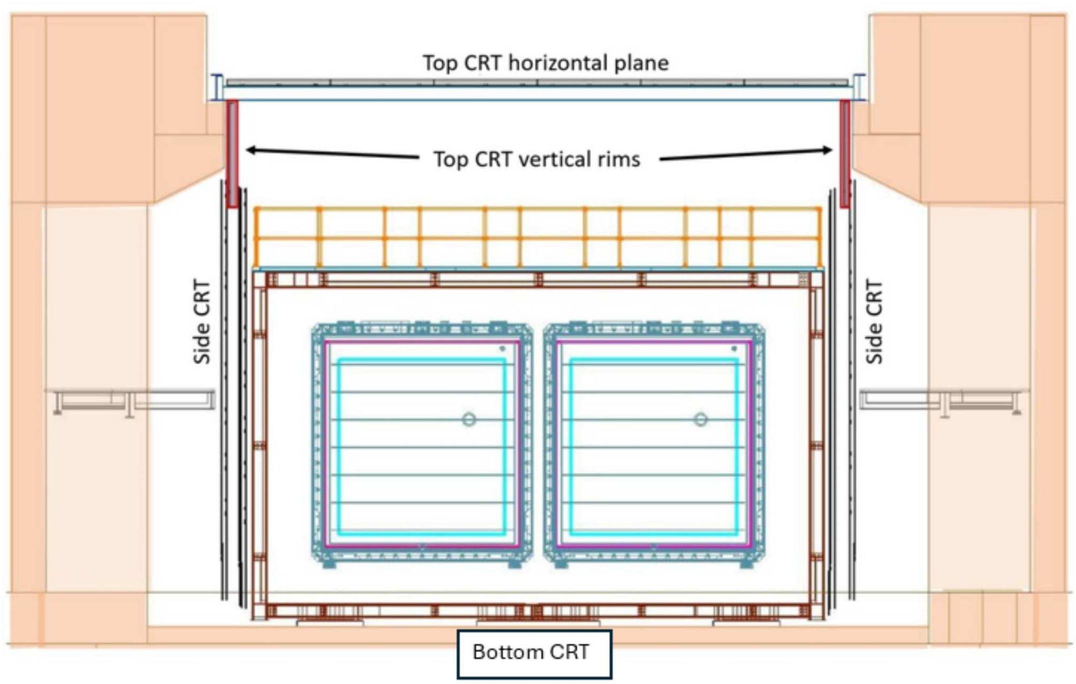

Figure 4.2: Face-on cartoon of the CRT systems surrounding the ICARUS cryostat.

Figure 4.3: Bottom CRT installation below the ICARUS cryostat.

layer, as seen in Figure 4.4) to form an X-Y coincidence by looking for signals in both layers. This optimized design makes each Top CRT module a self contained coincidence unit allowing to localize the position of a CRT interaction with a precision of < 1 cm. Each scintillator strip is 23 cm wide and houses two WLS fibers running the length of the 186 cm length of the strip. The fibers are read out on a single end with a silicon photomultiplier (SiPM) based readout. The full Top CRT system is shaped like a box-top, as seen in Figure 4.1, with 84 modules oriented horizontally (forming the Top-Roof) and 39 modules oriented vertically (forming the Top-Rims). The Top CRT subsystem has 4,000 channels across the 123 modules.

The Side CRT uses repurposed veto modules from the MINOS experiment [64]. Each MINOS module is 8 meters long with 20 individual scintillator strips, with each strip 4 cm wide and 1 cm thick, and a single fiber per strip. These modules are read out on both ends also with a SiPM based readout, with the readout described in more detail below. The Side CRT is made up of eight walls, named after their cardinal direction in the detector hall: North, South, West-North, West-Center (rolling), West-South, East-North, East-Center (rolling), and East-South. The walls have two layers of MINOS modules (inner and outer) operating in coincidence, with all but the South wall installed with a X-X coincidence configuration. The South Side CRT wall is upstream the detector along the BNB beamline and thus will able to intercept a large fraction of rock muons, so the X-Y coincidence was desired here to have optimal position reconstruction. The Side CRT has a total of 2,680 SiPM channels across 217 modules.

4.1.1 Optical Readout for Side CRT

When used for the MINOS experiment, the MINOS modules were readout by PMTs, but a SiPM based readout is preferred due to their robustness and only require tens of volts, compared to the hundreds of volts required to operate PMTs. Working with CSU engineers Dave Warner and Jay Jablonski, Robert Wilson's group at CSU designed and built a new, custom SiPM based optical readout module (ORM). While optimizing the readout design, it was found that the SiPMs did not fully cover the optical fiber which would result in throwing out some of the light. A clever design was needed to cover the full fiber area. Robert Wilson had the idea to tilt the SiPMs slightly, allowing each SiPM to read out two optical fibers, as shown in Figure 4.5a. With the design finalized, the production and testing of the readout modules began. ORMs were produced by then CSU undergraduate engineering students, Krista Grossman, Will Mingus, Jameson Richard, and Will Sheridan, in the CSU High Energy Physics lab with guidance from Warner and Jablonski. The quality control tests of ORMs were performed at CSU by then CSU graduate students Tyler Boone and Chris Hilgenberg, before being brought over to Fermilab. These quality control tests were covered in detail in Tyler Boone's thesis [62].

After arriving at Fermilab, summer 2019 I participated in additional ORM quality control tests before starting my PhD, working with Hilgenberg, Biswaranjan Behera (both CSU), Antoni Aduszkiewicz, Tony Wood and Donnie Munford (University of Houston). A stack of three MINOS modules were set up in the Wideband building at Fermilab as a test stand. The MINOS modules were placed directly on top of each other horizontally (separated with foam spacers) and used as a hodoscope, looking for the coincidence of signals between the different modules. By using two modules (top and bottom) as reference modules, ORMS could be installed and tested on

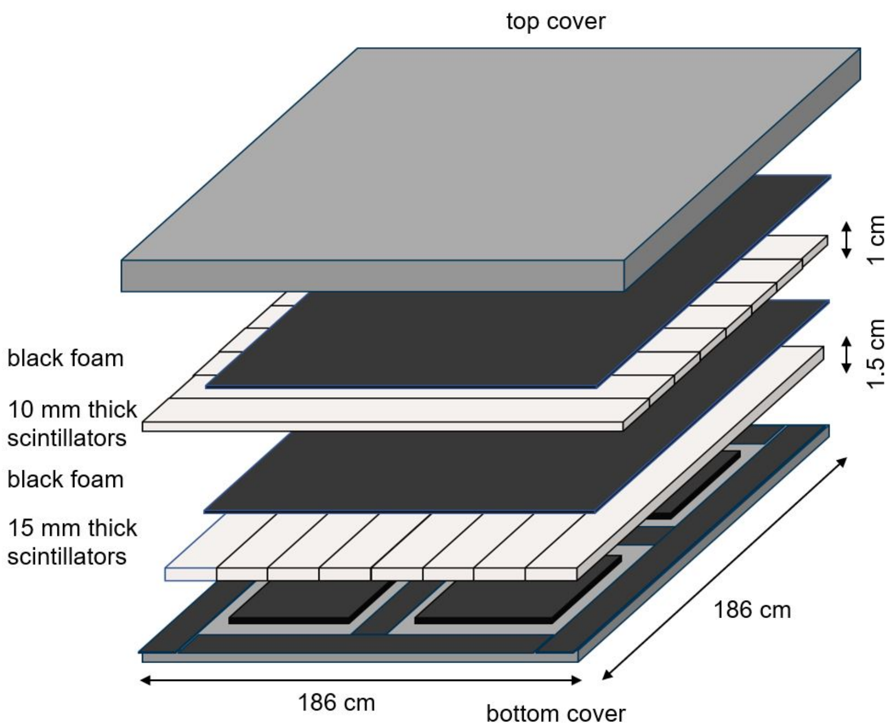

Figure 4.4: Top CRT module design. Figure from the CRT technical note [12].

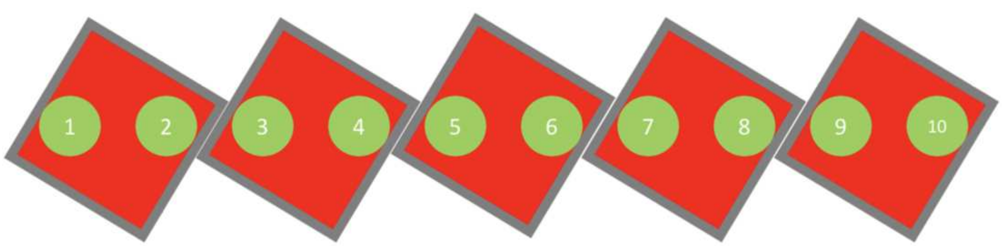

(a) SiPM alignment for each SiPM to read out two fibers. Figure from [16].

(b) SiPM based Optical Readout Modules used for the Side CRTs. Photo from [62].

Figure 4.5: Silicon photomultiplier (SiPM) used for the Side Cosmic Ray Tagging system.

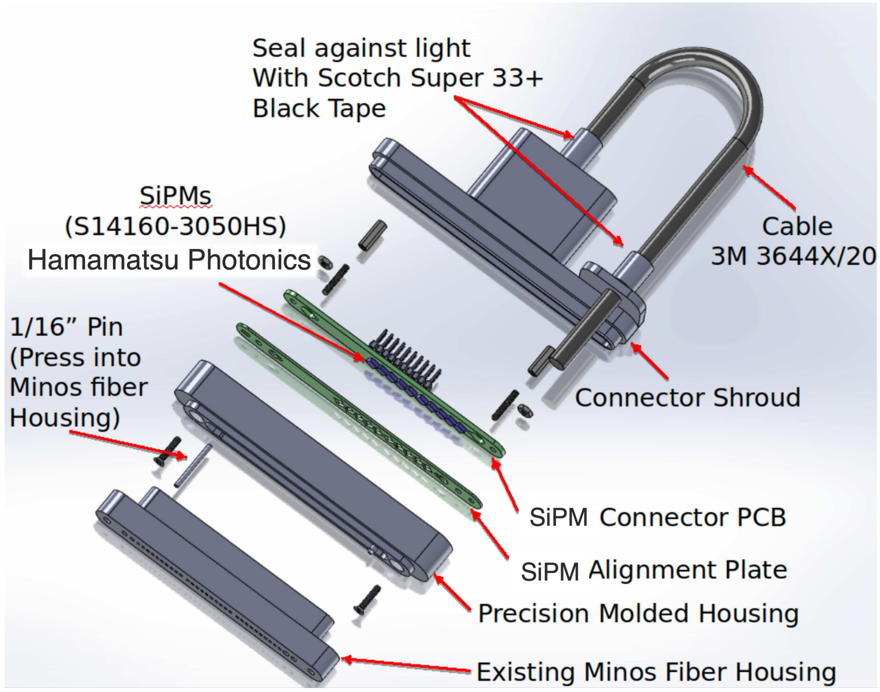

Figure 4.6: Expanded cartoon of the Optical Readout Module design (Image credit: David Warner, CSU).

the center test module. The test setup can be seen in Figure 4.7. 271 ORMs were to be tested for the full Side CRT Installation and I worked that summer to help finalize the ORM test procedure while tests continued throughout the rest of the summer. For each SiPM, the average light yield and gain were measured and stored in a Side CRT Hardware database.

4.2 Front-End Electronics

We use the CAEN A1702/DT5702 32 Channel SiPM Readout Board for Cosmic Rays Veto [65] for the readout and digitization of our SiPM signals, with the same model used by both the Side and Top CRT system. These front end boards (FEBs) shown in Figure 4.8 were designed initially for the SBND CRT Readout at the AEC for Fundamental Physics of the University of Bern and commercialized by CAEN. Figure 4.9 shows the inside of a FEB. Each board requires 5 V of input power. Two Ethernet ports are used for data acquisition and daisy-chaining. The FEBs provide four timing signals: T0 and T1 are independent time reference pulses used for triggering and time-stamping. TIN, a validation pulse input, and TOUT, a trigger output, allow us to daisy chain the

Figure 4.7: A. Aduszkiewicz, A. Wood D. Munford (all Univeristy of Houston) and I behind the Side CRT Optical Readout Module test stand at Wideband in 2019. Picture courtesy of C. Hilgenberg [16].

Figure 4.8: CAEN Model DT5702 used for the Front End electronics for the Side and Top CRT. Photo from FEB Manual [17].

boards together and communicate trigger signals between neighboring boards. Each FEB has 32 SiPM readout channels with a bias and signal pin. The bias pin holds the SiPM at the correct operational voltage and the signal pin digitizes the signal amplitude from the SiPM. The FEB trigger channel is defined as the CRT strip with the largest signal amplitude. We then sample charge in all other channels and average over all SiPM hits acquired. CRT trigger timestamp is based on the time the trigger channel generated the signal. Each FEB has a resolution of 1-2 ns and internal dead-time of approximately 22 μs.

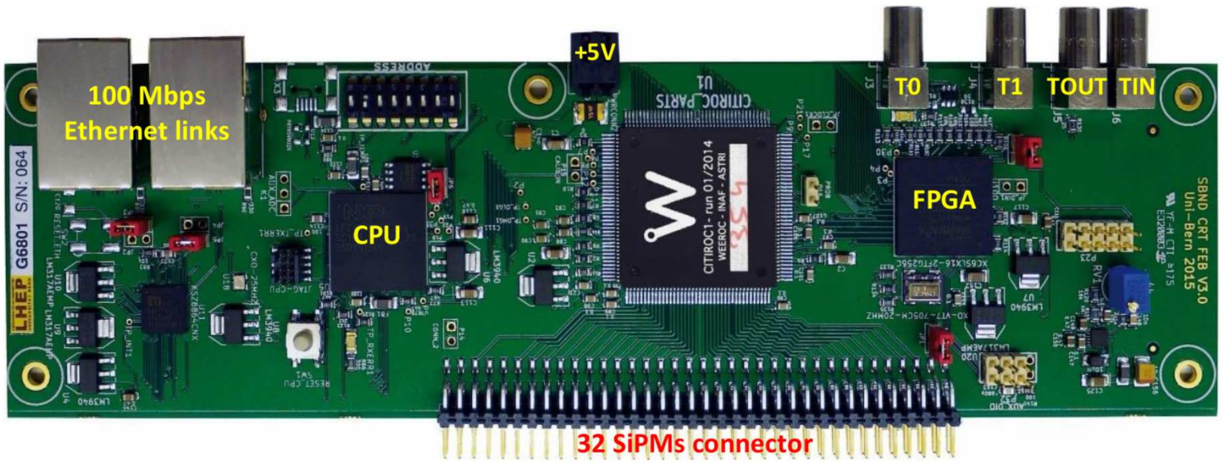

Figure 4.9: Internal view of CAEN Model DT5702 used for the Front End electronics for the Side and Top CRT.

4.3 Installation and Commissioning

The Bottom CRT was installed before the ICARUS warm vessel was placed in the SBN-FD pit. The Side CRT was installed over 2020 and 2021, with the initial commissioning plans interrupted by the COVID-19 pandemic. The North wall was the first Side CRT wall to be installed, and initial shape-only and rate comparisons from this wall were featured in Hilgenberg's thesis [16]. I assisted Hilgenberg with some preliminary data/simulation comparisons from data on the North wall. In August 2020, I received special approval to travel to Fermilab during the pandemic to assist in the commissioning of the East Side CRT wall. Working with Fermilab engineers and technicians, I helped install the MINOS scintillator panels and necessary support hardware. In Figures 4.10 and 4.11, Behera and I can be seen helping the technicians to lower one of the MINOS modules in between Unistrut beams for the East-North CRT wall. After the MINOS modules were installed in position outside the ICARUS cryostat, we mounted the ORMs on the module (see Figure 4.11b), cabled up the electronics and performed light leak checks.

The installation of the Top CRT was completed December 2021 before the installation of the overburden. Data was collected during overburden installation to monitor the impact the overburden has on reducing the cosmic rates in the CRT.

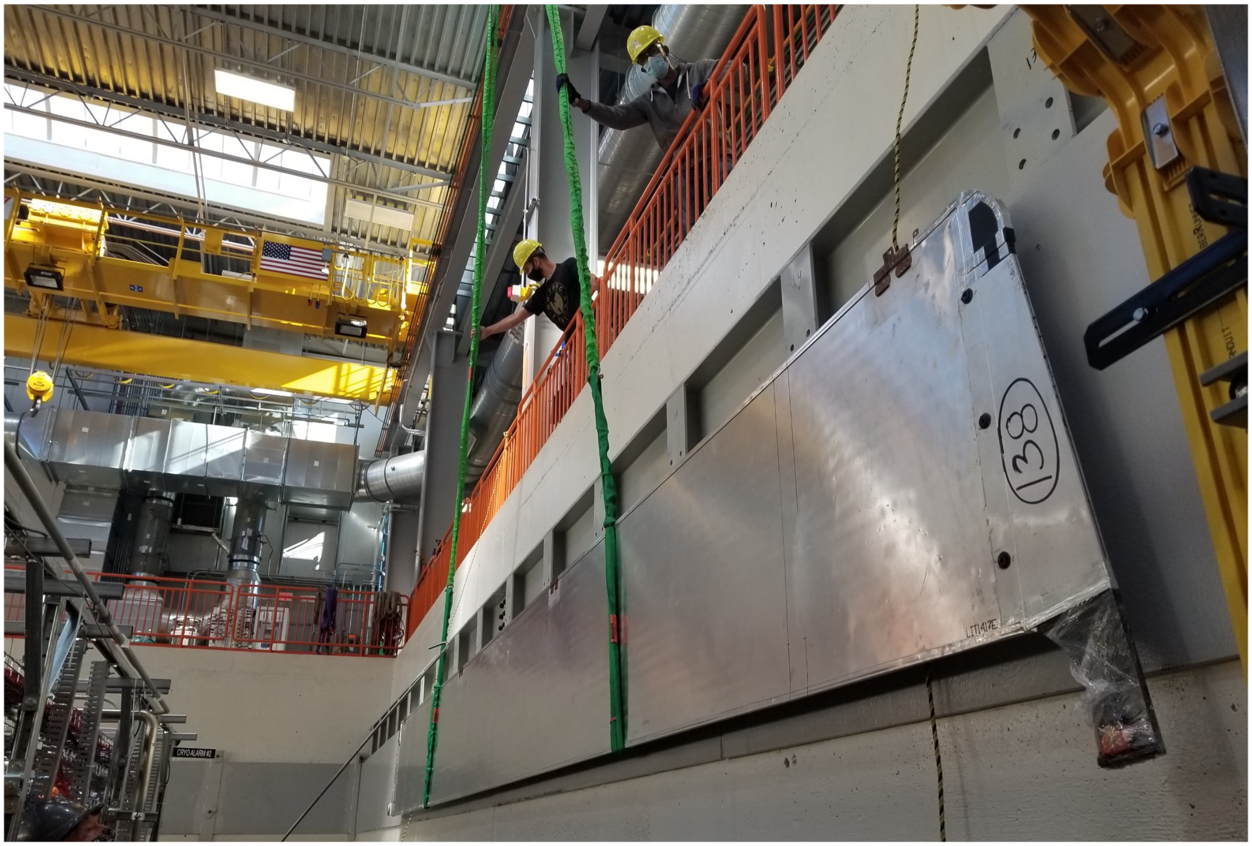

Figure 4.10: A MINOS module being lowered by technicians for the East-North Side CRT wall.

(a) **(b)**

Figure 4.11: Side CRT installation activities. (a) B. Behera and the author lowering a MINOS module between Unistrut beams for the Side East-North CRT wall. (b) The author installing an Optical Readout Module on one of the MINOS modules August 2020.

4.4 Side CRT Noise Mitigation

SiPMs are known to have a high dark noise rate. The FEBs can also have a source of electronic noise. During the tests at Wideband, a significant effect due to electrical noise was observed. This was more troubling in the SBN-FD building as FEBs close to the cryogenic pumps continued to exhibit a high noise rate. After moving out to Fermilab in 2021, I assisted with noise rate studies, working with Logan Rice, then a PhD student at University of Pittsburgh, and Fermilab scientists and engineers (Linda Bagby and Brandon Howe). We worked together to understand and mitigate the noise observed on the Side CRT boards. In Fall 2021, Fermilab hired a new electrical engineer, Matt Micheli, that proposed a design to install chokes on the CRT Power Cables to reduce noise radiating into the boards. We verified that these chokes provided an appreciable reduction in the noise rates.

4.5 CRT Timing

A precise Pulse-Per-Second (PPS) signal is sent from the central trigger rack to the T0 input, which is used to produce an absolute timestamps for every CRT interaction over threshold. The T1 input is the Global Trigger signal communicated from the trigger rack indicating the presence of PMT light within a trigger gate. Using the global trigger at the FEBs provides a beam timing reference within the CRT system. The FEBs digitize the time the Global Trigger signal is received at the T1 input. Offline, we reconstruct the time each FEB receives the Global Trigger signal, referred to as our "CRT Global Trigger signal". This is the global trigger signal we digitize at our CRT FEBs, which is then used as a time reference for each CRT Hit timestamp. The logic of assigning the T0 and T1 timestamps considering cable timing delays is shown in Figure 4.12 from [12]. The delay values shown are for the Top CRT subsystem, but the same logic applies for the Side CRT.

A full calibration of all time delays is essential to achieve nanosecond level timing synchronization with other detector subsystems. Originally, for the Side CRT cable delays we used values derived from the installed cable length with a simple conversion factor of 4.8 ns/m. In August

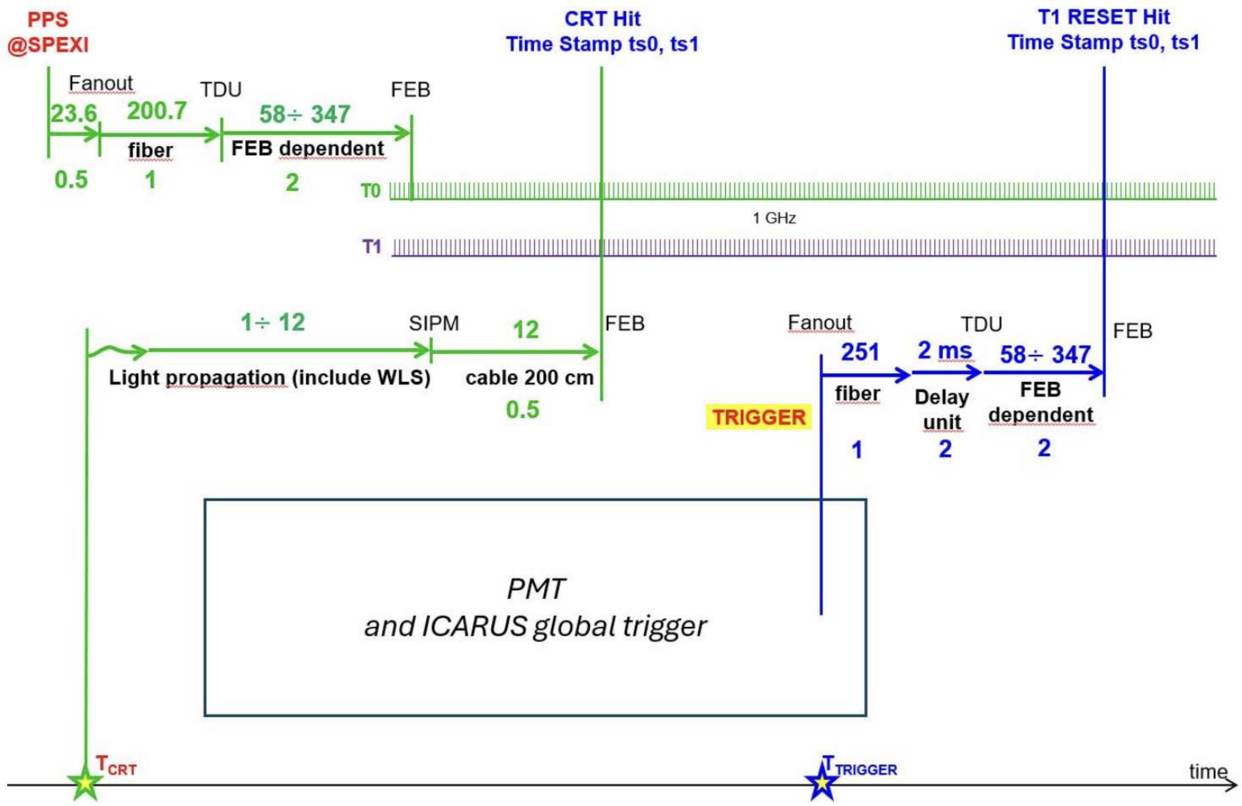

Figure 4.12: Top CRT Timing scheme showing signal propagation time in nanoseconds from [12].

2024, I led a time delay measurement campaign with INFN Bologna student Ricardo Jaimes of all delays along full distribution line to each Side CRT Front-End Board (FEB). With an oscilloscope, we directly measured the true signal propagation delay to each 93 FEB along the T0 and T1 timing lines. Having measured delays as opposed to estimated delays improves our time resolution and determination of the true hit timestamp.

The Side CRT modules time resolution was evaluated using two overlapping CRT walls, the East-Center wall and East-North wall. The East-Center wall was shifted north by 3.35 meters to have an overlap of approximately 2 meters with the East-North wall and data were collected with this configuration. The distribution of the time differences between the hits from the East-Center and East-North walls is shown in Figure 4.13. Comparing the distribution using the measured delay values in red with the estimated delay values in blue, there is a clear decrease in the in the reconstructed time difference. While using the new, measured delay values, we see a fit from the time difference of 5.72 ns compared to 6.38 ns using the old delay values. This represents a clear improvement using the measured delay values compared with the estimated values on the same dataset.

4.6 CRT Hit Reconstruction

Collections of raw FEB data are reconstructed into CRT Hits. Data is collected and saved by the central ICARUS Data Acquisition (DAQ) system, based on the *artdaq* software development toolkit [66] used by a majority of Fermilab experiments. A *BoardReader* application collects Top and Side CRT self-triggers within 10 ms and packages these into data fragments. CRT Hit reconstruction is performed using raw data collected by the FEBs, including timestamps of the T0 and T1 counters and ADC values of all 32 SiPM channels. These raw data first go through a CRT Decoder to decode the raw data fragments into usable data products in LArSoft. The decoder looks for CRT data occurring within 3 milliseconds of the event trigger timestamp. Due to the different designs and configurations fo the two subsystems, the hit reconstruction is handled differently for the Top and Side CRT.

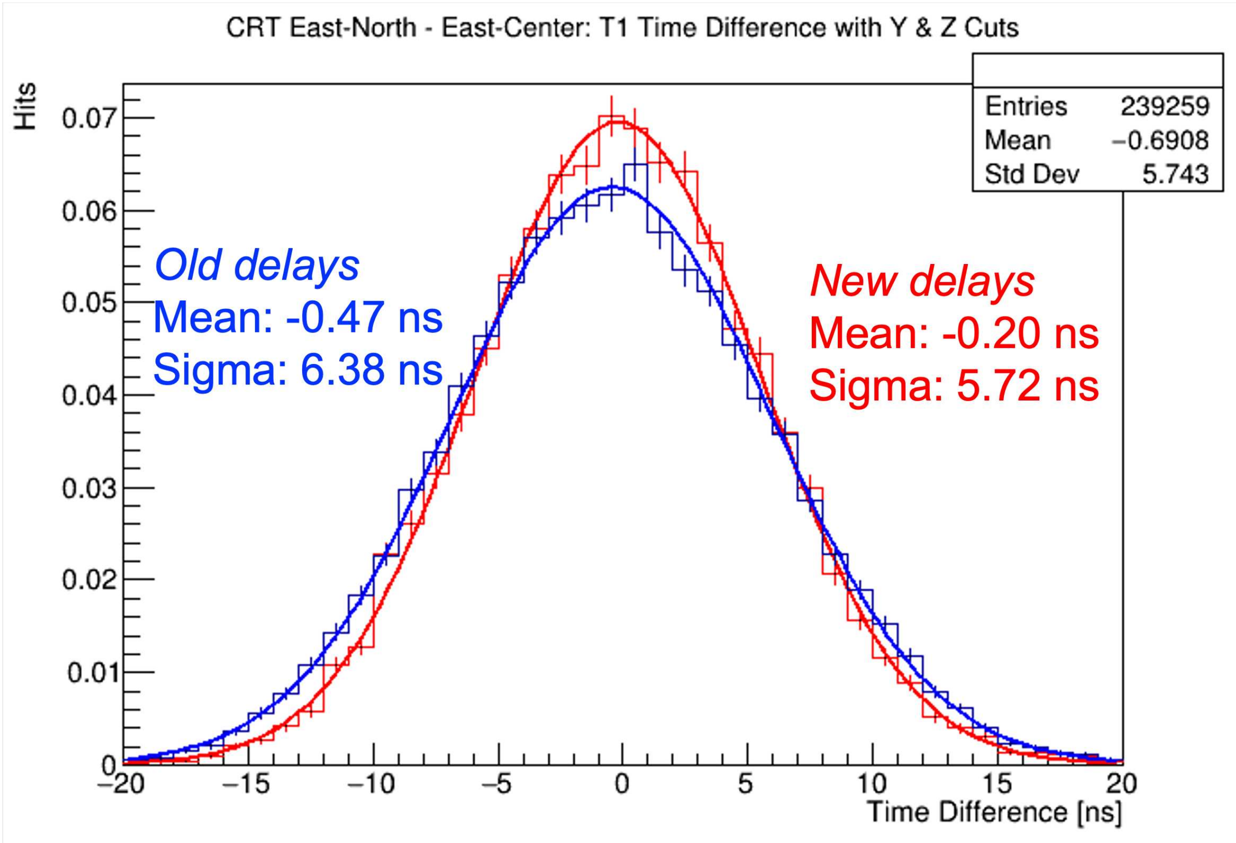

Figure 4.13: Time difference between the hits from East-Center wall and East-North walls, when the East-Center was shifted North to overlap the East-North wall by 3.35 meters, using the estimated delays in blue and the measured delays in red. Figure made using ICARUS data collected July 2023 during the summer shutdown.

The Top CRT modules are self-contained coincidence units designed with the internal triggering logic. Each raw signal from the Top CRT is from the quadruple coincidence of light activity in two perpendicular scintillator strips (four SiPMs reading out two scintillator strips, with two fibers per strip). This makes the hit reconstruction relatively simple.

Side CRT coincidence logic between adjacent layers is done at the software level. The CRT Hits are preselected by filtering out low threshold hits by removing FEB data that have no channel above a set energy deposition threshold of 7.5 photoelectrons (0.53 MeV). The hit reconstruction then looks for FEB channels within the same wall in coincidence with each other by looking for channels within a set time window (150 ns). For the East and West CRT walls, the position of the hit along the module is reconstructed using the time difference between FEB timestamps reading out opposite ends of the same scintillator strip with:

$$z = \frac{T_A - T_B}{2 \cdot v_{prop}} \tag{4.1}$$

where T_A and T_B are the timestamps recorded by FEB-A and FEB-B, and v_{prop} is is the propagation delay along the WLS fiber (0.062 ns/cm), and z is the reconstructed CRT Hit position. The z from inner and outer layers are averaged to assign a final Z position. B. Behera wrote the original Side CRT Hit reconstruction algorithm. Picking up on his work, I developed improvements to this algorithm, which arose due to the complicated coincidence logic of the Side CRT. In some cases, the CRT Hit positions were reconstructed beyond the bounds of the module, which is obviously nonphysical. I discovered this happens when timestamps of the FEB readouts on opposite modules are too far apart in time (for a 8 meter long module, this would be if the two timestamps are over 50 ns from each other). Additionally, in some cases the CRT hit position would be default to the center of the module, and I found this often happens when a module is only readout on a single end. Both of these effects can be seen in Figure 4.14.

I introduced several improvements that corrected the majority of mis-reconstructed CRT Hits. For CRT hits that were reconstructed within the bounds of the module, I studied the distance between the reconstructed hit position and end of scintillator strip (cm) vs. the amplitude of the

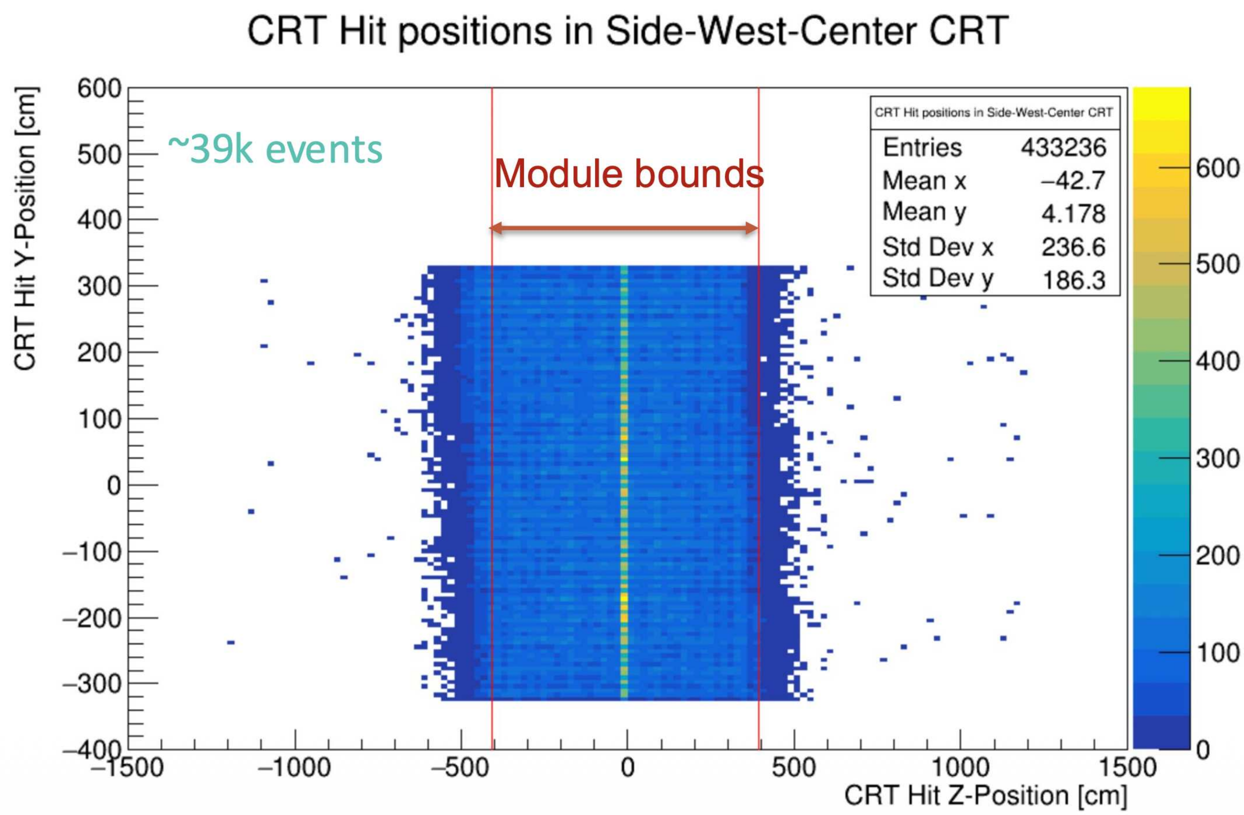

Figure 4.14: Side CRT Hit positions in West-Center CRT. Hits can be seen reconstructed beyond bounds of module and a large stripe is seen in the center, representing hits that were defaulted to the center of the module. Figure made using ICARUS data from Run-1.

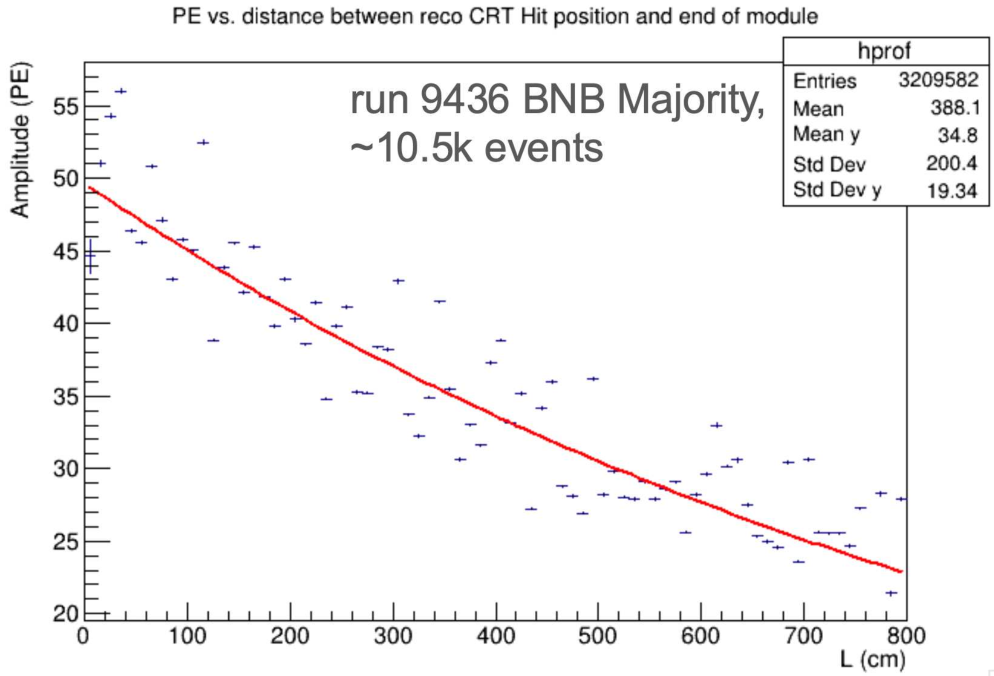

Figure 4.15: Distance between the reconstructed hit position and end of scintillator strip (cm) vs. the amplitude of the readout (in units of photoelectrons) using ICARUS data from Run-1.

readout (in units of photoelectrons). This attenuation curve is shown in Figure 4.15 where we see an attenuation length of $\sim$10 meters for the MINOS modules. We can use this relationship between PE and position to assign a better Z position for hits that only have a single-ended readout. I performed a complete overhaul of the Side CRT reconstruction code, fixing the algorithm to make sure the reconstructed CRT Hits are physical. I used the attenuation curve to reconstruct position of the CRT Hit along the scintillator bars for single ended readouts, and assigned a larger error to the still mis-reconstructed hits so analyzers could easily filter them out. In Figure 4.16, an example of the new West-Center CRT Hit positions using the updated Side CRT reconstruction and removing hits out of bounds is shown. For both the Top and Side CRT, the relative module position are translated into global detector coordinates.

4.7 CRT-PMT Matching

Using the nanosecond-scale synchronization of the CRT and PMT subsystems, we can associate PMT signals to CRT hits to distinguish between tracks entering or exiting the ICARUS detec-

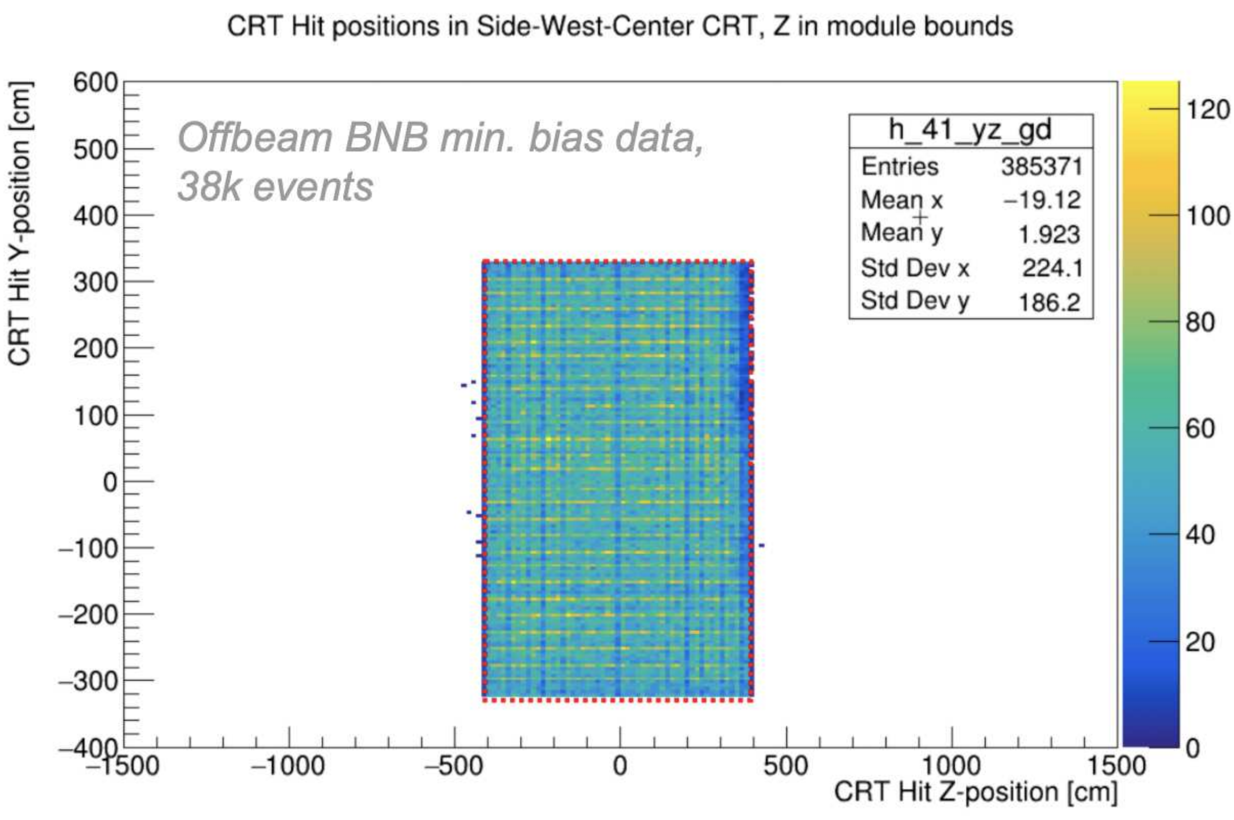

Figure 4.16: West-Center Hit position using updated Side CRT Hit reconstruction code and removing hits out of module bounds. The red box shows the scintillator module boundaries.

tor. Cosmic tracks entering the TPCs will hit CRTs first: $\mathrm{T_{CRT}} - \mathrm{T_{PMT}} < 0$. Neutrino interactions with tracks leaving the TPC will hit the PMTs first: $\mathrm{T_{CRT}} - \mathrm{T_{PMT}} > 0$.

For a cartoon of this working principle, see Figure 4.17. The $\mathrm{T_{CRT}} - \mathrm{T_{PMT}}$ parameter can be seen plotted in Figure 4.18 using ICARUS Run-1 BNB Off-Beam data with approximately 38,000 events. The Top CRT is primarily composed of entering tracks, consistent with negative values of $\mathrm{T_{CRT}} - \mathrm{T_{PMT}}$, as expected since the Top CRT geometry intercepts 80% of the entering cosmics.

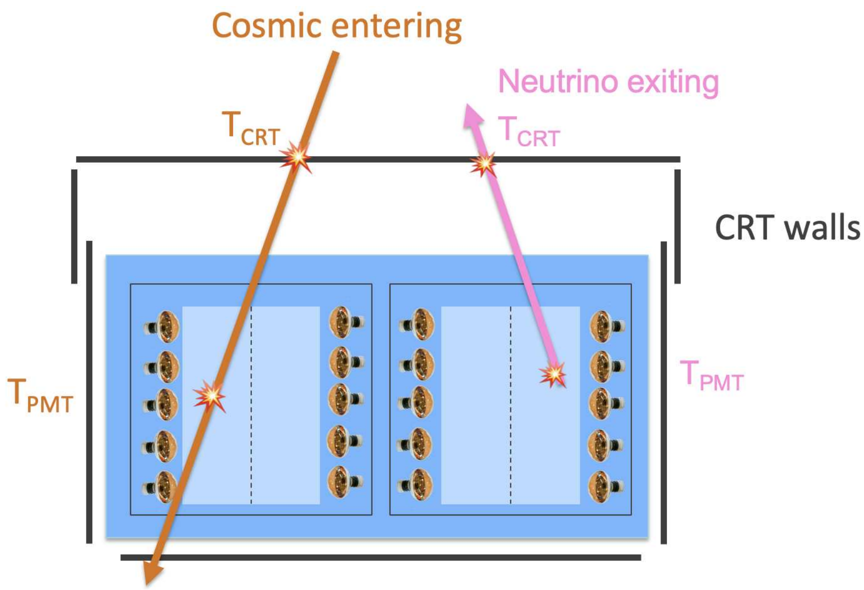

Figure 4.17: Cartoon demonstrating use of CRT-PMT matching.

For the Side CRT, we see both entering and exiting tracks. The Side CRT entering peak location is closer to 0 (representing CRT Hit times closer to the PMT Flash Times) compared to the Top CRT due to the close proximity of the Side CRT walls to the LAr vessel walls. With the Side CRT oriented vertically, we see a second peak representing particles exiting the detector. This was verified by looking at the Y-position of the Side CRT Hit versus $\mathrm{T_{CRT}} - \mathrm{T_{PMT}}$ in Figure 4.19, where we see the entering peak ($\mathrm{T_{CRT}} - \mathrm{T_{PMT}} < 0$) occurring at a higher CRT module Y-position and the exiting peak localized on the lower half of the modules. This agrees with the detector geometry as a cosmic muon could easily enter into the TPC and exit out the Side CRT, but we would expect the exiting tracks to hit lower on the module if it is an outgoing cosmic muon.

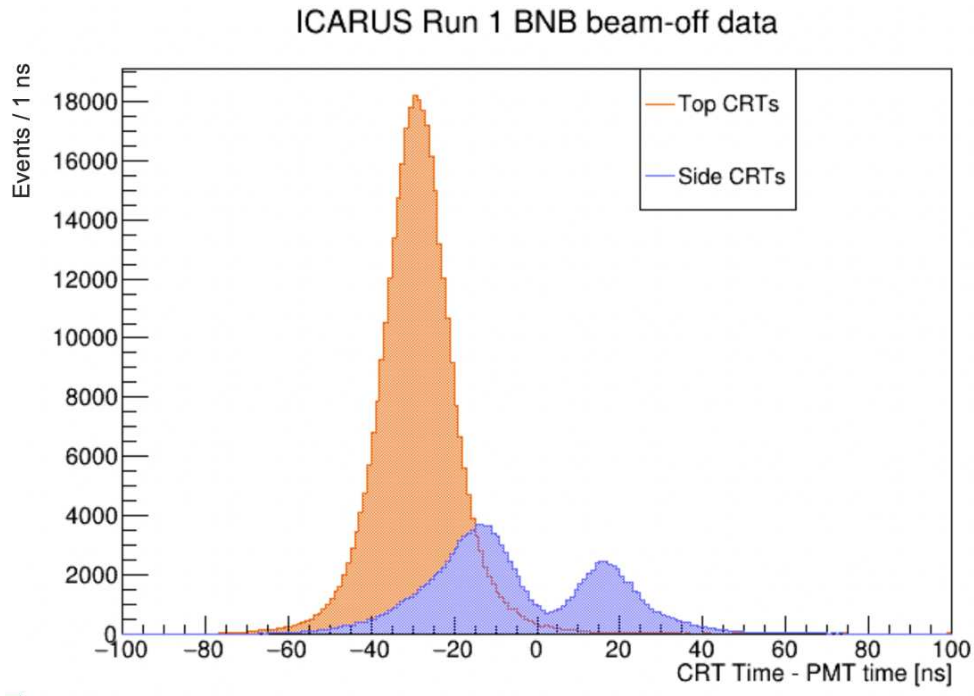

Figure 4.18: CRT Time minus PMT time using ICARUS Run-1 BNB Off-Beam data with approximately 38,000 events. The distribution from the Top CRT is primarily composed of entering tracks, where the Side CRT records tracks entering and exiting.

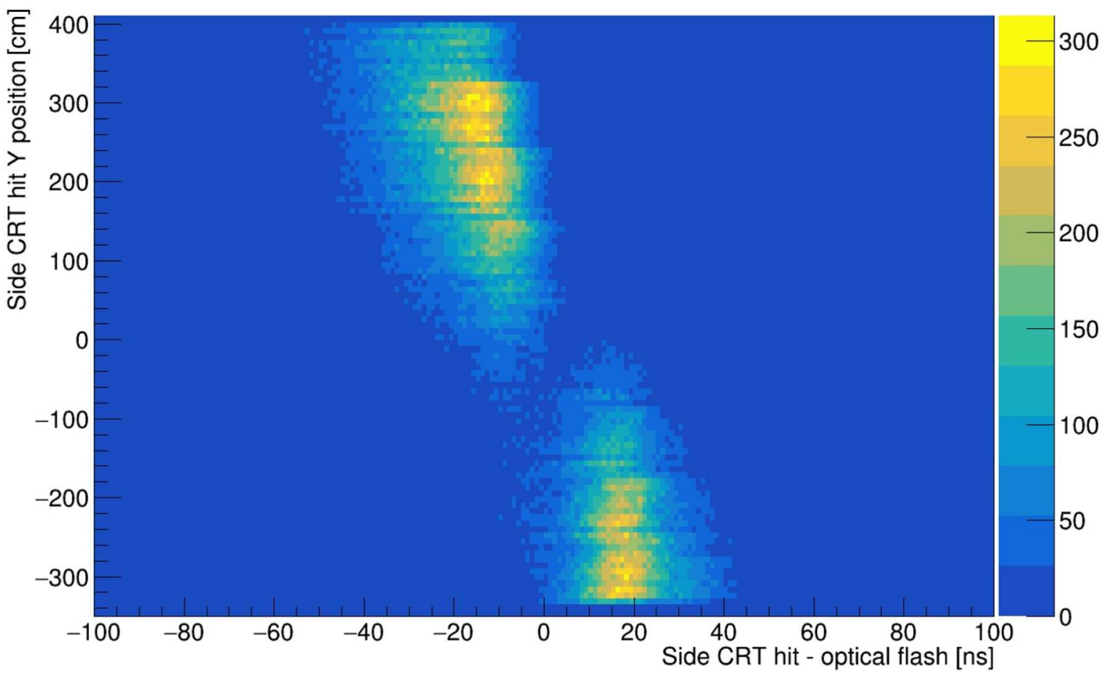

Figure 4.19: Side CRT Hit Y-positions vs. $\mathrm{T_{CRT}} - \mathrm{T_{PMT}}$. Figure made using ICARUS data.

4.7.1 Implementation in Common Analysis Framework

After seeing consistent results from the CRT-PMT Matching, I implemented a CRT-PMT matching tool in *icaruscode*/Common Analysis Files for analyzers to use. SBN experiments use a Common Analysis Framework (CAF) files for a centralized analysis workflow. I integrated the CRT-PMT Matching code into a LArSoft producer module, where the results of the matching were saved in a designated *crtpmt* data product. In the standard offline workflow, the CRT-PMT Matching algorithm is ran during the stage0 processing, which is a high-level decoding stage with CRT and PMT reconstruction ran on raw data files. The output of the CRT-PMT Matching is then saved in the stage0 artROOT [67] files under the *crtpmt* data product module label with type *std::vector<sbn::crt::CRTPMTMatching>*. After stage1 processing, which further runs the TPC processing on the stage0 files, the CRT-PMT Matches are stored in the output calibration ntuple ROOT files under the CRTDataAnalysis **TDirectory** within the **TTree** CRTPMTTree. Finally, the *crtpmt* data product is read into and saved in the CAF files under *rec.crtpmt_matches*.

Based on the number of CRT hits occurring before or after a PMT flash, the CRT-PMT matching results can be used to assign a classification to the flash that was matched. The CRT-PMT Matching Flash Classifications are as follows:

- No CRT Hit matched to an optical flash
- Single Top CRT Hit before optical flash
- Single Side CRT Hit before optical flash
- Top CRT Hit before optical flash and Side CRT hit after
- Single Top CRT Hit after optical flash
- Single Side CRT Hit after optical flash
- Multiple Top CRT Hits before optical flash
- Multiple Top CRT hits before optical flash and more then 1 side CRT hits after the optical flash

- All other cases

CRT-PMT Matching is used to reduce computational needs with a CRT-PMT based filter. In practice, CRT-PMT Matching can be used to skip computationally heavy TPC data reconstruction for cosmics by vetoing events that were triggered by a cosmic entering from Top CRT.

4.7.2 CRT-PMT in Event Selections

The CRT-PMT Matching can be used to select fully-contained or not fully-contained interactions. For fully-contained, the CRT-PMT matching suppresses the cosmic background arriving in time with the beam. Alternatively, the CRT-PMT Matching can be used to study interactions not fully contained within the detector volume by looking for exiting muon tracks.

CRT-PMT matching is used to further reject backgrounds in ICARUS' BNB 1μNp event selection analysis by selecting events that have no flashes in the beam spill time matched to a CRT Hit, resulting in a 98% selection efficiency from the CRT-PMT cut alone.

Chapter 5

Data-driven background modeling

Understanding detector effects and quantifying the associated systematics uncertainties can be challenging. ICARUS' initial analyses relied fully on Monte Carlo (MC) detector simulations to study and assign the associated systematics. Using a method developed by MicroBooNE [68] and NoVA [69], we are moving to overlay simulated neutrino events on real cosmic data collected by the ICARUS detector. This allows us to use real detector data to model our backgrounds and evaluate detector systematics. This requires complete calibration of TPC, PMT and CRT subsystems to data.

In this chapter, I will summarize the ICARUS Monte Carlo detector simulation in Section 5.1 and discuss some shortcomings that motivated the development of a technique that overlays data from the detector over simulations of neutrino interactions. I will then focus on the overlay technique and evaluate the current status of this effort in ICARUS in Section 5.2.

5.1 Monte Carlo Simulation

We use Monte Carlo methods to simulate both cosmic and neutrino events in ICARUS. Cosmics are modeled using CORSIKA, as introduced in Section 2.2 and explained in Section 5.1.1. The neutrino events are simulated using GENIE [70], a neutrino generator widely used in the experimental neutrino physics community and the generator of choice for the SBN program. To propagate simulated events (from CORSIKA or GENIE) through the detector materials, we use the GEANT4 [71] toolkit. This toolkit allows us to define our specific detector geometry and track these simulated particles through our detector setup.

5.1.1 Simulating Cosmogenic Backgrounds

The cosmic flux is modeled using CORSIKA (COsmic Ray SImulations for KAscade), a Monte Carlo simulation package of air showers from high energy cosmic rays [72]. CORSIKA is implemented directly in the LArSoft framework [73], and was adopted as the cosmic ray simulation for detectors in the SBN program, as opposed to FLUKA used in the original SBN Proposal [5]. CORSIKA has two models for the description of primary particles hitting Earth's upper atmosphere. The Constant Mass Composition Model includes simulation of both light and heavy elements, while the proton-only model includes only primary photons. For MicroBooNE, the proton-only model was adequate to simulate the cosmic ray fluxes [74], so following some brief studies this model was also adopted for ICARUS. CORSIKA simulates a data library of cosmic particles ("primaries") distributed uniformly on top of the ICARUS cryostats, and looks for particles with greater than 50 MeV of kinetic energy that cross through a "buffer box" surrounding the detector. These particles are then propagated through the detector geometry with Geant4 [71].

I worked on validating the cosmic flux produced by CORSIKA to ensure it gave similar results to the FLUKA simulation. CORSIKA with the proton-only model predicts a total cosmic muon flux of $130\ \mathrm{Hz/m^2}$, for $\mu^{\pm}$ above 50 MeV. See Figure 5.1 for the flux vs. kinetic energy of various simulated particles at ICARUS over the total estimated integrated beam-on time of 211 seconds. Assuming $\sim 6.6 \times 10^{20}$ POT exposure with 5×10^{12} protons / spill, this would produce a total of 1.32×10^{8} beam spills. For a 1.6 μs long BNB spill, this results in 211 seconds of total integrated beam-on time. This initial validation was done as we started doing studies on the impact of a concrete overburden on reducing the cosmic ray flux, as discussed in Section 2.2.

As the name suggests, CORSIKA was originally designed for the KAscade experiment, studying cosmic rays in the energy range 10^{16} - 10^{16} eV and as such has known deficiencies modeling low energy cosmic related activity (see sharp cut off at low energies in Figure 5.1).

5.1.2 Simulating TPC Noise

Understanding noise within the TPC is important for spatial resolution and calorimetric reconstruction. A data-driven calibration and simulation is used for the ionization charge signal and electronics noise from the TPC [18]. ICARUS has worked in great detail to categorize (coherent vs. intrinsic) noise within the detector, where the intrinsic noise is the noise that is inherent on a

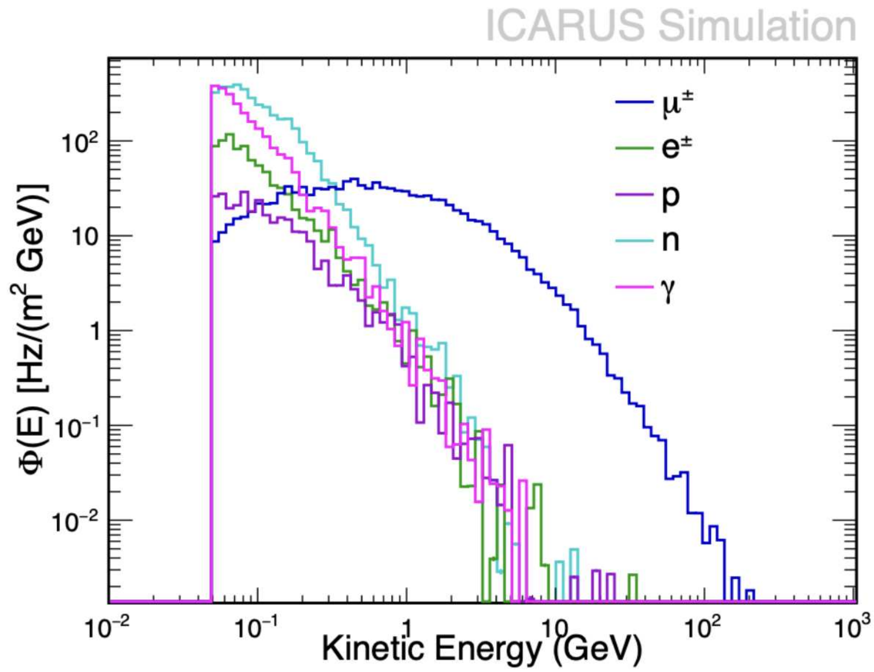

Figure 5.1: Flux of cosmic particles at surface from CORSIKA over a 211 s exposure (corresponding to $\sim 6.6 \times 10^{20}$ POT).

single TPC wire and the coherent noise is that which is shared between wires on the same TPC readout board. The coherent noise present across channels on the same readout board can be subtracted off to reduce the overall noise. Figure 5.2 shows the measured noise levels before and after coherent noise filtering with the cathode high voltage set to 0 V. After removing the coherent noise, the TPC noise model has the ability to model event-to-event variations very well (see Figure 5.3a) where we see the distributions from data closely matching MC. Despite this, the noise model has some limitations modeling channel-to-channel spatial variations, as shown in Figure 5.3b.

5.2 Overlay Technique

The overlay technique, where we overlay simulated neutrino events on off-beam data, has many benefits. With a data-driven modeling of backgrounds, this removes the need to rely on Monte Carlo cosmic generators to model our cosmic backgrounds. CORSIKA, FLUKA or other cosmic ray generators may have different composition or flux compared to reality. As discussed above, CORSIKA has known limitations specifically with low energy cosmic activity, which is

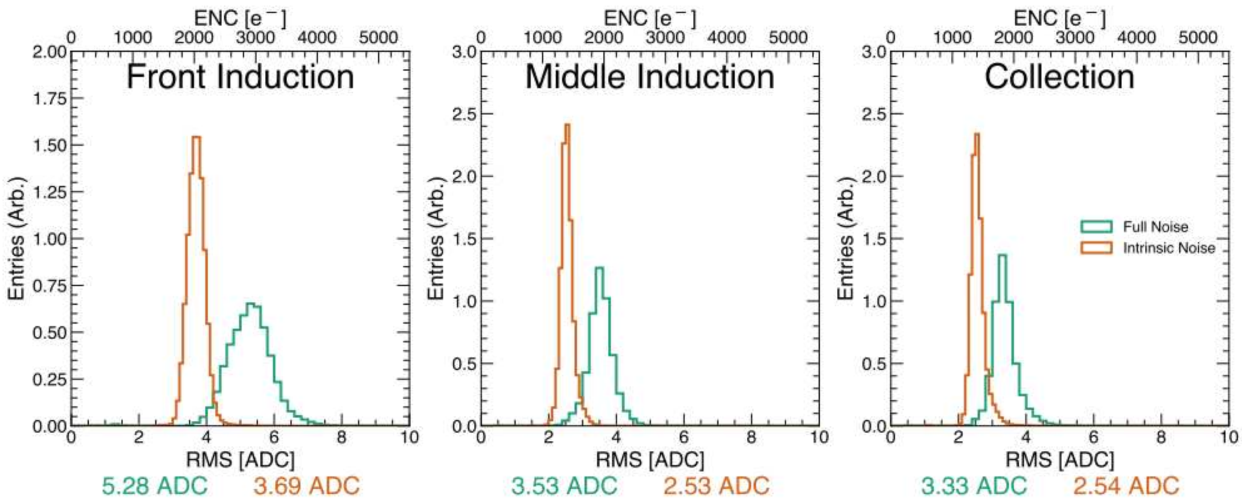

Figure 5.2: TPC noise distributions per wire plane of each waveform before and after coherent noise removal. Figure from [18].

important to model well for a sensitive oscillation search. In addition to cosmic backgrounds, radiological or other sources of backgrounds that aren't modeled are provided for free using off-beam ICARUS data. Using data driven cosmic overlays also has a reduced dependence on the detector noise simulation. An additional benefit is using fewer computing resources, as using cosmic data collected by the detector results in less time spent simulating cosmic backgrounds. See Figure 5.4 for an example of an overlay event with a ICARUS off-beam data event with a simulated neutrino interaction.

TPC waveforms from Off-Beam ICARUS data are overlaid with the TPC signals from a simulated neutrino. In practice, this is done by merging the raw waveforms from both simulation and data directly. In Figure 5.5, we see that the raw TPC signals are correctly being merged from data and simulation.

Collections of raw CRT hits from data and simulation are merged directly. Figure 5.6 shows CRT Hit positions from a single off-beam cosmic data event (6 millisecond exposure), where green star marks the interaction vertex of a 500 MeV neutrino and the red star marks the additional CRT Hit we get from the simulated neutrino. I focused on calibrating the CRT timing for overlays, ensuring the two collections are on the same time scale.

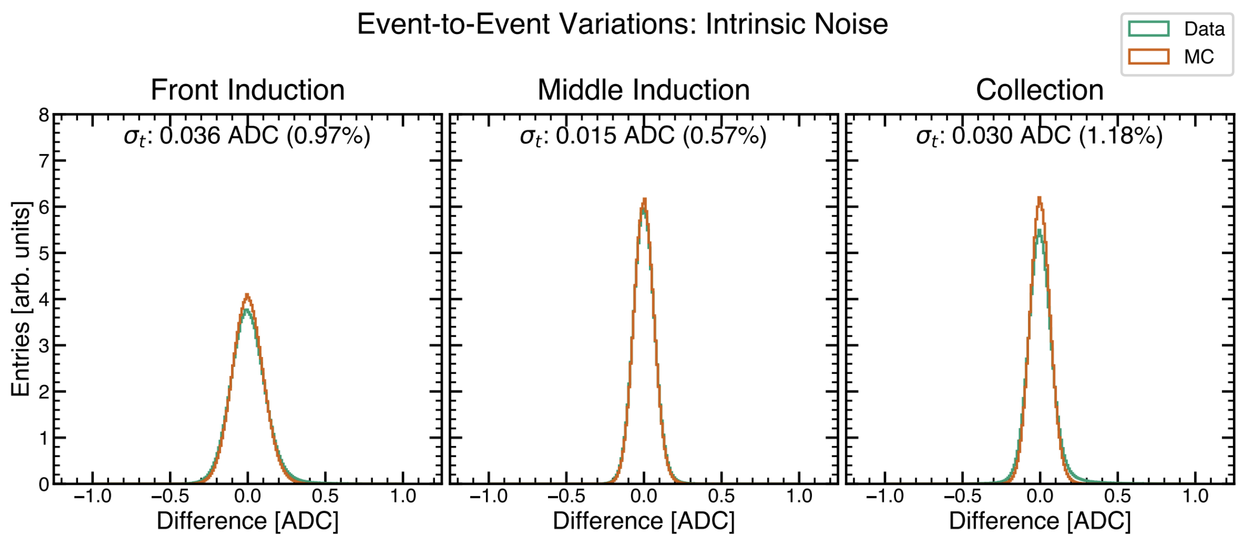

(a) Event-to-event noise variations.

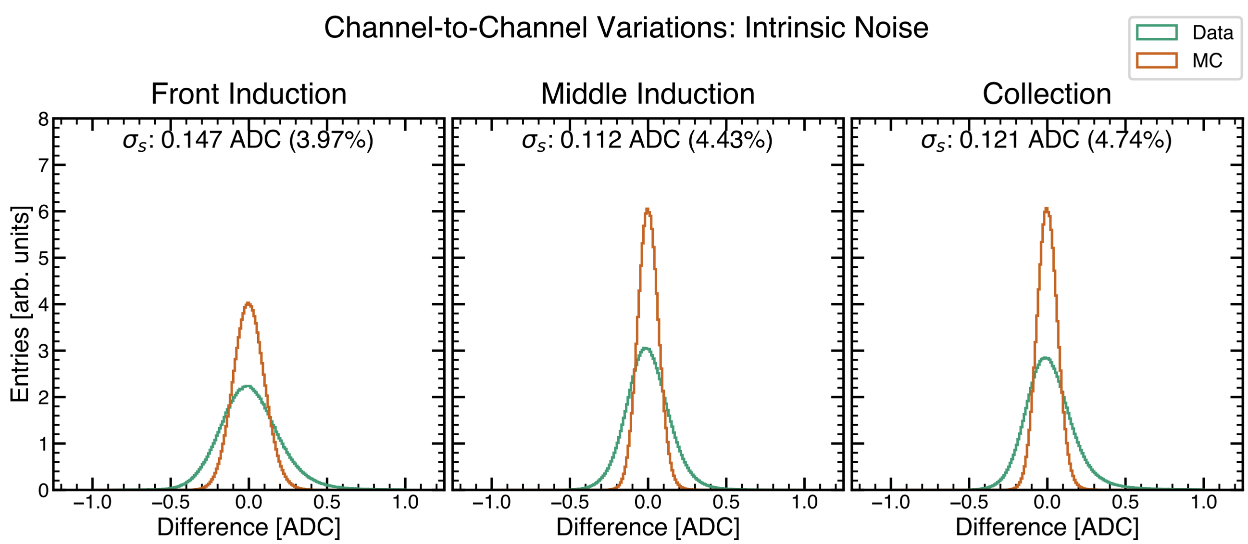

(b) Channel-to-channel noise variations.

Figure 5.3: TPC noise variations in data and Monte Carlo after coherent noise filtering. (a) Event-to-event variations are calculated by event using the difference between the measured RMS and the median RMS for a specific channel, while (b) channel-to-channel noise variations are calculated both by event and by channel using the difference of the measured RMS from the median RMS of the entire group of sixty four channels on a single TPC readout board. Figure from [18].

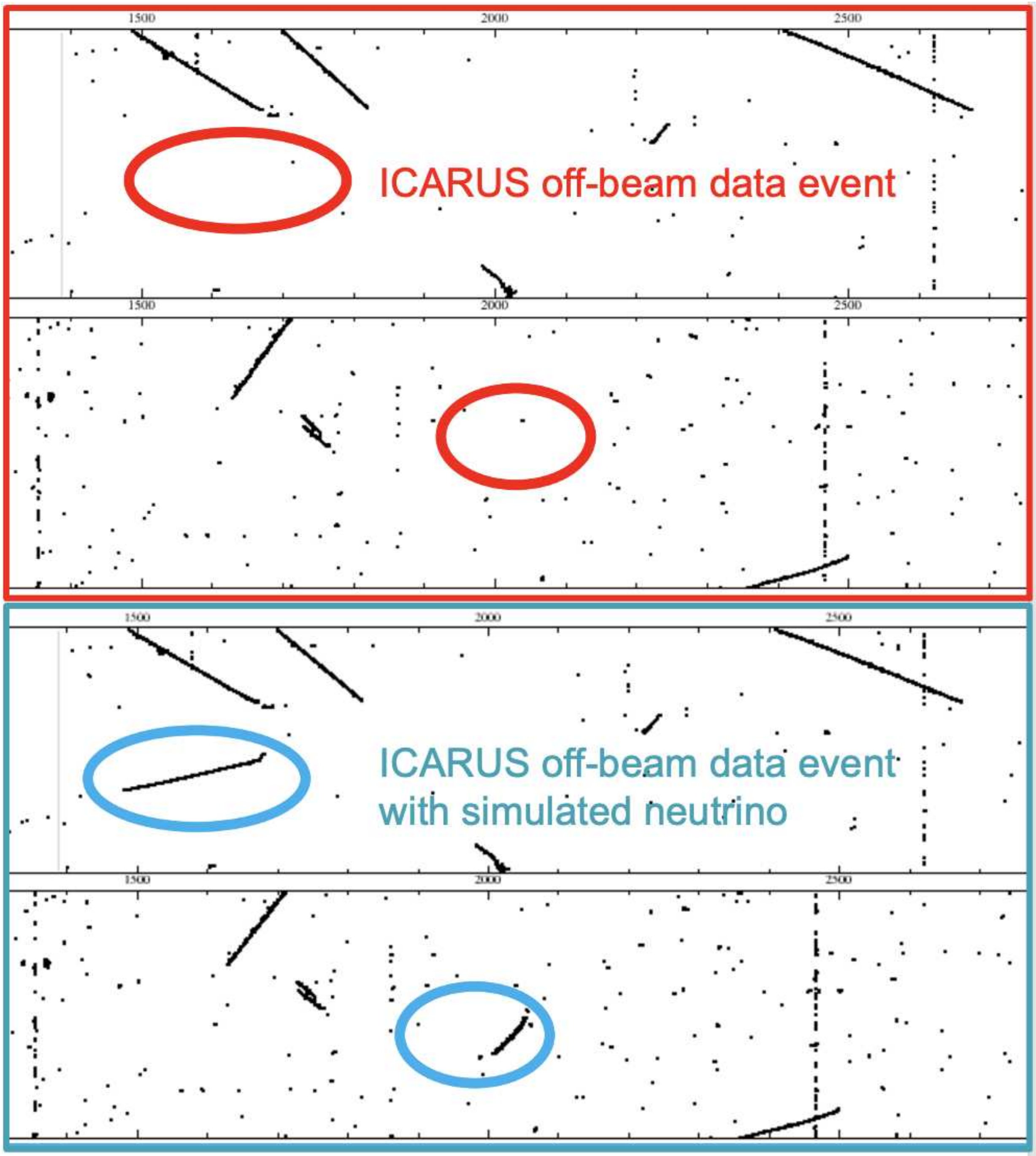

Figure 5.4: ICARUS off-beam data event (top) overlaid with as simulated neutrino interaction (bottom). The blue circles in the bottom figure show where the simulated neutrino event is reconstructed in the event display, while the circles in red indicate the same position with no off-beam data tracks reconstructed before overlaying.

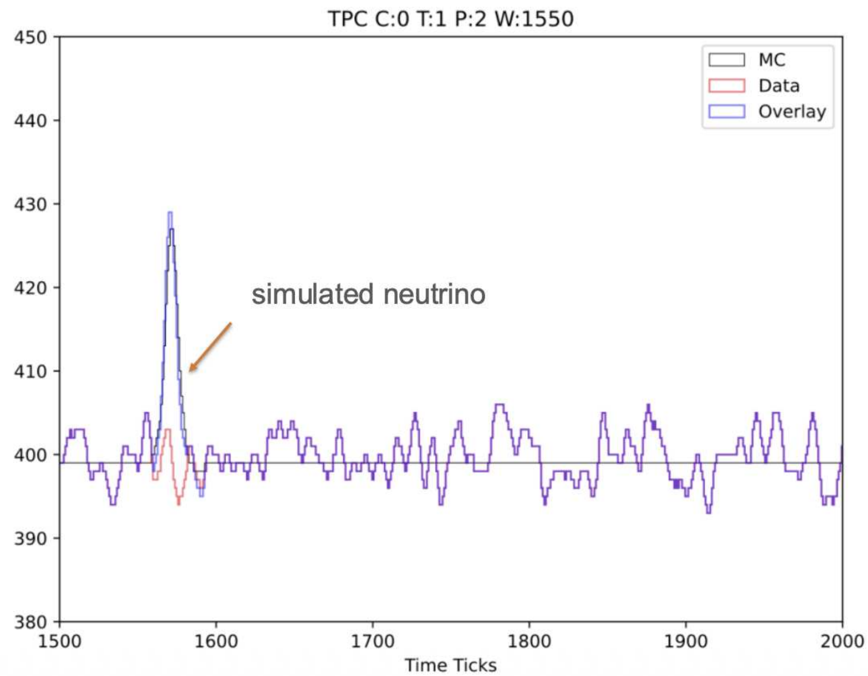

Figure 5.5: Raw waveform from a single TPC wire in off-beam data overlaid with simulated neutrino.

Similar to how the TPC signals are overlaid, the raw PMT signals from data and simulation are added directly. Careful handling is needed with the PMT system as this system is used as the detector trigger, and we want to make sure were triggering on the interaction that happened first. During the initial validations, it was found that the simulated noise was not turned off for the Monte Carlo waveforms, as can be seen in Figure 5.7a. PMT waveforms from a simulated MC neutrino interaction are overlaid on off-beam data PMT waveforms, and the two waveforms are summed to give the overlay waveform (top curve). It is a simple fix to turn off the simulated noise in the MC simulation, which is shown in Figure 5.7b. As can be seen in both figures, there is a shift in the sample time between the MC and data waveforms, where the MC waveform extends longer than the data readout time (circled in red). To fix this, a relative time shift is needed between data and MC events. This work was investigated and addressed by CSU student Noah Vardy, BNL postdoctoral researcher Matteo Vicenzi and SLAC staff scientist Gianluca Petrillo, where the timing in the simulation was shifted to the trigger time.

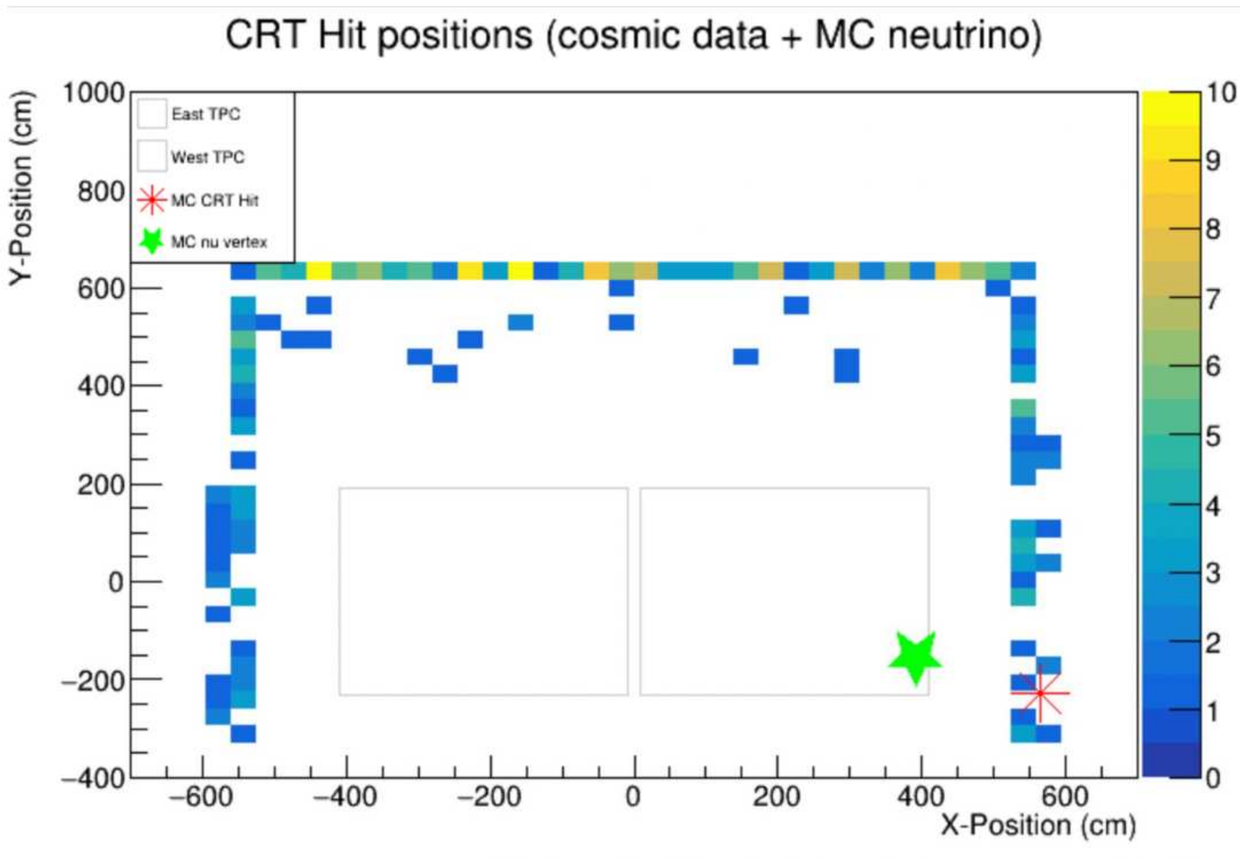

Figure 5.6: CRT Hit positions from a single off-beam cosmic data event (6 ms). The green star marks the interaction vertex of a 500 MeV simulated neutrino and the red star marks the additional CRT Hit we get from the Monte Carlo (MC) neutrino.

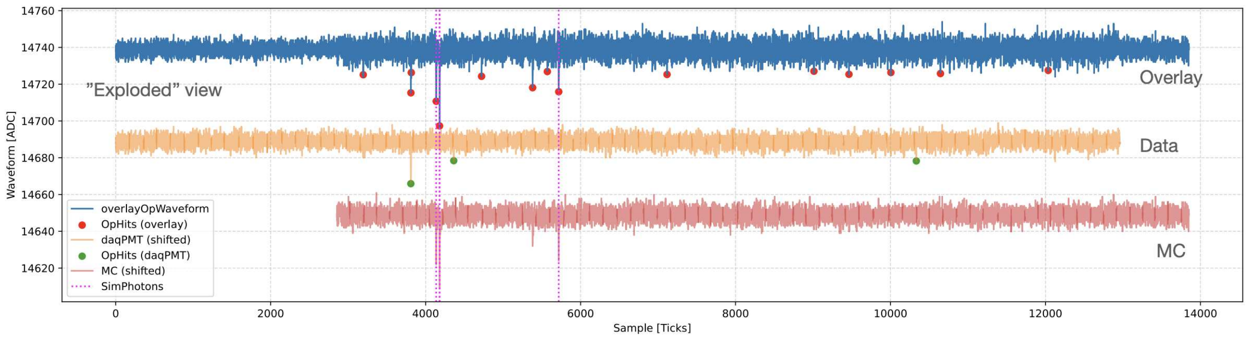

(a) MC waveform with simulated noise turned on.

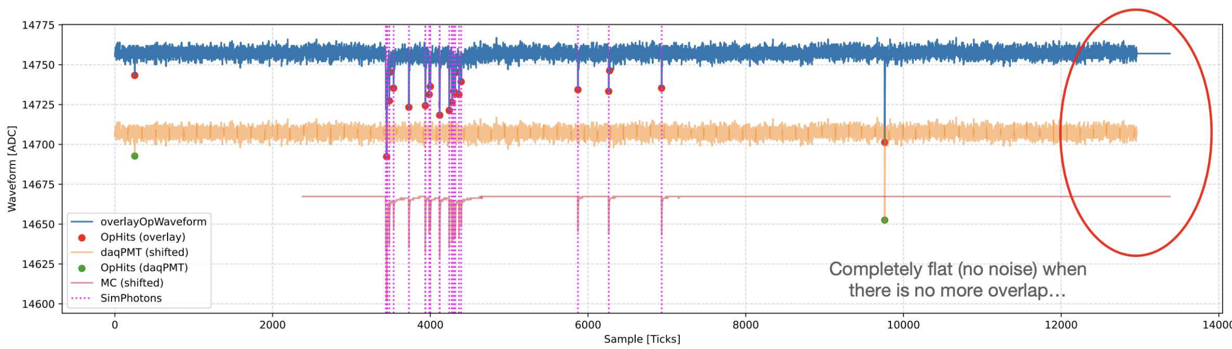

(b) MC waveform without simulated noise.

Figure 5.7: Data and MC PMT waveforms are summed to give an overlaid PMT waveform. (a) MC waveform with the simulated noise left on and (b) shows the waveform with the simulated noise turned off. The red circle shows a timing shift between data and MC events.

Chapter 6

Nanosecond-level Timing Reconstruction

Precise timing is a powerful tool in particle physics, where we are dealing with relativistic particles traveling close to the speed of light. Our ability to resolve the fine timing structure down to the sub-nanosecond level has improved greatly as detector technology improves, and can significantly expand our physics reach in studying neutrino interactions and searching for Beyond Standard Model (BSM) physics.

In this chapter, I will go over methods to resolve the substructure within the neutrino beam using the ICARUS detector. I will review the accelerator technology used to generate the beams of neutrinos (Section 6.1), accelerator signals used at ICARUS in Section 6.2, and the ingredients we use to resolve this substructure within the ICARUS detector in Section 6.3. In Section 6.4 I show the reconstructed bunch width across ICARUS runs. I highlight some features observed which led to discussions with the Fermilab Accelerator Division in Section 6.4 and discuss a recent narrow bunch beam test run in Section 6.4.3. I then discuss how this precise timing information can be leveraged to remove backgrounds for neutrino event selection in Section 6.5. Finally, in Section 6.5.3 I present a novel technique using the bunch structure to select events in our Minimum Bias data stream.

6.1 Accelerating RF cavities

An overview of the neutrino beams used by the SBN program was described in Section 1.2.2. The Fermilab accelerator produces beams of neutrinos by accelerating protons to nearly the speed of light (99.6% c) and collides them with a fixed target, producing mostly charged pions that are focused with a magnetic horn. The pions then readily decay into muons and muon neutrinos. The protons are sent in *spills* which have substructure due to the accelerating radio frequency (RF) power source used to accelerate them. See Figure 6.1 for the basic operating principle of a RF source. Within the RF cavities, protons are accelerated with an oscillating electric field, while

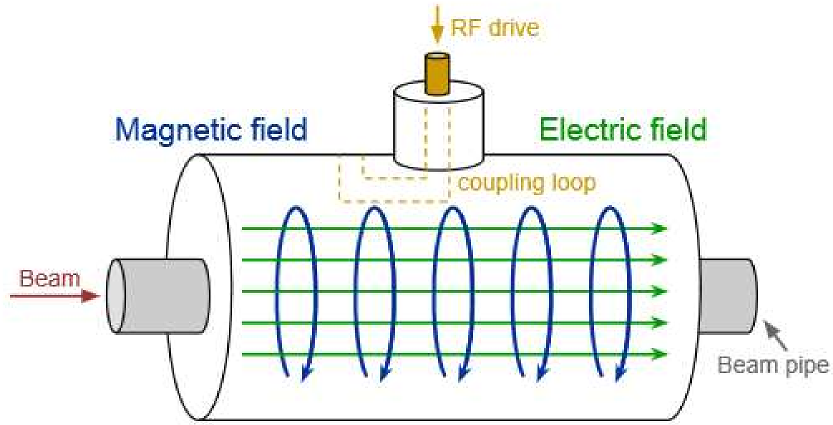

Figure 6.1: Basic operating principle of a Radio Frequency (RF) source used to accelerate particles from [19].

the field reverses direction with the RF cycle (see Figure 6.2b). As protons pass through the superconducting RF cavity (Figure 6.2a), the field gives them a momentum kick gaining energy and speed. The protons are accelerated or decelerated (gaining or losing energy) depending on the RF phase. As the field is oscillating, the protons must arrive at a precise time within the cavity so they gain momentum when they need it: slower particles receive a larger kick and faster particles receive less of a kick, leading to particle bunches. The bunching of the proton beam is inherent in the RF accelerating cavity design which allows us to accelerate the protons to close to the speed of light.

When the NuMI beam is operating, the Booster beam is "bunch rotated" to match into the Fermilab Recycler/Main Injector for a process called "slip stacking". Slip stacking is a beam accumulation technique used at Fermilab by merging (or stacking) two beams to nearly double the intensity of the beam, which is what establishes the high intensity beam to NuMI. A particle beam is described with both transverse (x,y) and longitudinal (z) components in phase space, where the transverse phase space describes the cross-section and angular divergence of the beam and longitudinal phase space describes the position along the beam direction including the bunch length and energy spread. Bunch rotation is a process used to modify a particle bunch in longitudinal phase space, trading off momentum spread (ΔE) for time spread (ΔT) [60]. The beam spreads

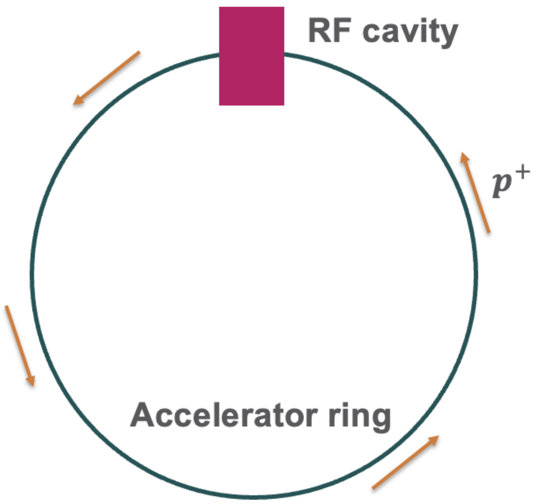

(a) Cartoon of a RF Cavity in a particle accelerator ring.

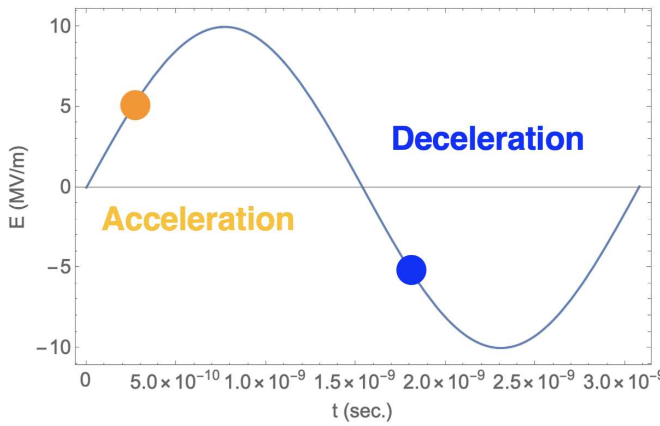

(b) Oscillating electric field in a RF Cavity.

Figure 6.2: Acceleration in a RF cavity. **(a)** depicts the RF cavities within the accelerator ring, where the RF frequency is dependent on the particle revolution frequency around the ring and a set harmonic number that determines the number of RF buckets in the ring. For BNB, the harmonic number is 84 with 81 filled buckets. The circumference of the BNB ring is 474 m, where the protons take roughly 1.6 µs to travel around the Booster. Cartoon not to scale. **(b)** is taken from [20]. The oscillating electric field accelerates or decelerates particles depending on the RF phase.

out in momentum space as it passes through magnets situated along the length of the accelerator ring and bunch rotation is a method used to decrease the momentum spread, allowing the beam to pass through cleanly. The beam is bunch rotated by rapidly decreasing, for just a quarter of the synchrotron period, and increasing the RF voltage [75]. The RF voltage is adjusted to allow the particles to rotate in phase space, effectively exchanging the momentum spread for a reduced time spread.

6.2 Beam Signals

The Fermilab Accelerator Division (AD) transmits signals from the beam target locations in advance of protons hitting target, indicating neutrinos are about to arrive at the detector and used for triggering on the beam gates. Two external AD signals are digitized directly on the spare channel (Channel 16) of the CAEN V1730B digitizer boards used by the PMT system: An early warning (EW) signal, sometimes also referred to as Beam Extraction Sync (BES), and a Resistive Wall

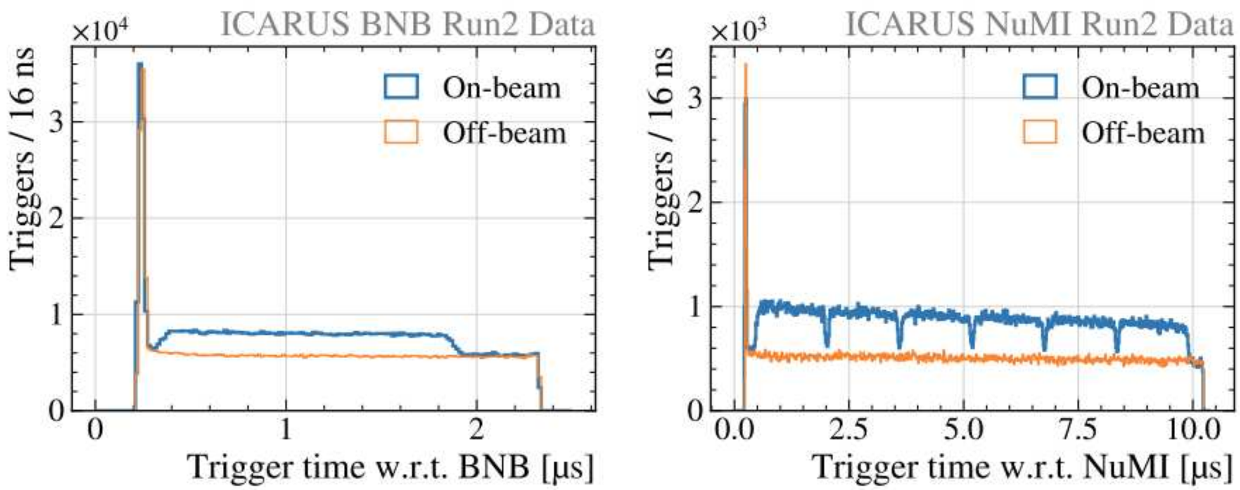

Figure 6.3: ICARUS Trigger time with respect to the beam gate opening for both BNB (left) and NuMI (right).

Monitor (RWM) signal [41]. For each beamline, there are two EW signals sent to ICARUS that we use for triggering: one to generate the enable gate and one to generate the beam gate. Coincidence between beam and enable gates ensures that gate is only opened when proton extraction is directed to respective beam line. For BNB, the signal labeled $1D opens the enable gate arriving 35 ms before the proton extraction to the BNB target. gatedBES is the signal that is used to generate the beam gate for BNB, arriving 0.3 ms before beam extraction. For the NuMI beam, $AE is the label for the signal that opens the enable gate 730 ms before beam extraction to the NuMI target, while the signal labeled MIBS$74 functions as the beam gate arriving 1.75 ms before beam extraction. Delay values for the various BNB and NuMI signals are referenced from [15]. ICARUS operates in neutrino mode by triggering on these signals.

The programmed duration of the beam gates is 2.2 μs and 10.1 μs for BNB and NuMI, while the true beam extraction time is 1.6 μs and 9.5 μs. This extended trigger window can be seen in Figure 6.3 with the trigger time with respect to the beam gate opening shown for both BNB and NuMI, demonstrating the synchronization of the system and our ability to trigger on the neutrino beam spills.

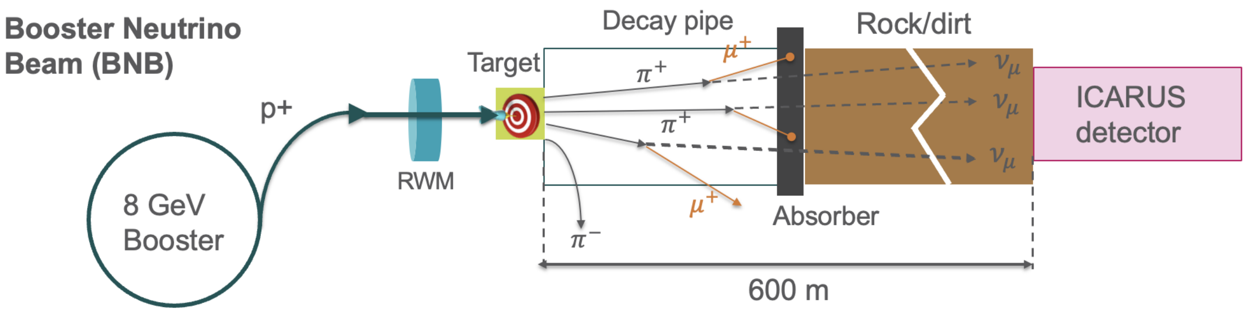

Figure 6.4: Drawing of the BNB Beamline with the Resistive Wall Monitor (RWM) shown.

Figure 6.5: The Resistive Wall Monitor (RWM) showing the circuit board and ferrite used to extract the timing structure of the protons immediately before they hit the target. Picture from [21].

6.2.1 Resistive Wall Monitor

Due to the internal jitter of the trigger, the EW signals alone are not enough to resolve the bunch structure of the neutrino beam. The duration of the spills can be seen in Figure 6.3, but these methods are not able to resolve the structure within the spill, as the jitter of the TTT timestamps is 8 nanoseconds (125 MHz clock). This can be overcome using an additional signal from AD: the resistive wall monitor (RWM). The RWM measures the timing structure of the beam immediately before the protons hit the target.

When charged particles (i.e. protons) travel within a conductive metallic beam pipe, image currents are induced on the beam pipe walls. The RWM measures the image current of the protons in the beamline immediately before they hit the target (see Figure 6.4). A close up view of the RWM, where the beam pipe is cut and a resistive gap is inserted, is shown in Figure 6.5. The

RWM signal is transmitted directly to the ICARUS detector and digitized by the PMT boards, where we sample the leading edge of the RWM pulse. Digitizing the RWM signal directly on the spare channel of the PMT boards bypasses the intrinsic trigger jitter. Offline in our data processing, the RWM and EW times are extracted from the leading edge of the waveform recorded in the spare PMT channel and that time is associated with all PMT channels in that same PMT crate. We do not record the full RWM signal on the PMT digitizers, but the raw RWM pulses with the full structure can be extracted from a Fermilab data base *ifbeam*.

6.2.2 RWM and EW Signal Stability

The stability in the RWM signal is extracted by plotting the difference between the RWM and EW leading-edge times. Plotting the RWM time with respect to a fixed reference (EW) allows us to monitor the stability of the RWM signals across a full run period. The stability of the RWM-EW time difference in Run-2 is shown in Figure 6.6, where an abrupt sign change is observed after run9700 (happening sometime between March 29 and April 1st, 2023). This sign change in the RWM-EW distribution suggested that the RWM and EW cables were swapped inadvertently during a hardware intervention. After investigation at the Far Detector building, it was confirmed that the EW and RWM fibers were swapped on March 29, 2023. This confirmed the value of monitoring the RWM-EW signals across a large run range.

For Run-4, the stability of RWM-EW time difference is shown in Figure 6.7; the median value is plotted to remove outliers. We observe shifts in the RWM-EW timing during known periods of instabilities in the EW (BES) signal at the beginning of December 2024 and again in June 2025. Additionally, in Figure 6.8, we observe some 20 ns jumps throughout Run-4. The 20 ns jumps are a known effect, as sometimes the first bunch in the full 81-bunch-train is not always filled (more discussion on this effect will be provided in Section 6.4). This results in a shift in the RWM time because with a lower peak amplitude, the signal sometimes does not meet the discriminator threshold.

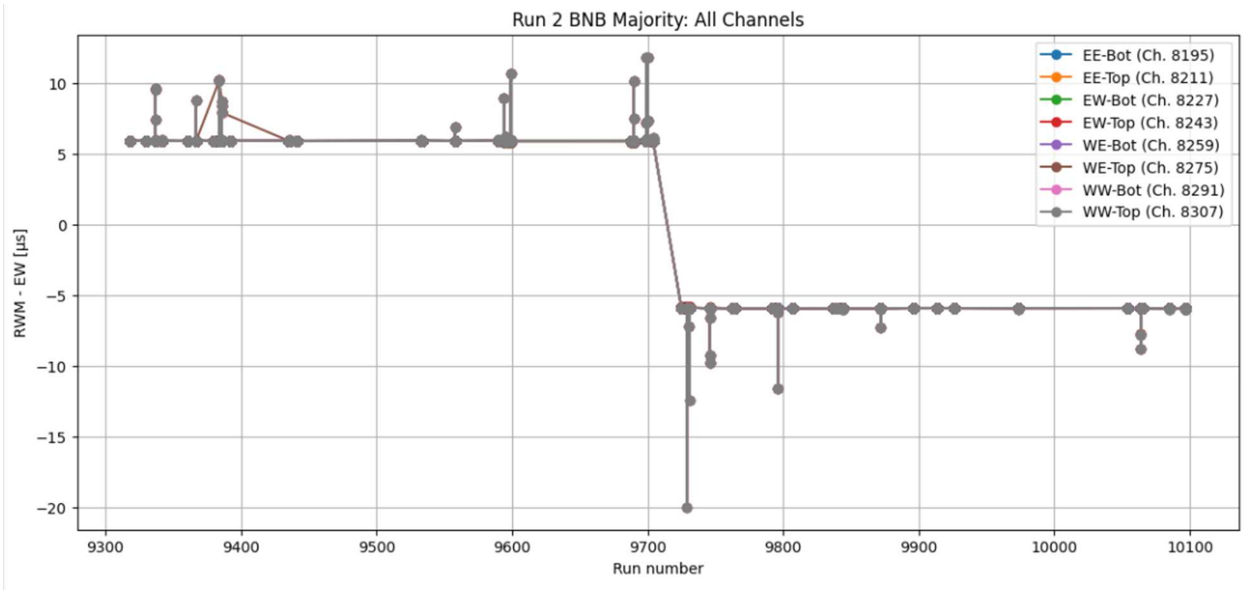

Figure 6.6: Resitive Wall Monitor (RWM) and Early Warning (EW) time difference, showing the stability of the signals across ICARUS Run-2. A sudden sign change is observed after run9700 due to the RWM and EW fibers being swapped following a hardware intervention.

As seen in Figure 6.9, we observe a ∼8-10 ns shift on January 15, 2025. This shift is also apparent in the ICARUS reconstructed beam bunch timing, which will be described in the next section. Upon investigation, it was found that AD was doing work on the Low Level Radio Frequency (LLRF) system that day. Follow up discussions were held with the Booster AD experts, where I was directed to someone in AD who works on the LLRF system. The LLRF expert confirmed that they also see a drop in the first peak time after switching from the digital LLRF to the Direct Digital Synthesis (DDS) system on January 15th. They noted that they went back to the LLRF system sometime in the month of February, however a change in the RWM was not observed then. This suggests that the shifts observed are related to the LLRF platform, but changes do not always give the same response. The cause of the shift is still not understood, but the effect could be related to how the "notch" (or a beam free region) is formed relative to the bunches.

6.3 Beam Event Timing

Several ingredients are necessary to resolve the bunch structure down to the sub-nanosecond level. The first is a RWM signal that is used as a reference signal, providing the time when the

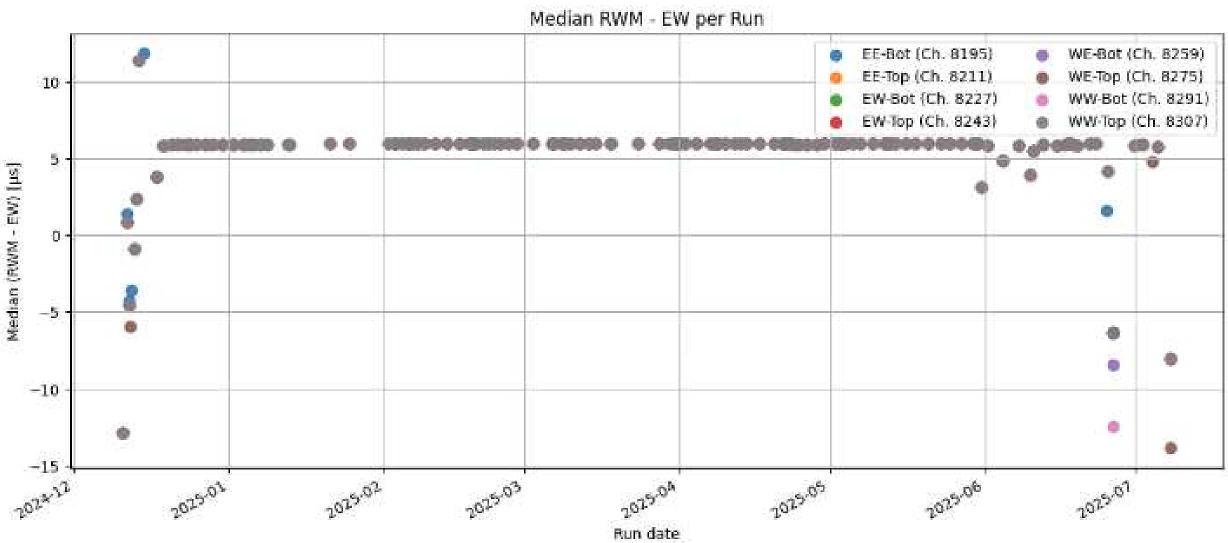

Figure 6.7: Median(RWM-EW) by calender date for all of Run-4

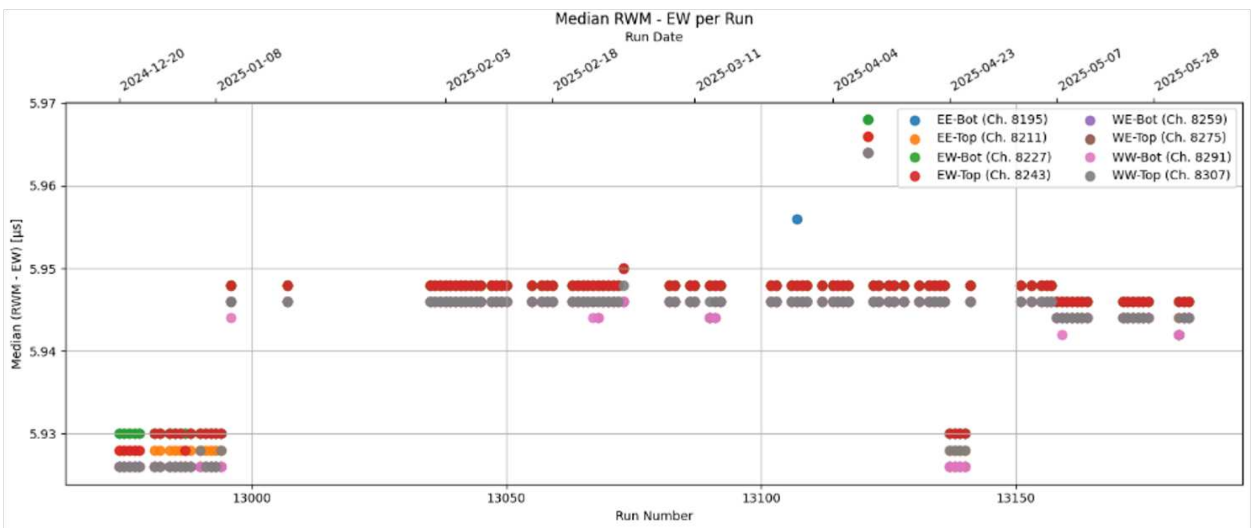

Figure 6.8: Median(RWM-EW) by calender date for all of Run-4

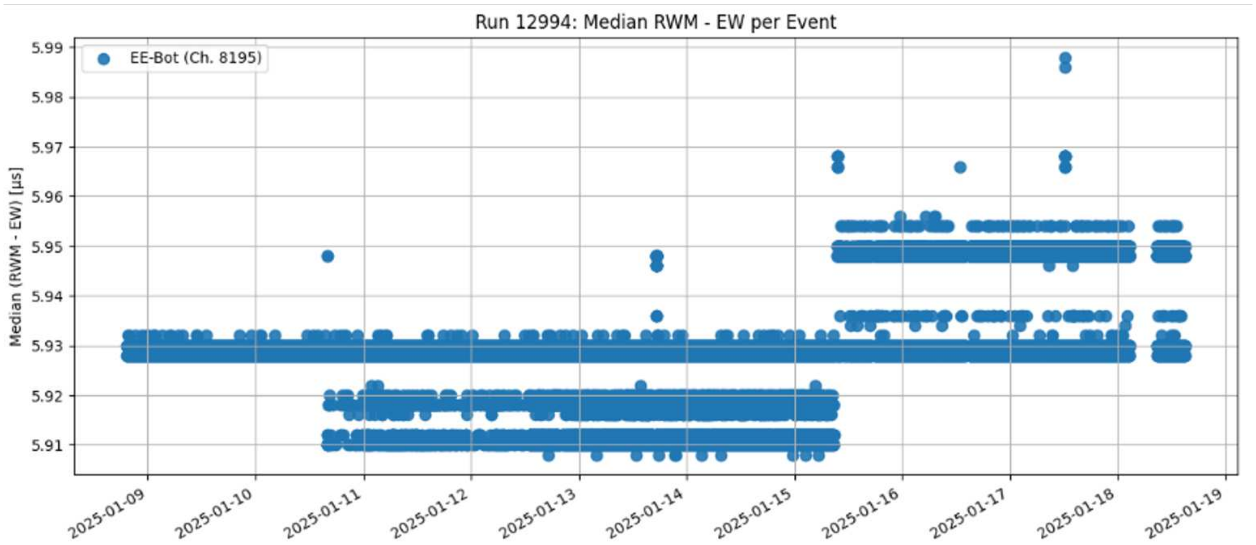

Figure 6.9: Median(RWM-EW) by calender date for run12994, showing an abrupt jump of 10 ns.

first proton bunch hit the target. Individual spills are overlaid on top of one another by measuring the flash interaction time with respect to the RWM signal, demonstrated in Figure 6.10. Using the RWM signal directly is essential because the jitter of the trigger timestamp (40 MHz clock, 25 ns) is too large to resolve the beam bunch structure on its own. However, the PMT digitizers that record the RWM signal have a sampling limit of 2 ns (500 MHz clock). Comparing the "neutrino" flash time with the external RWM signal both acquired by the PMT digitizer allows us to bypass the trigger jitter. As we are dealing with relativistic particles, the transit time from the RWM to the detector, including the time it takes for the protons to hit the target, meson decays and propagation time, and the time it takes for neutrinos to travel 600 m from the BNB target to the detector hall (see Figure 6.4), all can be treated as a constant time offset.

As described in Section 2.1, a single ICARUS-T300 module is composed of a central cathode containing two drift regions with opposite walls read out by an array of PMTs. We leverage the two PMT walls reading out the same T300 by averaging times of first PMTs on opposite walls (see Figure 6.11). Following studies by Vicenzi and an INFN graduate student Riccardo Triozzi, averaging the first times of PMTs on both walls of the same module ($(\mathrm{t}_{\mathrm{L}}^{\mathrm{first}} + \mathrm{t}_{\mathrm{L}}^{\mathrm{first}})/2$) removes the X, Y (drift, height) position dependency and virtually "aligns" the flashes to the center of detector (yellow star in Figure 6.11).

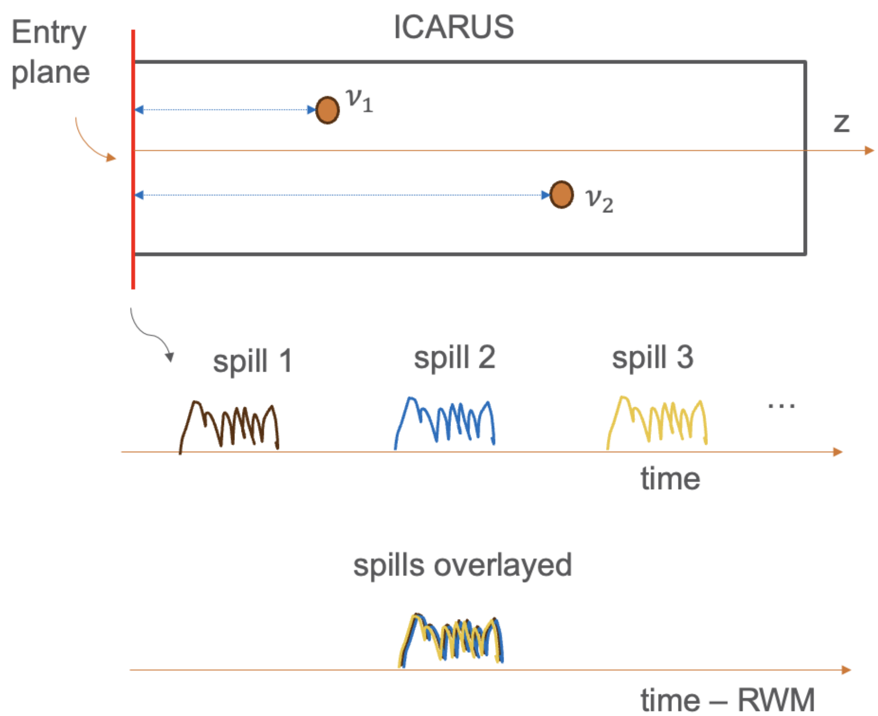

Figure 6.10: Cartoon demonstrating the benefit of using the RWM as a time reference to overlay spills on top of one another.

The last ingredient to resolve the structure is a time-of-flight (ToF) correction from the entry plane to the barycenter of the flash of light, where the barycenter is calculated using the weighted mean of optical hit positions contributing to the flash of light. This final correction effectively "aligns" the flashes to the entry plane which is chosen to be the front face of the cryostat (green diamond in Figure 6.11). This correction is necessary to be able to resolve the individual bunches in the beam spill, and is especially important in a large (19-meter long) detector like ICARUS because the neutrinos can interact anywhere within the detector. Additionally, due to the long length, we could have two bunches interact within the length of the TPCs. Based on the accelerator RF structure, the bunches are spaced by 18.94 ns (52.8 MHz [20]) which corresponds to $\sim$5.7 m, see Figure 6.12.

Finally, the CRT-PMT Matching procedure described in Section 4.7 is used to remove the persistent cosmogenic background (Figure 6.13). This is done by requiring there to be no CRT Hit matched either before or after the flash. The flat constant background, depicted as the plateau regions outside of the central structure in Figure 6.13 is reduced by a factor of of 6.4 from $\sim$800

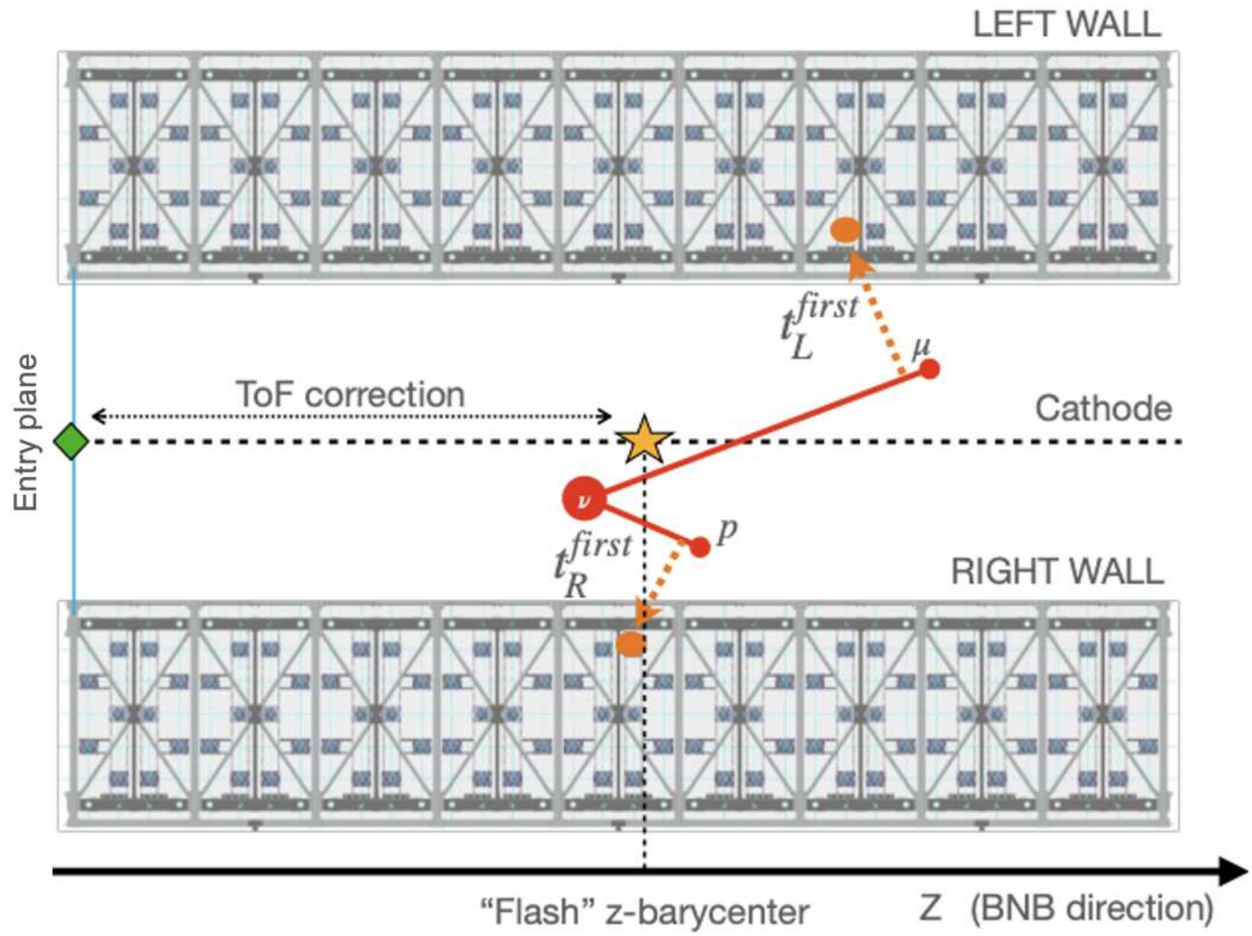

Figure 6.11: Timing corrections to resolve bunch structure.

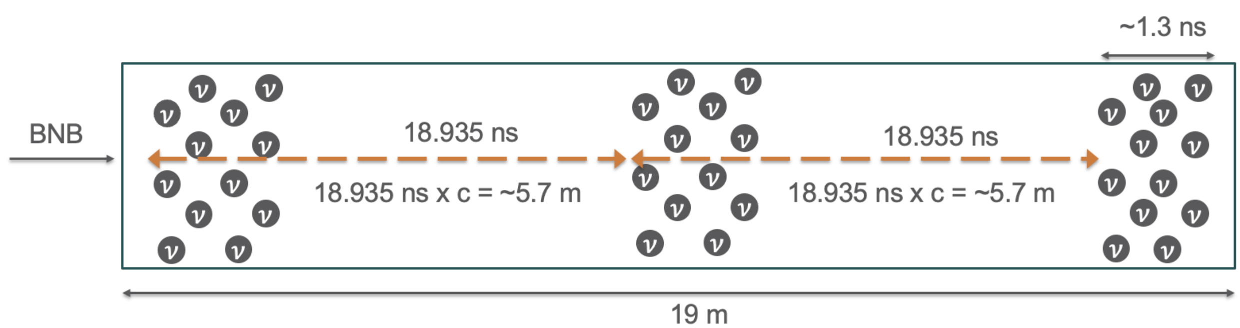

Figure 6.12: Cartoon of bunch spacing within the ICARUS detector (19-meters long along BNB beam direction).

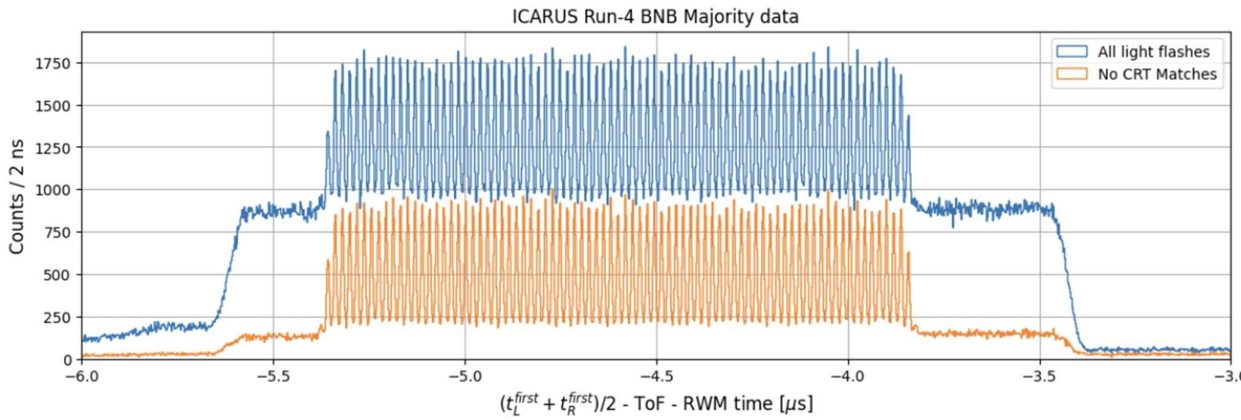

Figure 6.13: Run-4 BNB Majority bunch structure using the Resistive Wall Monitor (RWM) as a time reference, averaging the first PMT times on opposite walls ($(\mathrm{t}_{\mathrm{L}}^{\mathrm{first}} + \mathrm{t}_{\mathrm{L}}^{\mathrm{first}})/2$), and applying a simple ToF correction using the Z barycenter. CRT-PMT Matching is used to reduce the cosmic background.

down to $\sim$125. This cut effectively removes much of the background while preserving the periodic structure in the neutrino spill. There are many features of both the intrinsic bunch structure and the ICARUS trigger system that are apparent in Figure 6.13. We recover the 1.6 µs long spill with 81 individual bunch peaks, with a bunch spacing and width that matches the accelerator parameters. Section 6.4 discusses our ability to reconstruct key characteristics of the accelerator beam such as the bunch spacing and bunch width.

Also evident in Figure 6.13 is the extended 2.2 µs long trigger window that our PMT centric trigger system collects BNB data with, shown by the flat background outside of the main structure. Mostly cosmic events are recorded in the extended trigger window before and after the beam spill arrives at the detector. The range of the plot from -6 µs to -3 µs is just a simple offset introduced by using the RWM time as a time reference. Looking at the ratio between height of the peaks in the bunch region to the plateau region, we see the CRT-PMT cut brings the structure with all light flashes (blue histogram in Figure 6.13) from 1750/800 down to 800/125 with the CRT-PMT cut applied (orange histogram in Figure 6.13), reducing the constant background while maintaining the bunch structure.

6.3.1 Implementation in Common Analysis Framework

Within the SBN Common Analysis Framework (CAF), introduced in Section 4.7.1, the standard is for analyzers to work with CAF files. Following the initial integration in *icaruscode* by Vicenzi, I added the specific variables needed to build the bunch structure to the CAF files. Having the variables directly available in these files eases use for analyzers, allowing them to use it in their selections within the standard analysis workflow. Vicenzi implemented the **BeamTiming** data product within ICARUS' centralized code base *icaruscode*, but the data products need to exist in a SBN common area (*sbncode*) in order to be read into the CAFs. I changed the name-space of this data product within our centralized SBN code base and added a new variable to store the RWM-relative flash time in the CAF files.

6.4 Beam Bunch Structure Reconstruction

Features of the neutrino beam can be extracted by fitting the bunch structure. The separation between neutrino bunches is determined by the accelerator operating frequency, which operates at 52.8 MHz for BNB. In Figure 6.14, I fit the 81-peaks that make up the BNB spill with a Multi-Gaussian. Figure 6.15 shows the bunch structure. The bunch separation can then be extracted with ICARUS by plotting the 81-peak mean times against the peak number and performing a linear fit (see Figure 6.16). A bunch spacing of Δ = 18.935 ns with a fit uncertainty of $\pm$ 0.001 is extracted, which matches the BNB accelerator frequency (52.8 MHz). For a sanity check, I fit this for both Run-2 and Run-4 and see the expected spacing in both data periods.

The width of individual bunches can vary from different run periods, as will be discussed in more detail in Section 6.4.2. For Run-2 and the beginning of Run-4, the width of the individual 81 bunches has an average of 3.04 ns, with a root mean squared of 3.05 ns. After discussion with AD experts, it is expected that there will be some variation in the intrinsic bunch width from bunch-to-bunch. As the bunch structure is periodic, we can use the known separation between bunches to overlay all of the bunches. Each bunch is shifted periodically by taking the modulo (%) of the

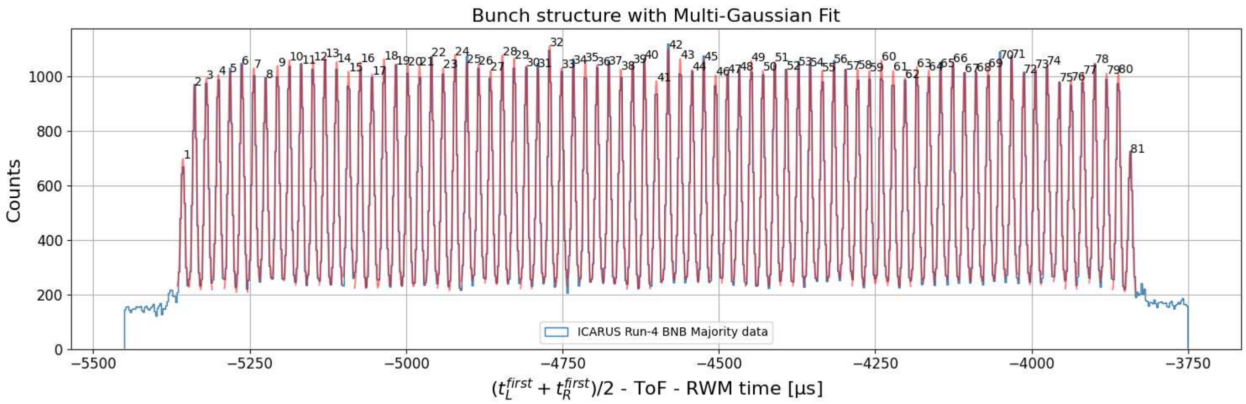

Figure 6.14: BNB bunch structure in Run-4 Majority data with Multi-Gaussian fit overlaid. The 81 peak numbers are drawn above each respective peak.

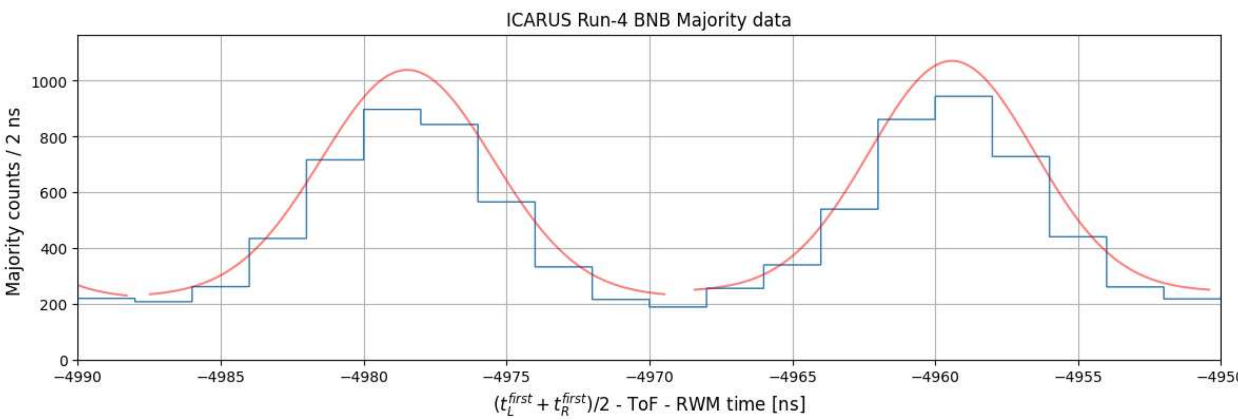

Figure 6.15: Run-4 BNB Majority bunch structure zoomed in on two bunches, showing the 18.935 ns bunch spacing and ∼3 ns individual bunch width reconstructed from neutrino interaction candidates at ICARUS. The 18.935 ns spacing is extracted from fitting the peaks in Figure 6.16 and is consistent with the accelerator frequency (52.8 MHz for BNB). For Run-4, the intrinsic bunch width was $\sim 1.3 - 1.7$ ns (more details on the intrinsic bunch width for Run-4 are provided in Section 6.4.2).

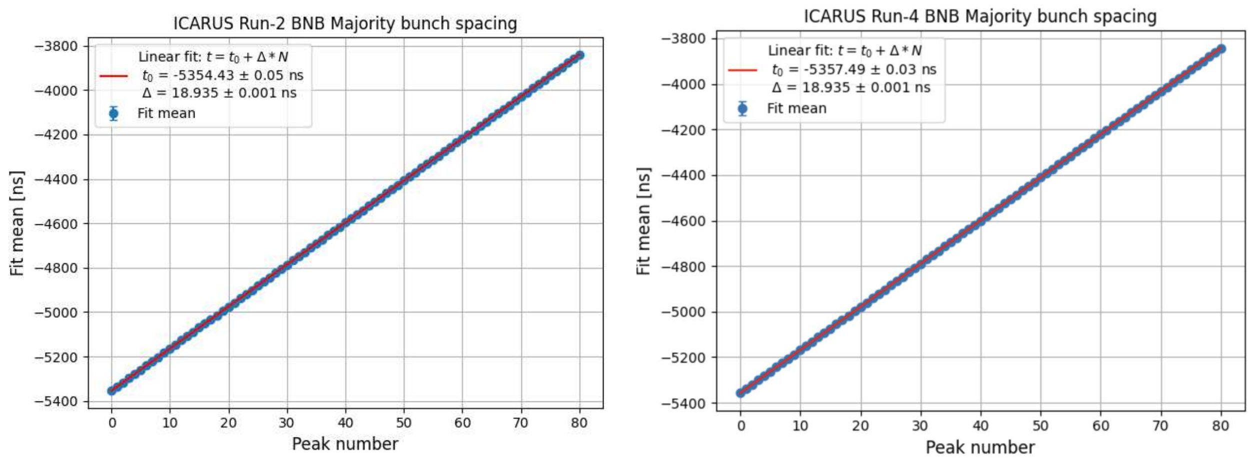

(a) Bunch spacing using Run-2 BNB Majority data collected 12/20/22 - 7/12/23.

(b) Bunch spacing using Run-4 BNB Majority data collected 12/10/24 - 7/8/25.

Figure 6.16: Bunch spacing found by plotting the 81 peak numbers versus the peak mean from the Multi-Gaussian fit for Run-2 (a) and Run-4 (b).

interaction time with

$$\text{Interaction Time} \,\%\, 18.935 = ((\mathrm{t_L^{first}} + \mathrm{t_L^{first}})/2 - \text{ToF} - \text{RWM}) \,\%\, 18.935 \tag{6.1}$$

where $\Delta = 18.935$ ns is the extracted bunch spacing from Figure 6.16. The superimposed bunches found by taking the modulo is shown in Figure 6.17.

A more precise measurement of the reconstructed bunch width is extracted by superimposing the bunches on top of one another, leveraging the fixed periodic structure of the beam. I then fit the superimposed bunch with a Gaussian and extract a reconstructed bunch width from the width (σ) of the Gaussian. In general, a single Gaussian + constant background fit is applied with

$$f(t) = C_{\text{bkg}} + A \cdot \exp\left(-\frac{1}{2}\left(\frac{t-\mu}{\sigma}\right)^2\right) \tag{6.2}$$

where σ is extracted from the fit and represents the reconstructed bunch width, A is the amplitude of the fit Gaussian and $\mathrm{C_{bkg}}$ is the flat background between peaks depicted by the yellow dashed line in Figure 6.17. The fit calculates an average bunch width of σ = 3.07 ± 0.07 ns (see Figure 6.17) in Run-2 BNB Majority data.

In some cases it is useful to look at three superimposed bunches with

$$\text{Interaction Time} \; \% \; (3 * 18.935) = ((\text{t}_{\text{L}}^{\text{first}} + \text{t}_{\text{L}}^{\text{first}})/2 - \text{ToF} - \text{RWM}) \; \% \; (3 * 18.935) \tag{6.3}$$

to better understand how the tails of the Gaussian blend into neighboring peaks. This effect gets smaller with a smaller reconstructed bunch width, as each individual bunch can more clearly be separated from the next. When using Equation 6.3 histograms are fit with a triple-Gaussian function with

$$\begin{aligned} f(t) = C_{\text{bkg}} + \\ A \cdot \Bigg[& \exp\left(-\frac{1}{2}\left(\frac{t-\mu-\Delta}{\sigma}\right)^2\right) \\ & + \exp\left(-\frac{1}{2}\left(\frac{t-\mu}{\sigma}\right)^2\right) \\ & + \exp\left(-\frac{1}{2}\left(\frac{t-\mu+\Delta}{\sigma}\right)^2\right)\Bigg] \end{aligned} \tag{6.4}$$

where the spacing between peaks Δ is fixed by the measured value from Figure 6.16, Δ = 18.935 $\pm$ 0.001 ns and the width σ is common to the three Gaussians. μ is the mean of the Gaussian fit, where the structure is shifted to have the middle peak centered around 0. A is the amplitude of the fit Gaussian and C_{bkg} is extracted from the fit and represents the flat cosmic background depicted by the yellow dashed lines in Figure 6.18. While the CRT-PMT Matching removes much of the cosmogenic background (see Figure 6.13), there is still some a flat constant background remaining in between the bunch peaks, which should be able to be reduced with more advanced cosmic background removal techniques. An example of the triple-Gaussian fit for Run-2 BNB Majority data is shown in Figure 6.18.

6.4.1 Timing Shifts in Run-4 Bunch Structure

In Section 6.2.2, I introduced a 8-10 ns shift observed in the RWM signal stability plots thought to be due to AD switching back and forth between the DDS and LLRF systems. We also reconstruct this effect in ICARUS Run-4 BNB majority data, where 8-10 ns shifts are apparent in Figure 6.19.

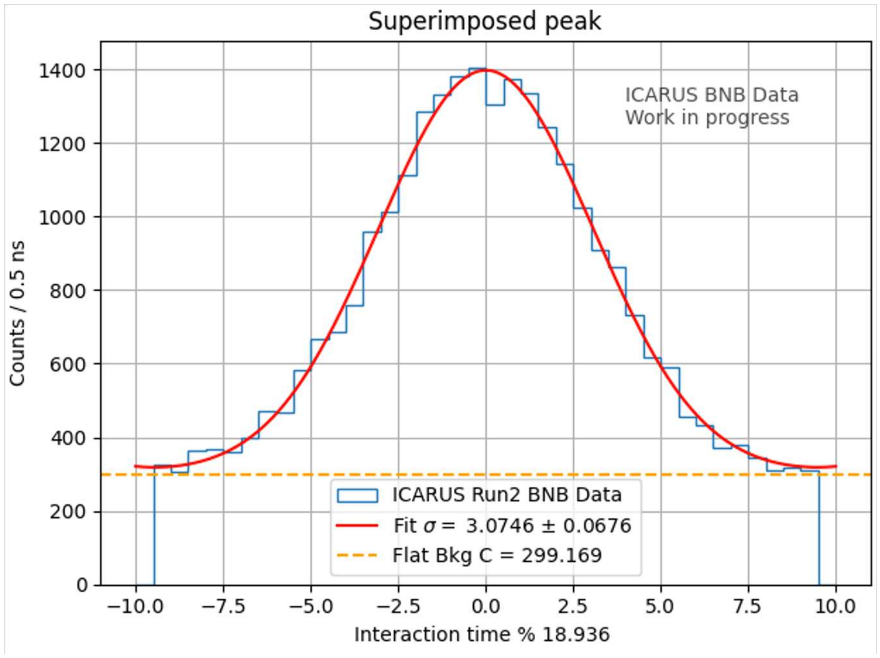

Figure 6.17: BNB Majority Run-2 reconstructed bunch width found by superimposing all 81 bunch peaks by taking the modulo of the interaction time over the bunch spacing.

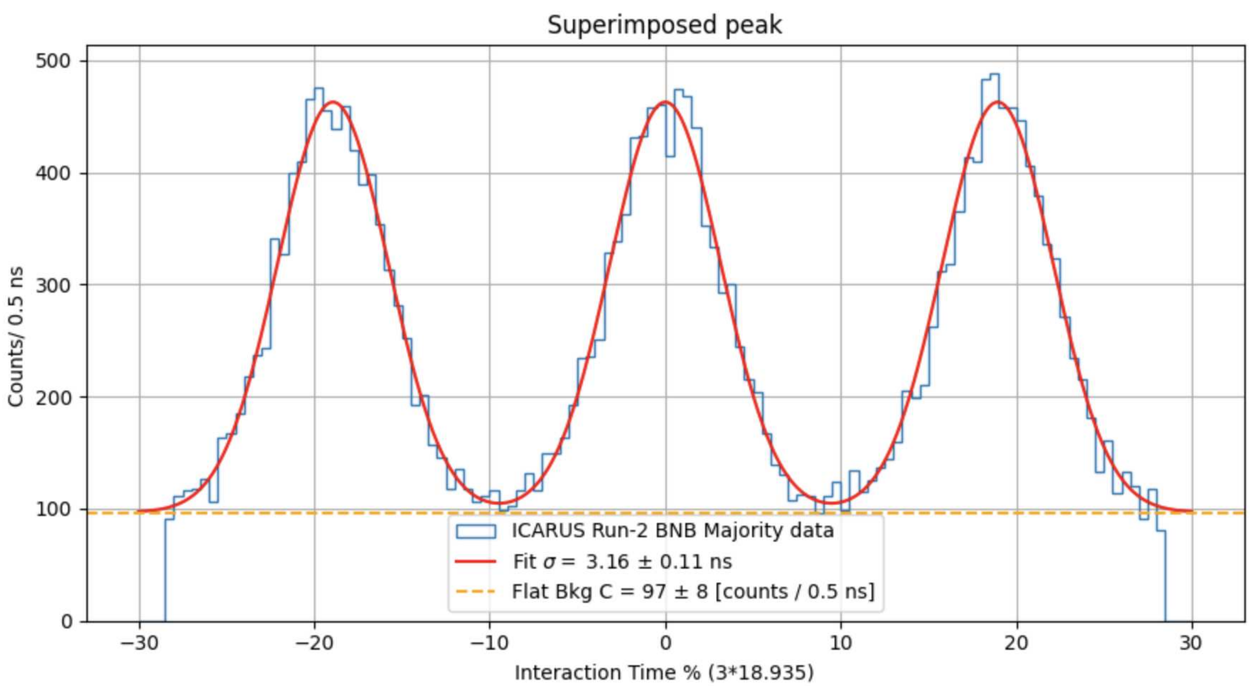

Figure 6.18: Bunch structure with a triple-Gaussian fit using Equation 6.4 on Run-2 BNB Majority data.

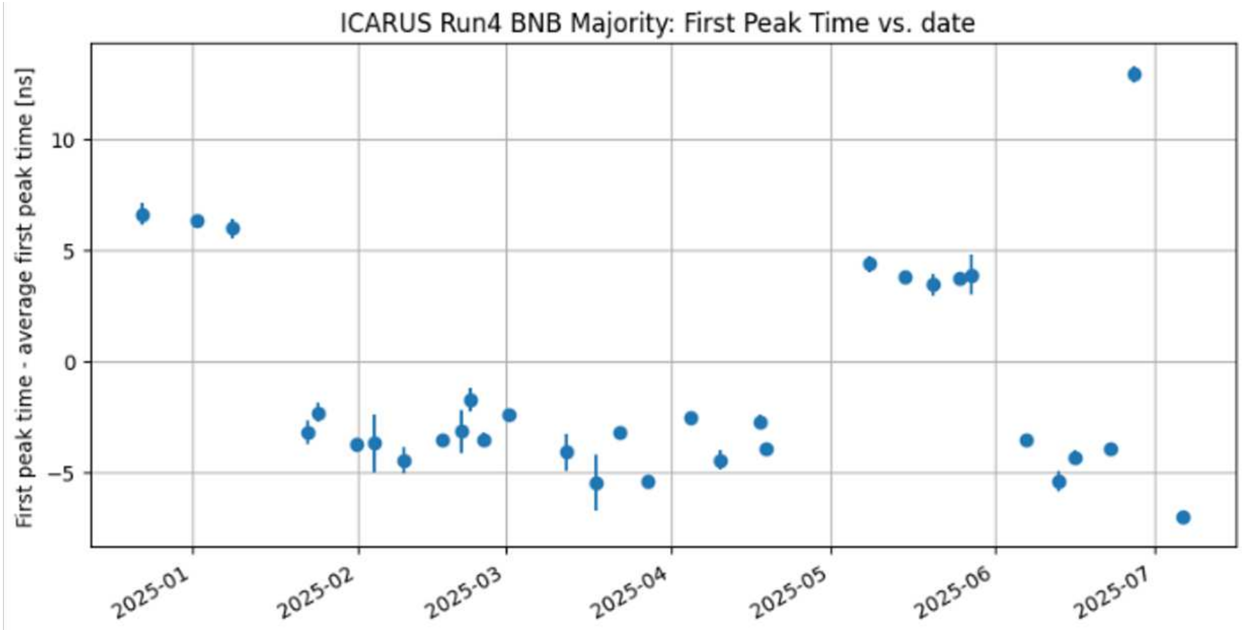

Figure 6.19: BNB Majority Run-4 1st bunch peak times versus calender date.

This effect was also observed by SBND at the same time we see the shifts. A shift of 8-10 ns is important to correct for as it corresponds to half a bunch spacing, which results in the peaks falling in the valleys of different runs, looking like destructive interference between different runs (see Figure 6.20). This demonstrates the importance of effective communication between AD and experiments so the experiments can be informed and adequately correct for these effects.

6.4.2 Bunch Width across ICARUS Runs

To help account for shifts between runs observed in the Run-4 BNB Majority data, I fit and superimposed bunches run-by-run. While the reconstructed bunch width is stable around 3 ns in Run-2 (Figure 6.23a), I observed an unexpected drop in the reconstructed bunch width in our Run-4 BNB data. Figure 6.21a shows data from 19 runs (run12975-13114) collected from in the first half of Run-4 from December 20, 2024 - April 6, 2025 and Figure 6.21b shows data from 14 runs (run13122-13269) from the second half of Run-4 (April 8 - July 7, 2025). Figure 6.22 shows the reconstructed bunch width for those two periods with a Gaussian fit. A clear decrease in the

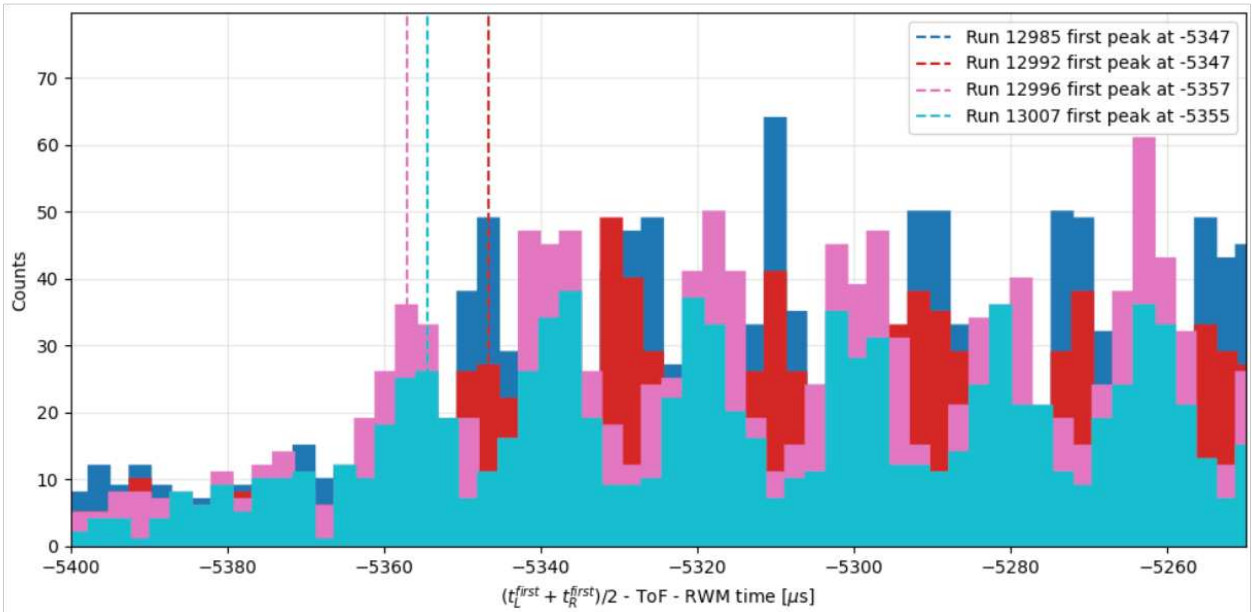

Figure 6.20: An 8-10 ns shift observed between different data runs in Run-4.

reconstructed bunch width is observed from run13114 (ending April 6, 2025) to run 13122 (started April 8, 2025) (see Figure 6.23b).

To understand the decrease in the reconstructed bunch width, I investigated what could have changed in our detector or beam configuration from April 6 to April 7, and discovered that the beam bunch rotation was turned on from April 3 to April 7 following a power outage. While we expect the intrinsic bunch width to be higher with bunch rotation on, it was interesting to see a smaller reconstructed bunch width after this intervention. We would expect to see a slightly higher bunch width for the couple days with bunch rotation on, and then see it return to the same width as before. Instead, I observe a smaller bunch width after AD turned the bunch rotation back off compared to before. Joint discussions with SBND informed us that they also saw a drop in the reconstructed bunch width after April 7, 2025. I met with AD BNB experts to understand if in fact the true intrinsic bunch width became smaller after April 7th. After turning the bunch rotation back off on April 7th, accelerator experts re-tuned the BNB back to nominal beam conditions, resulting in a smaller, more optimal bunch width. To verify this, I extracted the raw RWM traces from the database stored by AD (see Figure 6.24) to check for any change in the raw RWM signal, which samples the pulse right before the beam hits the target.

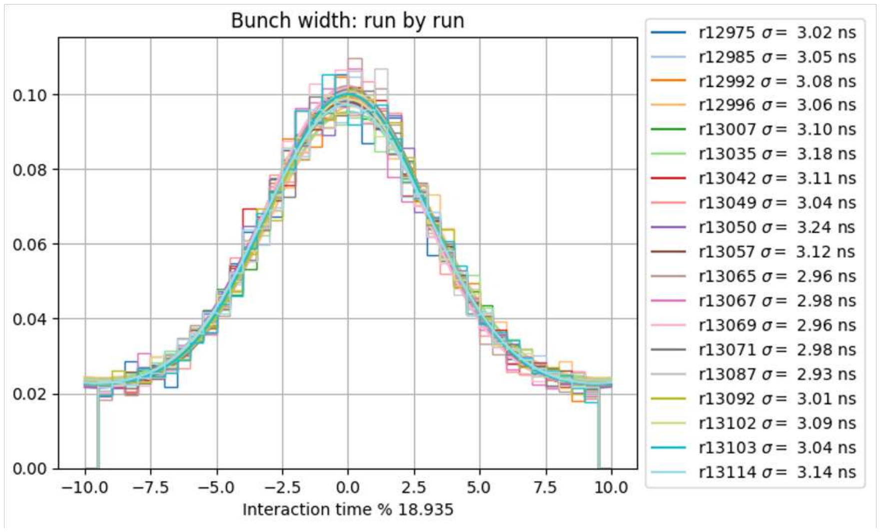

(a) 19 runs (run12975-13114) collected from December 20, 2024 - April 6, 2025 with an average bunch width of 3.05 ± 0.02 ns.

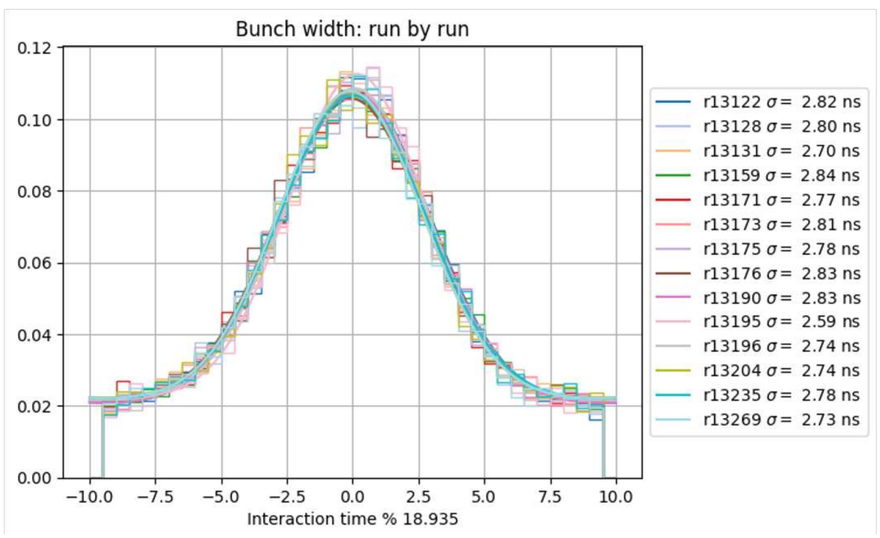

(b) 14 runs (run13122-13269) collected from April 8 - July 7, 2025 with an average bunch width of 2.78 ± 0.02 ns.

Figure 6.21: Superimposed reconstructed BNB bunch width plotted run-by-run for Run-4 BNB Majority data. **(a)** shows data from the first half of Run-4 and **(b)** shows data from the second half of Run-4.

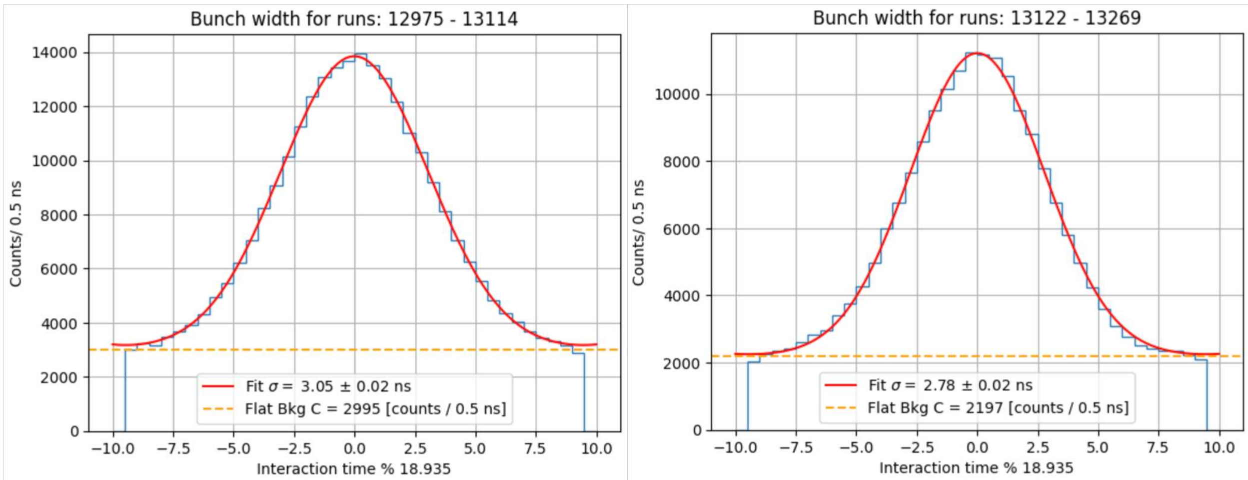

(a) First half of Run-4 (December 20, 2024 - April 6, 2025). **(b)** Second half of Run-4 (April 8 - July 7, 2025).

Figure 6.22: Superimposed BNB bunch width with Gaussian fit for the first **(a)** and second **(b)** half of Run-4 BNB Majority data.

Looking at the raw RWM pulses informs us about the beam conditions directly at the source. An example of the bunch width extracted from the RWM traces can be seen in Figure 6.25 and Figure 6.26. The RWM traces from *ifbeam* show a noticeable change in the intrinsic bunch width from approximately 1.7 ns to 1.3 ns, which agrees with the change we see in ICARUS. The hypothesis for why we see this decrease is that after bunch rotation was turned back off on April 7th, AD re-tuned the beam which left us with a smaller intrinsic bunch width. A smaller width is optimal for both background rejection for neutrino selection and BSM searches. This made us aware that the ICARUS PMT system is sensitive to small changes in the intrinsic bunch width.

6.4.3 Narrow Bunch Beam Test

In Spring 2026, the Fermilab Accelerator Division wanted to explore running the beam with a narrow bunch beam configuration, with an intrinsic BNB width of less than 1 ns, compared to "nominal" running with a 1.31 ns width with bunch rotation off. As this configuration is very interesting for my analysis, I coordinated with AD and the experiments situated along BNB (our near detector SBND and the ANNIE experiment, located directly upstream from SBND) to organize a long enough test run so we can gather enough statistics with the ICARUS detector to resolve

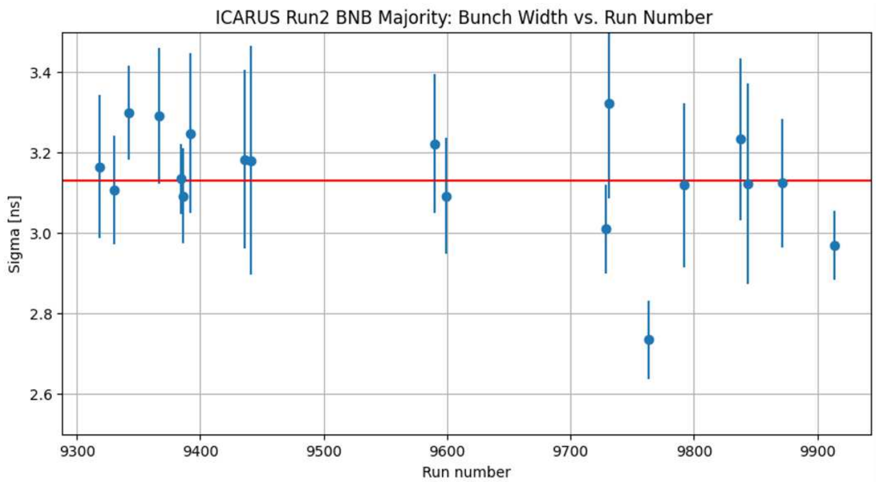

(a) Run-2 reconstructed bunch width (sigma) as a function of run number. The red line represents the average sigma at σ = 3.07 ns

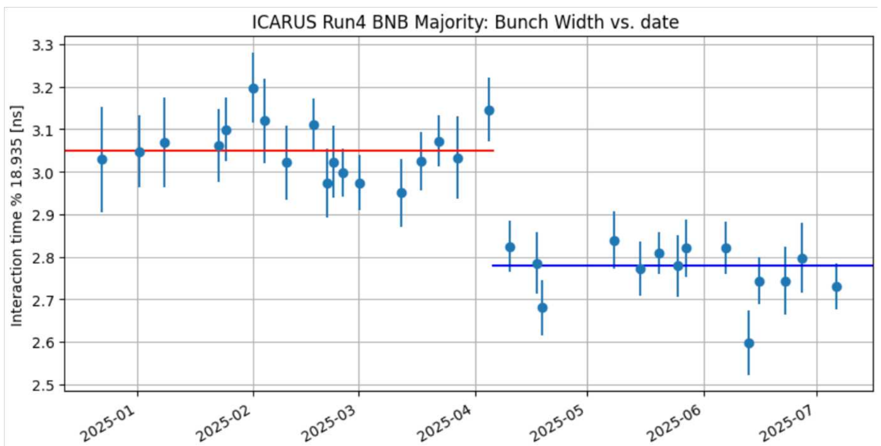

(b) Run-4 reconstructed bunch width (interaction time % 18.935 ns) as a function of calender date. A clear decrease in the bunch width is observed after April 7th, 2025. The red line represents the average bunch spacing in the first half of Run-4 at 3.05 ns and the blue line represents that in the second half of Run-4 at 2.78 ns.

Figure 6.23: Run-2 (a) and Run-4 (b) reconstructed bunch width versus Run number or date.

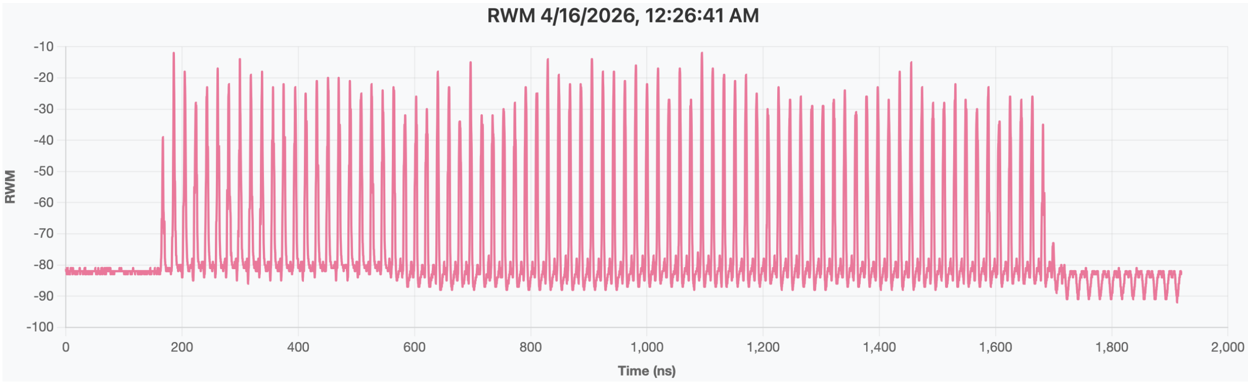

Figure 6.24: Example raw RWM Trace from *ifbeam*. The RWM samples the proton structure of the proton beam immediately before it hits the neutrino beam target. Two reflections at ∼34-36 ns and ∼400 ns are visible, which are consistent with the known propagation times for cables connected to the RWM [22].

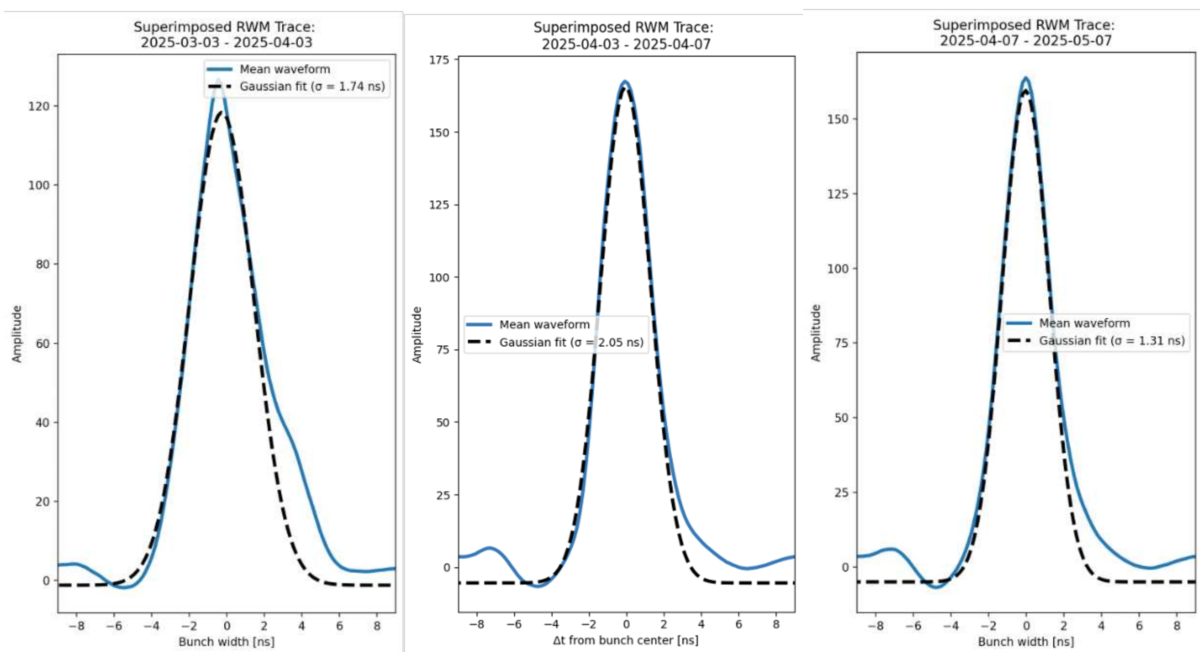

(a) Bunch rotation OFF **(b)** Bunch rotation ON **(c)** Bunch rotation OFF

Figure 6.25: RWM Traces from *ifbeam* database for dates ranges before (a), during (b) and after (c) bunch rotation was turned on. The asymmetry in the pulses observed in the superimposed waveforms is a known feature and due to the attenuation of pulses along the cables [23].

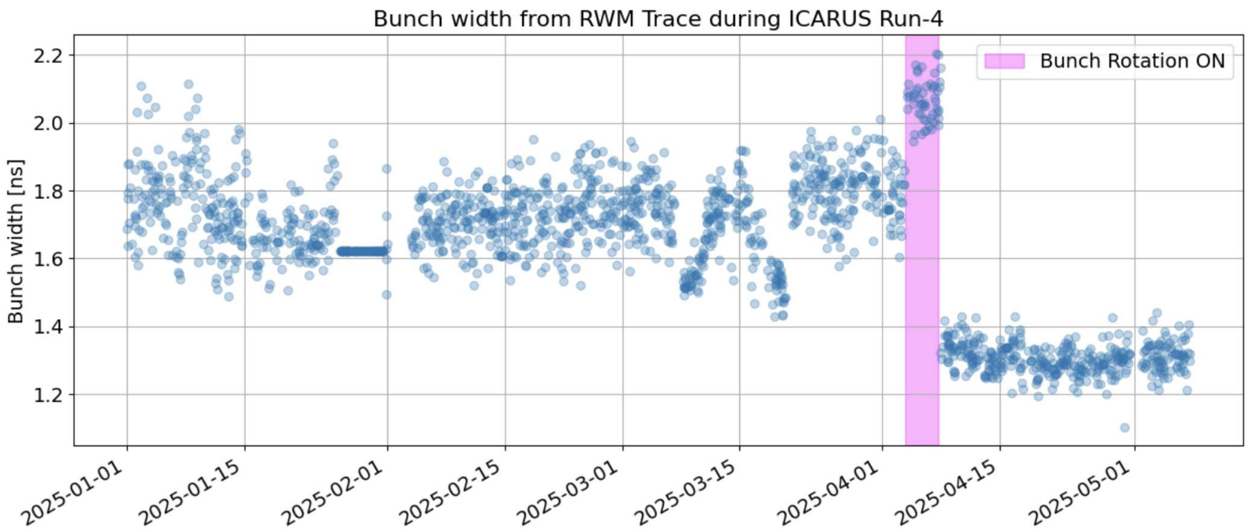

Figure 6.26: RWM traces from *ifbeam* database across ICARUS Run-4.

the narrow bunches. Since ICARUS is much further from the target (600 m) compared to SBND (110 m), we need higher statistics to resolve the bunch structure of the beam. From the analysis of the run-by-run fitting performed for Run-4 BNB Majority data, I estimated we would need around 50 hours running to resolve the bunch structure of the beam. After discussion with AD, beam experts, ICARUS and SBND management, we decided to run for 50 hours with the narrow beam configuration which would provide enough data to enable ICARUS to resolve the beam structure.

The narrow bunch beam tests were started around 11 am on Tuesday, March 31, 2026 and lasted until 2 pm on April 2, 2026. After some preliminary tests, AD and BNB experts were able to establish a narrow bunch beam with an average bunch width of 0.87 ns and $4.5 \cdot 10^{12}$ POT intensity. I worked in real time to analyze this data for rapid feedback to ICARUS management and the accelerator division.

To understand the reduction from the nominal Run-5 beam width, I compared the narrow beam run (run14165) with a run collected the weekend before the narrow beam bunch tests (run14163). run14163 is a 68:56 hour run collected from March 27-30, 2026 with an intrinsic BNB bunch width of $\sim$1.3 ns. run14165 is the narrow beam run collected for 50:38 hours from March 31-April 2, 2026 with an intrinsic BNB bunch width of $\sim$0.87 ns. From these tests, we resolve a bunch

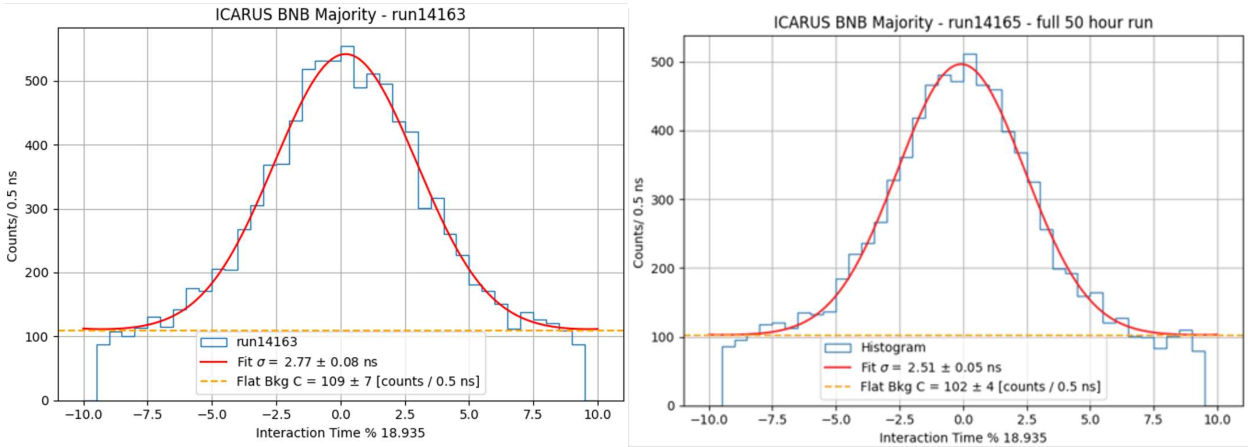

(a) run14163 with nominal Run-5 BNB bunch width. **(b)** run14165 with narrow beam configuration.

Figure 6.27: Comparison of the nominal Run-5 reconstructed bunch width and the bunch width reconstructed with the narrow beam bunch configuration. **(a)** shows run14163, a 68:56 hour run collected from March 27-30, 2026 with the nominal Run-5 BNB beam configuration (~1.3 ns intrinsic BNB bunch width) and **(b)** shows run14165, a 50:38 hour run collected from March 31-April 2, 2026 with the narrow beam bunch configuration (~0.87 ns intrinsic BNB bunch width).

structure of 2.51 $\pm$ 0.05 ns with the ICARUS detector in run14165 (Figure 6.27b), compared to 2.77 $\pm$ 0.08 ns with the nominal Run-5 beam configuration in run14163 (Figure 6.27a).

Intrinsic Detector Resolution

Using the reconstructed bunch width we observe at ICARUS and the intrinsic bunch width, we can obtain an upper limit on a measurement of the intrinsic detector resolution, R, of the PMT system in ICARUS.

$$R = \sqrt{\sigma^2_{\text{ICARUS Fit}} - \sigma^2_{\text{BNB}}} \tag{6.5}$$

We have measurements of the bunch width in four different beam running configurations, summarized in Table 6.1.

The intrinsic BNB beam width was measured to be 1.31 $\pm$ 0.03 ns with bunch rotation OFF. Using the lowest bunch width value found for Run-4, 2.78 ns, we find an estimated upper bound for the detector resolution to be approximately 2.44 ns using timing information alone. Incorporating the TPC (charge) reconstruction information is expected to improve this measurement. Instead of using flash barycenter position, the vertex position from the TPC should give a better ToF

Configuration	σ_{BNB} (ns)	$\sigma_{\text{ICARUS Fit}}$ (ns)	R (ns)
Run-2 (BR on)	1.95 ± 0.02	3.08 ± 0.07	2.38 ± 0.09
Run-4 a	1.74 ± 0.03	3.05 ± 0.02	2.47 ± 0.03
Run-4 b / Run-5	1.31 ± 0.03	2.78 ± 0.02	2.44 ± 0.03
Run-5 narrow beam	0.87	2.51 ± 0.05	2.35

Table 6.1: Various beam configurations with the intrinsic BNB width σ_{BNB}, ICARUS reconstructed bunch width $\sigma_{\text{ICARUS Fit}}$, and estimated detector resolution R using Equation 6.5. ICARUS Run-2 had bunch rotation (BR) on and "Run-5 narrow beam" is from the 50 hour BNB Narrow Beam test with the Fermilab Accelerator Division.

correction. A preliminary investigation of the improvement from the TPC vertex correction is shown in Figure 6.28. A reduction of approximately 0.5 ns is observed by using the TPC vertex position for the ToF correction, which agrees with the improvement expected from incorporating charge information.

The bunch width fit we extract at ICARUS includes the PMT timing resolution, the intrinsic bunch width measured by AD, and the uncertainty on the first proton bunch peak time (T0) from the discriminated RWM pulse sampling. After consulting with SBND and MicroBooNE colleagues, the resolution of the discriminated RWM pulse is estimated to be close to 1 ns due to an effect from the timewalk. Timewalk is an affect on a fixed trigger threshold for signals of varying amplitude. In plots of the raw and reconstructed bunch structure, we observe that the 1st peak height is less than the second peak height (for example, see first bunch peak Figure 6.14). This is a known effect and can have an effect the time discriminated RWM pulse goes over threshold, which determines the T0. The measurement of 2.44 ns is thus overestimating the PMT intrinsic detector resolution considering the spread of the T0 signal from the RWM. This effect can be removed by subtracting out 1 ns in quadrature, providing a timing resolution of approximately 2.23 ns for the ICARUS PMT system.

6.5 Applications of Precise Beam Timing

Our ability to resolve the beam bunch structure has many uses including background rejection for both neutrino selection and BSM searches. For neutrino selection, the persistent cosmic back-

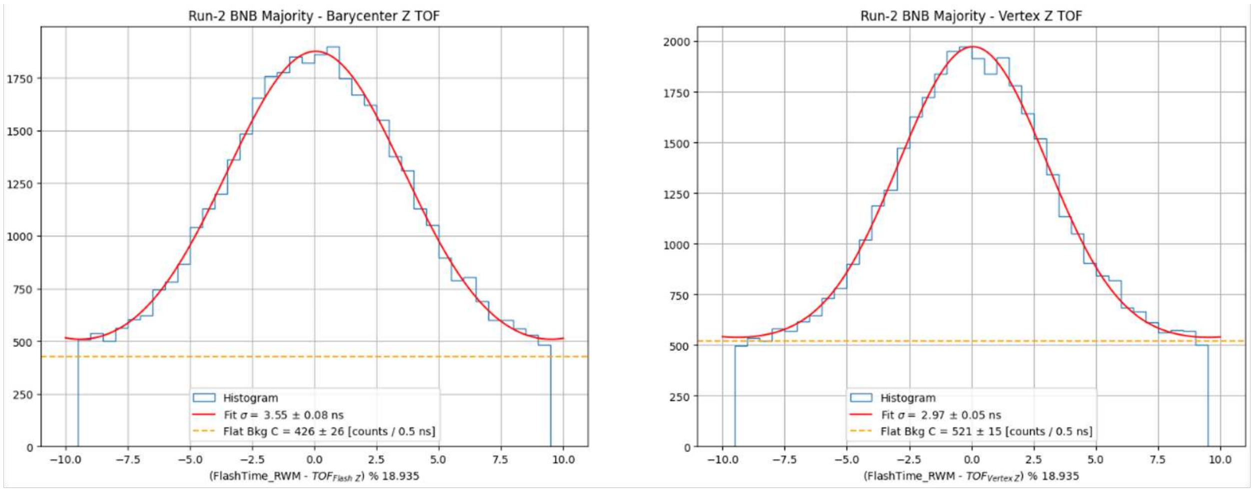

Figure 6.28: (left) Bunch width using flash barycenter Z-position for TOF correction, (right) Bunch width using TPC vertex Z position for TOF correction.

ground can be reduced by selecting events in the beam bunch, effectively removing the background in between peaks. In addition, precise timing information can be leveraged in BSM searches as will be discussed in Section 6.5.6. My work focuses on using the beam bunch timing to select neutrino events from our Minimum Bias data stream to remove bias from the triggering logic.

6.5.1 Neutrino Selection

The beam structure can be leveraged for background rejection for neutrino selection. Background events not correlated with the beam (ie. cosmics) arrive uniformly in time, while the neutrinos arrive in fixed bunches from the structure of the proton spill. The flat background depicted by the yellow lines in the reconstructed bunch width plots (see Figure 6.22) can be reduced by performing a cut around the beam bunch peak, exploiting the periodic structure of neutrino arrival.

The neutrino efficiency and background rejection is estimated from Run-4 BNB Majority data with a reconstructed bunch width of 2.77 ns observed in the second half of the run, which is used to used to study the effect on selecting neutrinos while reducing the constant background. Neutrino selection efficiency is estimated from the fraction of beam correlated events in an example selection window around the beam bunch peak. This is extracted by integrating the fit bunch width up to an example cut value ($|t - t_0|$) from 0 to half a bunch spacing (18.935 / 2 ns). The neutrino efficiency

Cut	Neutrino efficiency (%)	Background rejection (%)
$\pm\ 3\sigma$ (9.22 ns)	99.9	1.9
$\pm\ 2\sigma$ (6.15 ns)	95.4	34.6
5 ns	89.6	50
$\pm\ 1\sigma$ (3.07 ns)	68.2	67.3

Table 6.2: Neutrino efficiency vs. background rejection for an example ± 1, 2 and 3σ cut around the beam bunch peak for a bunch width of σ = 3.07. An example cut at 5 ns is also shown for reference.

defined here is essentially the integral of the Gaussian fit in Equation 6.4, where the integral of a Gaussian is commonly referred to as the Error Function and is used to estimate the neutrino efficiency. Figure 6.29 shows the neutrino efficiency as a function of a cut around the beam bunch peak ($|t - t_0|$). The background rejection calculation assumes a flat background, as cosmics arrive at the detector uniformly in time.

With the flat background, widening the cut around the beam bunch peak introduces more background linearly, so the background rejection fraction decreases linearly with ($|t-t_0|$). Figure 6.29b shows the flat background rejection plotted against neutrino efficiency. In both figures, 1, 2 and 3-σ cut values are shown to benchmark the impact of a cut around the beam bunch peak for different cut values, as shown in Table 6.2. An example cut at 5 ns around the interaction time peak removes roughly 50% of the constant background while preserving 92.8% of the neutrino signal using light only (see Figure 6.29). This demonstrates how the beam bunch structure is yet another tool we can use to remove backgrounds for neutrino selections by selecting events close to the beam bunch peak.

6.5.2 Bunch Structure in Minimum Bias Data Stream

As discussed in Section 3.3, Minimum Bias triggers are collected both on-beam and off-beam to provide an unbiased data sample. Due to the pre-scale, Minimum Bias data has significantly fewer statistics as the on-beam Minimum Bias triggers are collected only once every 200 (40) on-beam gates for Run-2 (Run-4). Figure 6.30 shows the BNB Majority data overlaid on the BNB Minimum Bias data, zoomed in on the first 19 bunches of the 81 bunches making up the BNB

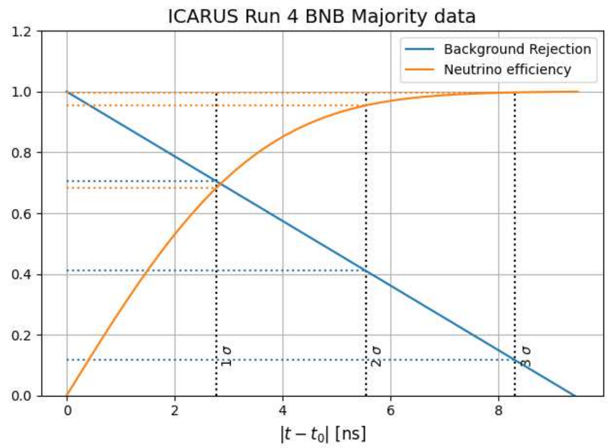

(a) Neutrino efficiency and cosmic rejection as a function of a cut around the main bunch peak.

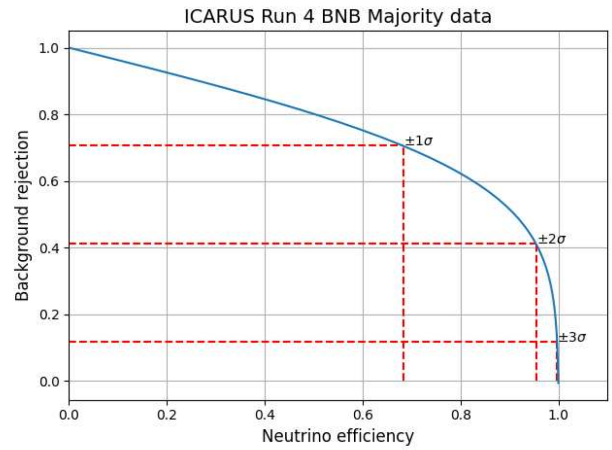

(b) Neutrino efficiency vs. cosmic rejection .

Figure 6.29: Neutrino efficiency and cosmic rejection for a bunch width of 2.77 ns found in Run-4 BNB Majority data.

spill (see Figure 6.30a for Run-2 and Figure 6.30b for Run-4). Leveraging the fixed periodic time structure in both datasets, the bunch structure from the BNB Majority data stream can be used to select neutrinos from the BNB Minimum Bias data stream. This is the first time the bunch structure has been resolved in the unbiased dataset. This dataset has not yet been thoroughly investigated for neutrino selection, so this work is demonstrating a new use of this data for the collaboration.

Shift in Run-2 BNB Minimum Bias Structure

In Figure 6.30a, we observe a shift of approximately 19 ns between the Minimum Bias and Majority bunch structure. This shift is close to one bunch spacing of 18.935 ns and is currently not understood. One explanation could be related to the RWM signal not going over threshold. Sometimes the first bunch is only partially filled and might not always reach the RWM trigger threshold, which would delay the signal to the subsequent bunch. Why this feature would show up in one data stream and not the other is not clear.

6.5.3 Selecting Neutrinos from Minimum Bias Data Stream

Our ability to see the beam bunch structure in the BNB Minimum Bias data allows to select neutrinos from this unbiased data stream. I initially looked at Run-2 BNB Majority events as

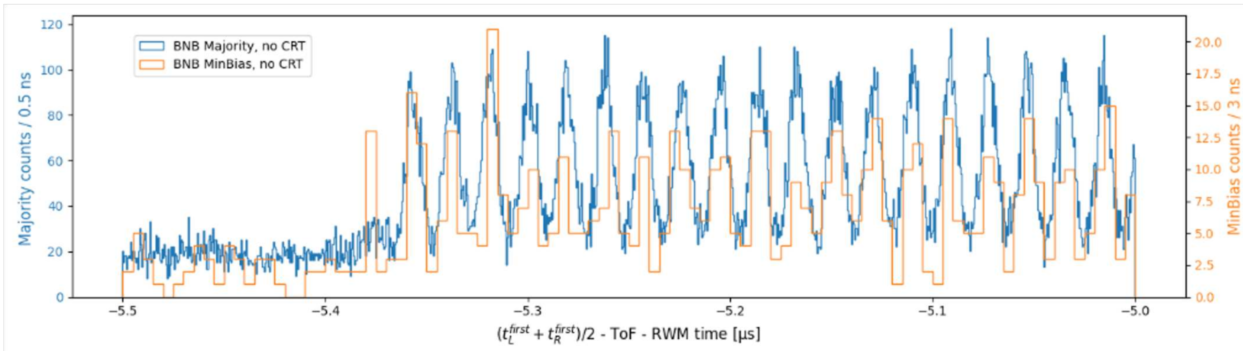

(a) Run-2 data from run9435-run9599 (January 29, 2023 - February 19, 2023).

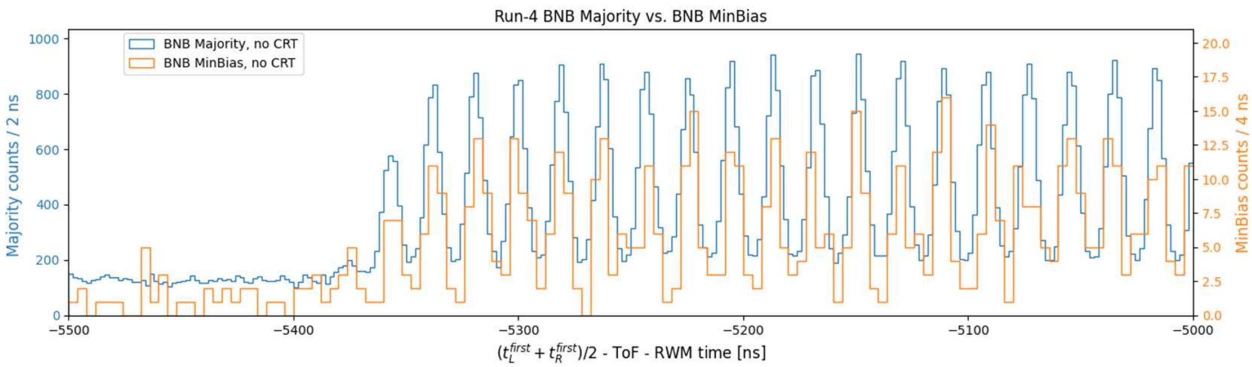

(b) Run-4 data from run12996-run13137 (January 19, 2025 - April 23, 2025).

Figure 6.30: BNB Majority stream bunch structure overlaid on BNB Minimum Bias data, zoomed in on the first 19 bunches out of the 81 total bunches in the bunch train making up the BNB spill.

"mini-selection" to verify we can cleanly select events with beam timing alone. The Run-2 BNB Majority sample has also been studied in great detail within the ICARUS oscillation analyses, so this can be a useful dataset to study. To select events with beam timing, I look for events with an interaction time within 3 ns of the beam bunch interaction peak, with the cut values driven by the selection efficiency show in Figure 6.29.

Using the TITUS event display introduced in Section 2.3, I studied a few of the Run-2 selected events and identified BNB Majority neutrino event candidates using beam bunch timing information alone. For an example of a selected BNB Majority event candidate, see Figure 6.31. The selected flash informs what cryostat the flash occurred in and the reconstructed flash barycenter Z-position indicates where along the detector length the selected flash was, so this information was used to help identify and verify the identified neutrino interaction in TITUS. After this proof of concept with the Majority data, I looked for events in the Run-2 BNB Minimum Bias data stream and performed the same activity by selecting events using timing information alone, and immediately identified a neutrino candidate from the Minimum Bias stream.

An estimate of the number of triggered and Minimum Bias neutrino induced events can be obtained from the observed trigger rates in Run-2 and Run-4. In Run-2, we see an average trigger rate of 31.5 mHz from the BNB. This is found by taking the difference between the on-beam and off-beam BNB Majority rates. With the beam operating at the nominal 4 Hz (resulting in 9.33 million BNB beam gates per month) and given the trigger rate, we expect 73,000 neutrino induced events per month. For Minimum Bias, we need to consider the pre-scale which was 200 for Run-2 on-beam BNB resulting in an expected 367 neutrino induced Minimum Bias events per month. For a 7-month BNB run, this would result in a total of 514,000 neutrino induced events from BNB Majority, with an additional 2,570 neutrino induced events from the Minimum Bias data stream in Run-2.

For Run-4 data, we have an estimated average trigger rate of 38 mHz with BNB operating at 4.9 Hz, which can operate at a higher rate without NuMI running. A similar calculation for the neutrino induced rates from Run-4 estimates $\sim$700,000 neutrino induced events from the triggered

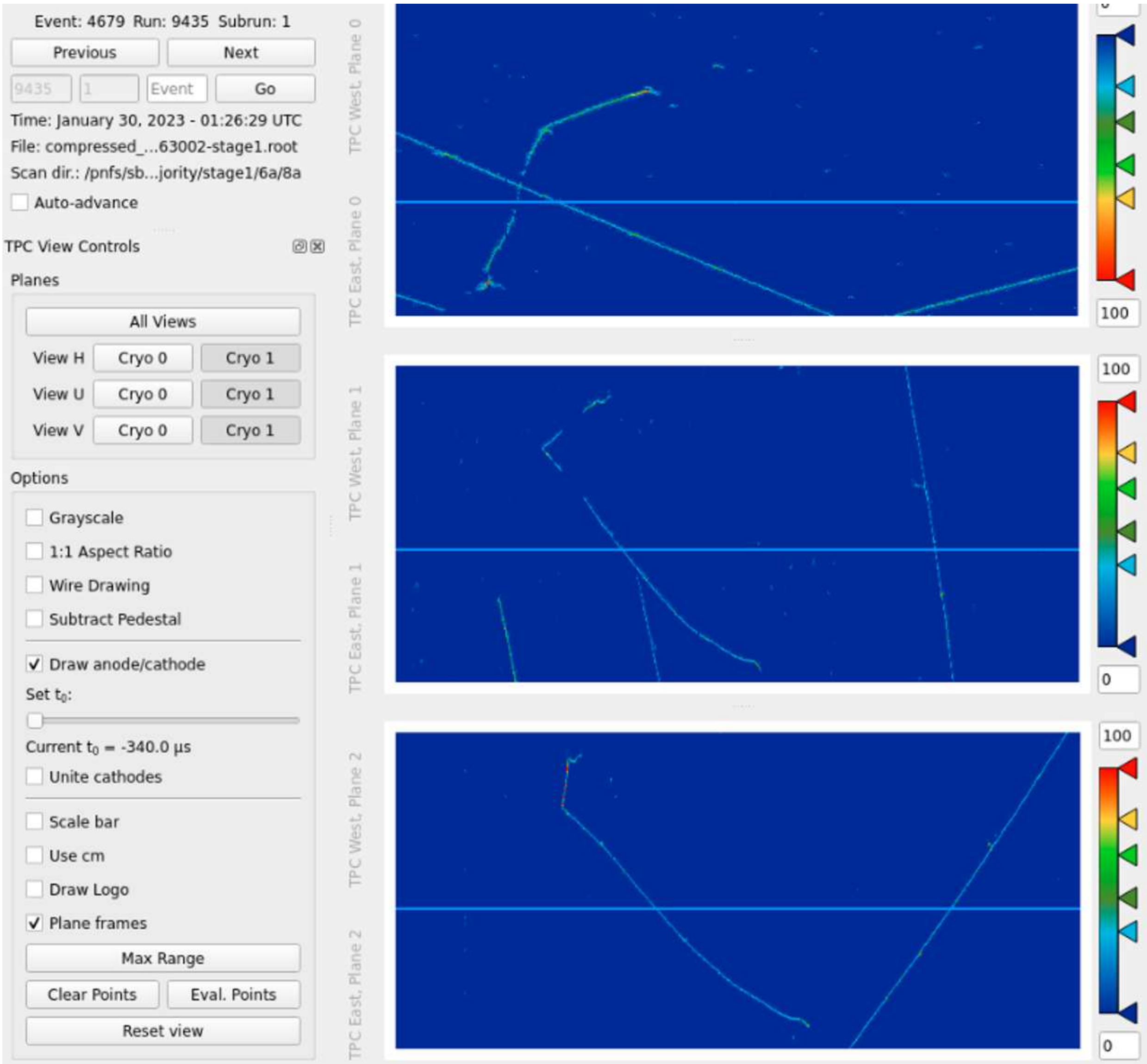

Figure 6.31: Run-2 BNB Majority run 9345 event 4679 in TITUS event display, an example of a BNB Majority event candidate selected with PMT timing information.

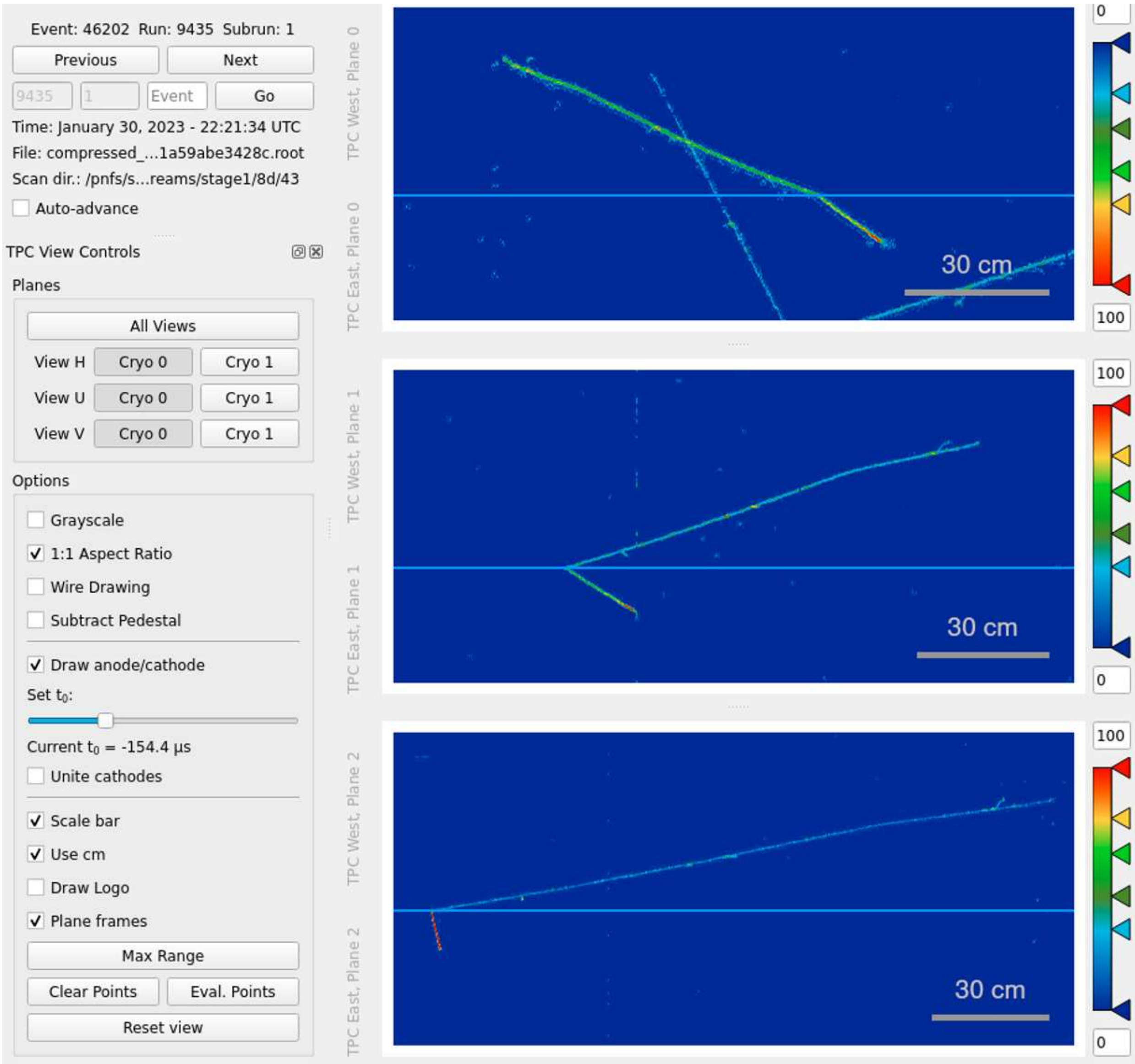

Figure 6.32: Run-2 Minimum Bias run 9435 event 46202 in TITUS event display, an example of a BNB 1µNp Minimum Bias event candidate selected with PMT timing information.

data stream, with an additional ∼17,000 neutrino induced events from the Minimum bias data stream. This provides a rich and unbiased sample to study.

Due to the timing shifts discussed in Section 6.4.2, for the Run-4 Minimum Bias event selection I restricted the data to a shortened run range from run12996-run13137 (January 19, 2025 - April 23, 2025). Out of 699,421 BNB Minimum Bias events, I select 4034 Minimum Bias events to be within $\pm$ 3 ns of a bunch center. This is found using 90% of the processed Run-4 BNB Minimum Bias data.

A neutrino candidate selected with the beam bunch timing is shown in Figure 6.33. This event (run 13055 event 1767) was identified with an interaction time 0.33 ns from a beam bunch peak and located in the East T-300 cryostat in TITUS. This event is a potential neutral current neutrino candidate identified from the short proton tracks with a short muon or pion track. Another candidate neutrino event is shown in Figure 6.35 (run 13055 event 5153), where we see a long muon track connected to a short proton track at the vertex. The flash was again in the East cryostat with an interaction time 0.3 ns from a beam bunch peak. This was identified as a clear neutrino candidate event due to the clean interaction signature, with the vertex pointing back towards the beam direction (BNB points left to right in the TITUS event display).

Figure 6.35 displays another neutrino candidate event identified with the beam bunch timing, located in the West cryostat with a interaction time 0.74 ns from a beam bunch peak. This is a very interesting event where we see a potential neutral current interaction, with a short proton track, corresponding to just a few cm, at the interaction vertex. There appears to be a neutron traveling upwards that scatters an makes a proton, identified by the small track with a gap separating it from the other tracks. Neutrons are neutral particles and do not leave a track in LArTPCs. We only see the particles that the neutron scatters against. The final segment appears to be a minimum ionizing particle as the track stops, potentially with a charged pion on the left-hand side of the interaction.

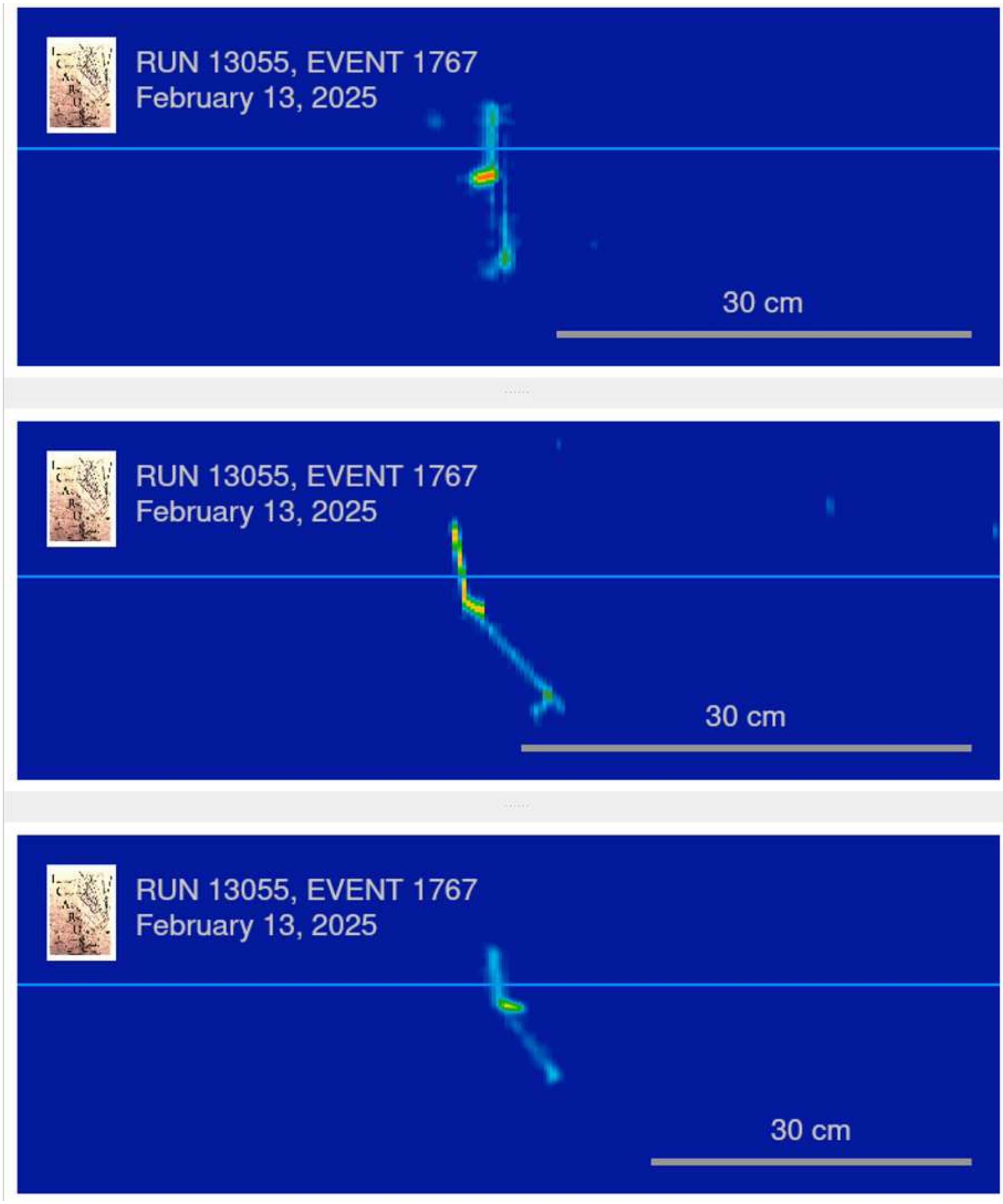

Figure 6.33: Run-4 BNB Minimum Bias run 13055 event 1767 in the TITUS event display.

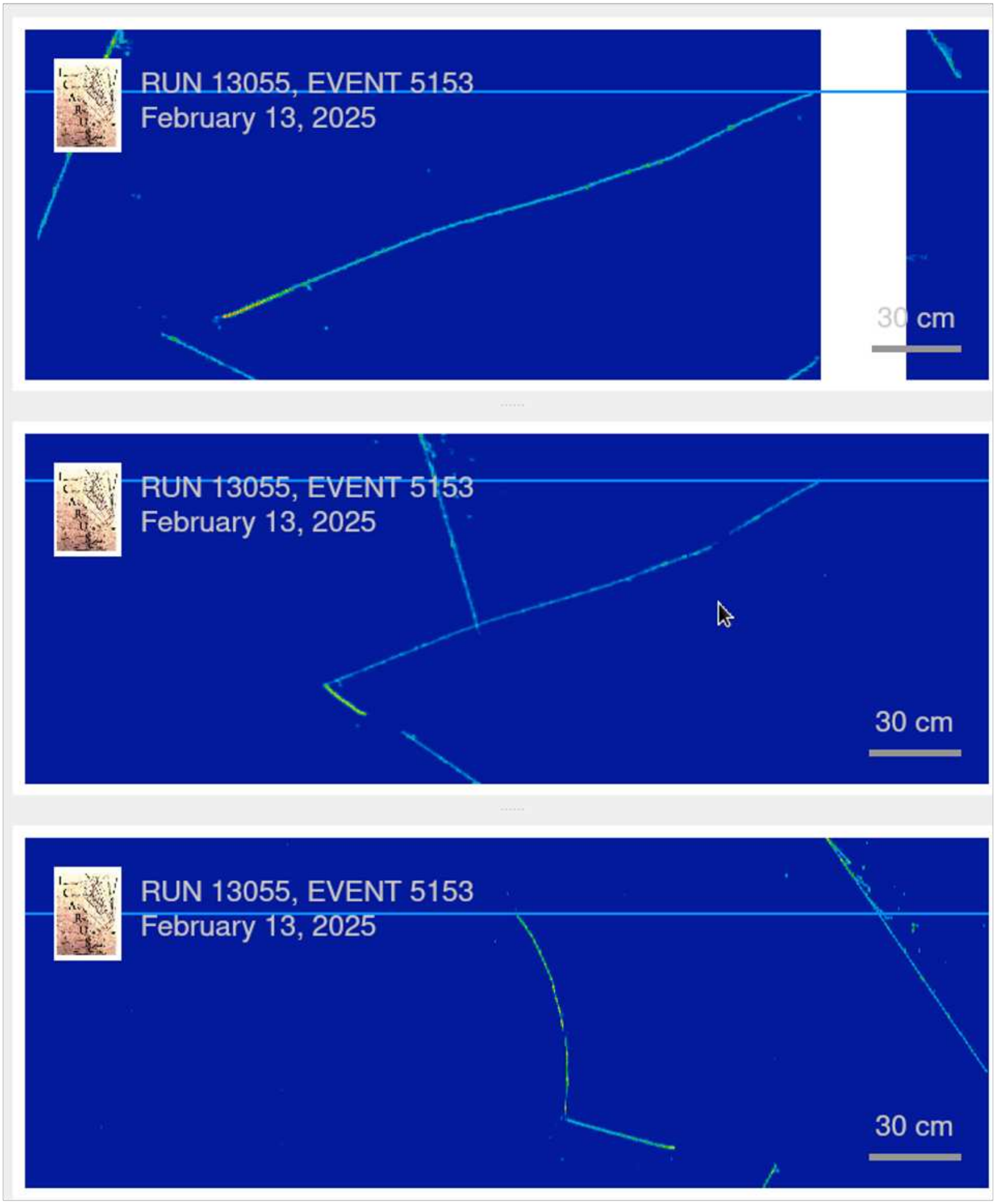

Figure 6.34: Run-4 BNB Minimum Bias run 13055 event 5153 in the TITUS event display.

Figure 6.35: Run-4 BNB Minimum Bias run 13055 event 5153 in the TITUS event display.

6.5.4 Trigger efficiency using Minimum Bias Data

The Minimum Bias data stream can be exploited to get an unbiased measurement of trigger efficiency. In this work, I apply a cut at ± 3 ns around the beam bunch peak to select BNB Minimum Bias events. Work was done within the trigger group including R. Triozzi, M. Rossella, D. Torretta, G. Petrillo and T. Krishnan to save the hardware trigger response for Minimum Bias events even though this information was not used to trigger the readout. The Minimum Bias data is recorded in both the on-beam and off-beam data streams, but there is no trigger requirement on the amount of scintillation light seen. The only requirement for Minimum Bias data is if the respective beam gate is present. This additional trigger hardware information records whether the Majority or Adder trigger requirements would have been met for that event based on the amount of PE light and the light pattern. The response from these additional trigger diagnostics were recently made available in the CAFs by Triozzi. For each event, the trigger logic (adder-only, Majority-only, or both), trigger time and which cryostat had the first trigger within the gate is saved. This information became available starting from Run-3.

Events selected to be within ± 3 ns of a beam bunch center can be identified to have passed the trigger requirements by leveraging the additional trigger information. Out of the 4,034 Run-4 Minimum Bias events selected with a timing cut, 3,972 Run-4 Minimum Bias events passed trigger requirements giving a trigger efficiency of $\sim$98.5%. 62 events selected with timing cut were found to not pass the hardware trigger requirements (adder or Majority). In Figure 6.36, I show the total flash photoelectrons (PE) for all of the selected events and those that pass the trigger requirements. A proxy for the trigger efficiency as a function of the flash PE can be extracted by taking the binned ratio of the events that pass the trigger requirements over all of the selected events, shown in Figure 6.37. These distributions inform us that the events that did not pass the trigger requirements are those with a low amount of detected scintillation light (low PE), where we see the ratio start to drop off for events with a total flash PE below 2000. The bins less than 700 PE have much lower statistics, resulting in larger error bars in Figure 6.37.

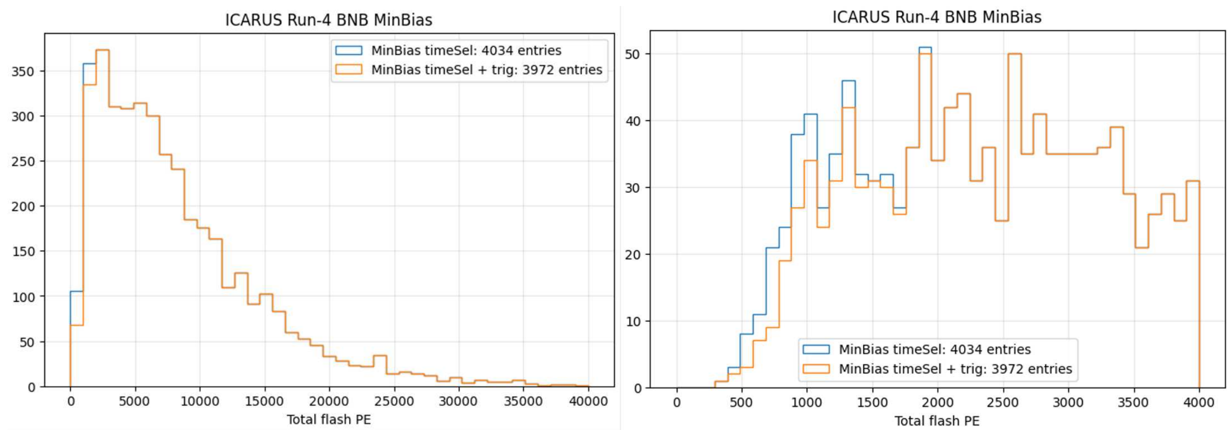

(a) Flash PE distribution. **(b)** Total Flash PE zoomed in on lower PE values

Figure 6.36: Total flash photoelectrons (PE) for events selected with bunch timing (blue) and out of those, events that pass the hardware trigger requirements (orange).

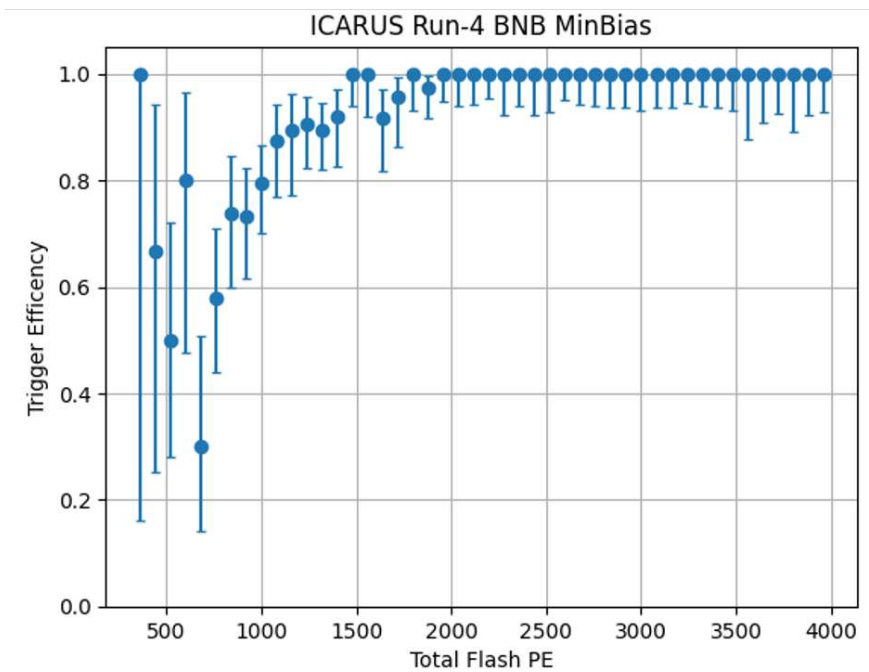

Figure 6.37: Binned ratio of selected events that pass the trigger requirements over all selected events as a function of binned total flash PEs.

6.5.5 Energy of Minimum Bias Selected Events

With the capability to select neutrino candidates from the Minimum Bias data stream, this enables the opportunity to investigate the reconstructed energy range from this unbiased dataset. In collaboration with INFN-Padova postdoctoral researcher Maria Artero, the Run-4 BNB Minimum Bias sample was passed through the Pandora event selection and reconstruction she developed for ICARUS' 1μNp disappearance used in [59]. The neutrino energy is reconstructed for the 1μNp events based on range, which is used to reconstructed the energy of particles in LArTPCs based on the distance traveled. Events selected with the beam bunch timing were matched to those selected in the 1μNp selection.

The effect of the timing cut centered on the beam bunch peak is studied by gradually enlarging the timing window and evaluating the corresponding selection efficiency, quantified as the fraction of 1μNp events that remain. This dependence is illustrated in Figure 6.38. Of the 521 1μNp candidates, 396 lay within 2σ (5.86 ns) of a beam bunch peak, corresponding to an efficiency of 76% for this timing cut and is illustrated by the blue horizontal line at 2σ in Figure 6.38. The fraction of 1μNp Minimum Bias events that are selected is compared to the neutrino selection efficiency predicted by an Error Function with a sigma of 2.93 ns, corresponding to the bunch width I obtain from the BNB Majority bunch fit. The fraction of selected Minimum Bias events is lower than what is predicted by the Error Function with σ = 2.93 ns (54% observed versus the expected 68% at 1σ). This discrepancy may arise from using the Minimum Bias data stream, which has a less clean structure and significantly lower statistics than the BNB Majority stream, potentially leading to a somewhat larger effective bunch width.

The distribution plateaus to a fraction of 86.9% around 9.45 ns. The observation that the fraction of 1μNp events reaches a plateau at this point is consistent with expectations, as this value corresponds approximately to half of the bunch spacing. When the cut value exceeds half of the bunch spacing, the selection would only select more events originating from the neighboring bunch. Applying a timing cut of 9.45 ns selects 452 out of the 521 1μNp candidates. The 69 events that aren't selected with the 9.45 ns timing cut will be further studied in detail by looking at the

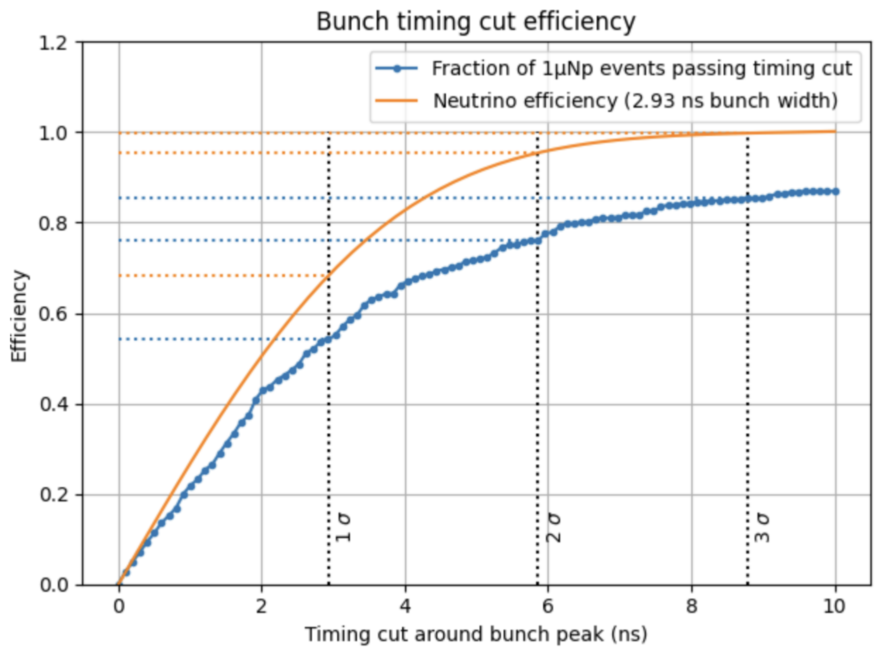

Figure 6.38: Fraction of 1μNp events selected (blue) compared with the neutrino efficiency (orange) as a function of a timing cut around the beam bunch peak. The neutrino efficiency is estimated using an Error Function with a bunch spacing of σ = 2.93 ns, which was extrapolated from Run-4 BNB Majority data used to overlay and select events from the BNB Minimum Bias stream.

spatial and temporal distributions, along with looking at these events in the TITUS Event Display. Figure 6.39 shows the reconstructed neutrino energy of the total number of Run-4 BNB Minimum Bias 1μNp selected events compared with the subset of events found to be within and not within two example timing cuts of 2σ (5.86 ns) and half bunch spacing (9.45 ns). Compared with the efficiency of 48% reported in [59] for the 1μNp selection using the same Pandora event selection, this beam bunch timing selection with the unbiased data provides an additional handle to identify neutrino events and can supplement existing ICARUS event selections.

6.5.6 Beyond Standard Model Searches

Precise timing has powerful applications for model independent Beyond the Standard Model (BSM) searches. Heavy dark matter particles produced in the BNB or NuMI beams would arrive at the detector delayed with respect to the beam neutrinos. With a heavier mass, a dark matter (DM) candidate will travel slower and show up later, in between bunches. Since ICARUS is further away from the beam targets compared to SBND and MicroBooNE, this effect is expected to be larger

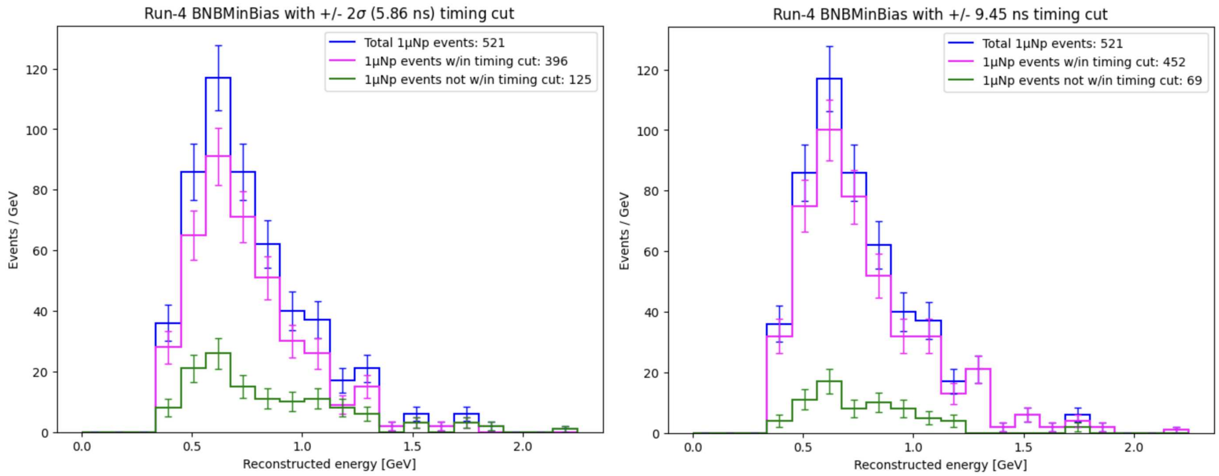

(a) 2σ (5.86 ns) timing cut. **(b)** Half bunch spacing (9.45 ns) timing cut.

Figure 6.39: Reconstructed neutrino energy for all Run-4 BNB Minimum Bias 1µNp selected events and the subset of those 1µNp events found to be within and not within two example timing cuts.

at ICARUS. Precise timing can enhance DM searches by looking for event candidates arriving delayed but correlated with the neutrino beam. This has the potential to improve the sensitivity range of studies currently underway by CSU graduate student Jamie Dyer, CSU physics professor Joshua Berger and others in the ICARUS BSM group.

Chapter 7

Conclusions

The work of this thesis was dedicated to leveraging precise timing information for background rejection in the ICARUS LarTPC. We are able to resolve the beam bunch structure within the ICARUS detector to sub-nanosecond timing precision with PMT light only, which enables its use for additional background rejection by leveraging the periodic structure of the neutrino beam.

This analysis resolved the bunch structure observed in various ICARUS runs collected from 2022 to 2026. Using light information only, I reconstruct an average bunch width of 3.07 ± 0.06 ns and 2.78 ± 0.02 ns in Run-2 and the end of Run-4 respectively. I show data collected with a special narrow beam configuration from the Fermilab Accelerator Division, where they established a narrow bunch beam with an intrinsic width of $\sim$0.9 ns compared to the nominal BNB bunch width of $\sim$1.3 ns. ICARUS was able to detect this difference in bunch width, where we observe a reconstructed bunch width of 2.51 ± 0.05 ns by collecting 51 hours of data with this narrow beam bunch configuration. This provided an additional data point to extract a measurement for the upper bound of the intrinsic ICARUS PMT timing resolution of 2.44 ns.

I presented a novel approach for selecting neutrino events in our Minimum Bias data stream using the beam bunch structure. This work is the first demonstration of using the beam bunch timing to select events from an unbiased data stream in a LArTPC.

Bibliography

[1] Wikipedia. Elementary particles of the standard model, 2019. https://en.wikipedia.org/wiki/Standard_Model.

[2] P. B. Denton, M. Friend, M. D. Messier, et al. Snowmass neutrino frontier: Nf01 topical group report on three-flavor neutrino oscillations, 2022.

[3] A. Aguilar, L. B. Auerbach, R. L. Burman, et al. Evidence for neutrino oscillations from the observation of $\overline{\nu}_e$ appearance in a $\overline{\nu}_\mu$ beam. *Phys. Rev. D*, 64:112007, Nov 2001.

[4] A. A. Aguilar-Arevalo, B. C. Brown, J. M. Conrad, et al. Updated MiniBooNE neutrino oscillation results with increased data and new background studies. *Physical Review D*, 103(5), March 2021.

[5] R. Acciarri, C. Adams, R. An, et al. A proposal for a three detector short-baseline neutrino oscillation program in the fermilab booster neutrino beam, 2015.

[6] B. Abi, R. Acciarri, Mario A. Acero, et al. Deep underground neutrino experiment (DUNE), far detector technical design report, volume ii: DUNE physics. *arXiv preprint arXiv:2002.03005*, 2020.

[7] Fermilab Visual Media Services. Fermilab's accelerator complex. https://www.fnal.gov/pub/science/particle-accelerators/accelerator-complex.html.

[8] R. Acciarri, C. Adams, R. An, et al. Design and construction of the MicroBooNE detector. *Journal of Instrumentation*, 12(02):P02017–P02017, February 2017.

[9] C. Adams, M. Alrashed, R. An, et al. Design and construction of the MicroBooNE cosmic ray tagger system. *Journal of Instrumentation*, 14(04):P04004–P04004, April 2019.

[10] B. Behera and the ICARUS collaboration. Cosmogenic background suppression at the ICARUS using a concrete overburden. *Journal of Physics: Conference Series*, 2156(1):012181, Dec 2021.

[11] P. Abratenko, A. Aduszkiewicz, F. Akbar, et al. ICARUS at the fermilab short-baseline neutrino program: initial operation. *The European Physical Journal C*, 83(6):467, 2023.

[12] A. Aduszkiewicz, L. Bagby, B. Behera, et al. Design and implementation of the cosmic ray tagger system for the ICARUS detector at FNAL. *Journal of Instrumentation*, 20(04):T04002, apr 2025.

[13] V Boccone and (on behalf ofthe ArDM collaboration). The ArDM project: A liquid argon TPC for dark matter detection. *Journal of Physics: Conference Series*, 160(1):012032, apr 2009.

[14] M. Vicenzi and on behalf of the ICARUS collaboration. Calibration and timing performance of the light detection system in the ICARUS detector. *Journal of Instrumentation*, 20(03):C03049, mar 2025.

[15] F. Abd Alrahman, P. Abratenko, N. Abrego-Martinez, et al. Operation of the trigger system for the ICARUS detector at fermilab. *Journal of Instrumentation*, 20(10):P10044, oct 2025.

[16] C. Hilgenberg. *Cosmogenic Background Rejection for the Sterile Neutrino Search with the Short-Baseline Neutrino Program Far Detector*. PhD thesis, Colorado State University, Fort Collins, CO, 2020.

[17] CAEN. *A1702 / DT5702 32-channel SiPM Readout Board for Cosmic Rays Veto - User manual*, 2023. https://www.caen.it/download/?filter=A1702.

[18] P. Abratenko, N. Abrego-Martinez, A. Aduszkiewicz, et al. Calibration and simulation of ionization signal and electronics noise in the ICARUS liquid argon time projection chamber. *Journal of Instrumentation*, 20(01):P01032, jan 2025.

[19] IARC at Fermilab. RF power source. https://iarc.fnal.gov/rf-power-source/.

[20] K. Yonehara. Accelerator concepts for BNB narrow bunch beam. *FNAL Beams-doc-10972*, 2026. https://beamdocs.fnal.gov/cgi-bin/sso/ShowDocument?docid=10972.

[21] Brian Fellenz and Jim Crisp. An improved resistive wall monitor. *AIP Conference Proceedings*, 451(1), 12 1998.

[22] Z. Pavlovic and M. Stancari. Documentation of the RWM setup in MI-12. *SBN Document 46546*, 2026. https://sbn-docdb.fnal.gov/cgi-bin/sso/RetrieveFile?docid=46546&filename=MI-12%20RWM%20setup.pdf&version=1.

[23] M. Backfish. MiniBooNE resistive wall current monitor. *FERMILAB-TM-2556-AD*, 2013. https://lss.fnal.gov/archive/test-tm/2000/fermilab-tm-2556-ad.pdf.

[24] American Physical Society. This month in physics history. https://www.aps.org/archives/publications/apsnews/201107/physicshistory.cfm, July 2011.

[25] F. Reines and C. L. Cowan. Detection of the free neutrino. *Phys. Rev.*, 92:830–831, Nov 1953.

[26] CERN. Neutrinos detected at last! https://timeline.web.cern.ch/neutrinos-detected-last, June 1956. Accessed: 2026-05-26.

[27] C. L. Cowan, F. Reines, F. B. Harrison, H. W. Kruse, and A. D. McGuire. Detection of the free neutrino: a confirmation. *Science*, 124(3212):103–104, 1956.

[28] Nobel Prize Outreach. The nobel prize in physics 1995. https://www.nobelprize.org/prizes/physics/1995/summary/, 1995. Accessed: 2026-05-26.

[29] Brookhaven National Laboratory. 1988 nobel prize in physics. https://www.bnl.gov/bnlweb/history/nobel/1988.php. Accessed: 2026-05-26.

[30] John N. Bahcall and Raymond Davis. Solar neutrinos: A scientific puzzle. *Science*, 191(4224):264–267, 1976.

[31] B. Pontecorvo. Mesonium and antimesonium. *Zh. Eksp. Teor. Fiz.*, 33:549, 1957.

[32] B. Pontecorvo. Neutrino experiments and the problem of conservation of leptonic charge. *Sov. Phys. JETP*, 26(5):984–988, 1968.

[33] S. Fukuda, Y. Fukuda, T. Hayakawa, et al. The super-kamiokande detector. *Nuclear Instruments and Methods in Physics Research Section A: Accelerators, Spectrometers, Detectors and Associated Equipment*, 501(2):418–462, 2003.

[34] Nick Jelley, Arthur B. McDonald, and R.G. Hamish Robertson. The Sudbury Neutrino Observatory. *Annual Review of Nuclear and Particle Science*, 59(Volume 59, 2009):431–465, 2009.

[35] C Athanassopoulos, L.B Auerbach, D Bauer, et al. The liquid scintillator neutrino detector and LAMPF neutrino source. *Nuclear Instruments and Methods in Physics Research Section A: Accelerators, Spectrometers, Detectors and Associated Equipment*, 388(1):149–172, 1997.

[36] Alexis A. Aguilar-Arevalo. The MiniBooNE Experiment. *eConf*, C0406271:MONP01, 2004.

[37] A. A. Aguilar-Arevalo, B.C. Brown, L. Bugel, et al. Significant excess of electronlike events in the MiniBooNE short-baseline neutrino experiment. *Physical Review Letters*, 121(22), November 2018.

[38] S. Ritz, H. Aihara, M. Breidenbach, et al. Building for discovery: Strategic plan for U.S. particle physics in the global context. May 2014.

[39] C. Rubbia. The liquid-argon time projection chamber: A new concept for neutrino detectors. *CERN-EP 77-08*, 1977.

[40] S. Amerio, S. Amoruso, M. Antonello, et al. Design, construction and tests of the ICARUS T600 detector. *Nuclear Instruments and Methods in Physics Research Section A: Accelerators, Spectrometers, Detectors and Associated Equipment*, 527(3):329–410, 2004.

[41] A. R. Miller. BNB accelerator timing signals. *FNAL Beams-doc-6771v10*, 2019. https://beamdocs.fnal.gov/AD/DocDB/0067/006771/009/BNB%20Accelerator%20Timing%20Signals.pdf.

[42] P. Adamson, K. Anderson, M. Andrews, et al. The NuMI neutrino beam. *Nuclear Instruments and Methods in Physics Research Section A: Accelerators, Spectrometers, Detectors and Associated Equipment*, 806:279–306, 2016.

[43] P. Abratenko, R. An, J. Anthony, et al. Novel approach for evaluating detector-related uncertainties in a LArTPC using MicroBooNE data. *The European Physical Journal C*, 82(5), May 2022.

[44] P. Abratenko, O. Alterkait, D. Andrade Aldana, et al. First demonstration of $\mathcal{O}(1\ \mathrm{ns})$ timing resolution in the MicroBooNE liquid argon time projection chamber. *Phys. Rev. D*, 108:052010, Sep 2023.

[45] MicroBooNE Collaboration, P. Abratenko, M. Alrashed, R. An, et al. Measurement of the atmospheric muon rate with the MicroBooNE liquid argon TPC. *Journal of Instrumentation*, 16(04):P04004, apr 2021.

[46] MicroBooNE collaboration, P. Abratenko, R. An, J. Anthony, et al. Measurement of the longitudinal diffusion of ionization electrons in the MicroBooNE detector. *Journal of Instrumentation*, 16(09):P09025, sep 2021.

[47] P. Abratenko, R. An, J. Anthony, et al. Calorimetric classification of track-like signatures in liquid argon TPCs using MicroBooNE data. *Journal of High Energy Physics*, 2021(12), December 2021.

[48] P. Abratenko, O. Alterkait, D. Andrade Aldana, et al. Measurement of ambient radon progeny decay rates and energy spectra in liquid argon using the MicroBooNE detector. *Physical Review D*, 109(5), March 2024.

[49] R. Acciarri, C. Adams, R. An, et al. Michel electron reconstruction using cosmic-ray data from the MicroBooNE LArTPC. *Journal of Instrumentation*, 12(09):P09014–P09014, September 2017.

[50] MicroBooNE collaboration, P. Abratenko, D. Andrade Aldana, et al. Search for the production of higgs-portal scalar bosons in the NuMI beam using the MicroBooNE detector, 2025.

[51] P. Abratenko, D. Andrade Aldana, J. Anthony, et al. First constraints on light sterile neutrino oscillations from combined appearance and disappearance searches with the MicroBooNE detector. *Physical Review Letters*, 130(1), January 2023.

[52] MicroBooNE Collaboration, A. M. Abdullahi, P. Abratenko, et al. First search for dark sector e^+e^- explanations of the MiniBooNE anomaly at MicroBooNE, 2025.

[53] P. Benetti, A. Bettini, E. Calligarich, et al. A three-ton liquid argon time projection chamber. *Nucl. Instrum. Methods Phys. Res., A*, vol. 332, no. DFPD-93-EP-05:395–412, 1993.

[54] M. Antonello, B. Baibussinov, P. Benetti, et al. Search for anomalies in the ν_e appearance from a ν_μ beam. *Eur. Phys. J. C*, 73:2599, 2013.

[55] M. Antonello, B. Baibussinov, P. Benetti, et al. Measurement of the neutrino velocity with the ICARUS detector at the CNGS beam. *Physics Letters B*, 713:17–22, 2012.

[56] L. Bagby, B. Baibussinov, B. Behera, et al. Overhaul and installation of the ICARUS-T600 liquid argon TPC electronics for the fnal short baseline neutrino program. *Journal of Instrumentation*, 16(01):P01037, Jan 2021.

[57] P. Abratenko, N. Abrego-Martinez, A. Aduszkiewicz, et al. Angular dependent measurement of electron-ion recombination in liquid argon for ionization calorimetry in the ICARUS liquid argon time projection chamber. *Journal of Instrumentation*, 20(01):P01033, jan 2025.

[58] F. Abd Alrahman, P. Abratenko, N. Abrego-Martinez, et al. Search for a hidden sector scalar from kaon decay in the dimuon final state at ICARUS. *Phys. Rev. Lett.*, 134:151801, Apr 2025.

[59] ICARUS Collaboration. First search for sterile neutrino oscillation leading to ν_μ disappearance in the booster neutrino beam at ICARUS, 2026.

[60] T. Kobilarcik. Bunch rotation in the booster neutrino beamline. *FNAL Beams-doc-6904*, 2018. https://beamdocs.fnal.gov/cgi-bin/sso/ShowDocument?docid=6904.

[61] M. Bonesini, R. Benocci, R. Bertoni, et al. The upgraded laser calibration system of the ICARUS experiment at FNAL. *Nuclear Instruments and Methods in Physics Research Section A: Accelerators, Spectrometers, Detectors and Associated Equipment*, 1067:169670, 2024.

[62] T. Boone. *ICARUS Cosmic Ray Tagger Efficiency*. PhD thesis, Colorado State University, Fort Collins, CO, 2024.

[63] H. de Kerret, Y. Abe, C. Aberle, et al. The double chooz antineutrino detectors. *Eur.Phys. J. C*, 82, 804, 2022.

[64] D.G. Michael, P. Adamson, T. Alexopoulos, et al. The magnetized steel and scintillator calorimeters of the MINOS experiment. *Nuclear Instruments and Methods in Physics Research Section A: Accelerators, Spectrometers, Detectors and Associated Equipment*, 596(2):190–228, November 2008.

[65] M. Auger, A. Ereditato, D. Goeldi, et al. Multi-channel front-end board for sipm readout. *Journal of Instrumentation*, 11(10):P10005, oct 2016.

[66] K. Biery, C. Green, J. Kowalkowski, M. Paterno, and R. Rechenmacher. artdaq: An event-building, filtering, and processing framework. *IEEE Transactions on Nuclear Science*, 60(5):3764–3771, 2013.

[67] Fermilab. The art event processing framework. https://art.fnal.gov/.

[68] P. Abratenko, R. An, J. Anthony, et al. Novel approach for evaluating detector-related uncertainties in a LArTPC using MicroBooNE data. *The European Physical Journal C*, 82(5), May 2022.

[69] A Aurisano, C Backhouse, R Hatcher, N Mayer, J Musser, R Patterson, R Schroeter, and A Sousa. The NOvA simulation chain. *Journal of Physics: Conference Series*, 664(7):072002, dec 2015.

[70] C. Andreopoulos, A. Bell, D. Bhattacharya, et al. The GENIE neutrino monte carlo generator. *Nuclear Instruments and Methods in Physics Research Section A: Accelerators, Spectrometers, Detectors and Associated Equipment*, 614(1):87–104, February 2010.

[71] S. Agostinelli, J. Allison, K. Amako, et al. Geant4—a simulation toolkit. *Nuclear Instruments and Methods in Physics Research Section A: Accelerators, Spectrometers, Detectors and Associated Equipment*, 506(3):250–303, 2003.

[72] D. Heck, J. Knapp, J. N. Capdevielle, G. Schatz, and T. Thouw. CORSIKA: A Monte Carlo code to simulate extensive air showers. 2 1998.

[73] E.L. Snider and G. Petrillo. LArSoft: toolkit for simulation, reconstruction and analysis of liquid argon TPC neutrino detectors. *Journal of Physics: Conference Series*, 898(4):042057, oct 2017.

[74] P. Abratenko, M. Alrashed, R. An, et al. Measurement of the atmospheric muon rate with the MicroBooNE liquid argon TPC. *Journal of Instrumentation*, 16(04):P04004, April 2021.

[75] P. S. Martin and D. W. Wildman. Bunch coalescing and bunch rotation in the Fermilab main ring: Operational experience and comparison with simulations. *European Particle Accelerator Conference Proceedings*, 1988.